The Pennsylvania State University

The Graduate School

NOVEL META-SURFACE DESIGN SYNTHESIS VIA NATURE-INSPIRED OPTIMIZATION ALGORITHMS

A Dissertation in

Electrical Engineering

by

Zikri Bayraktar

Submitted in Partial Fulfillment
of the Requirements
for the Degree of

Doctor of Philosophy

May 2011

The dissertation of Zikri Bayraktar was reviewed and approved* by the following:

Douglas H. Werner
Professor of Electrical Engineering
Dissertation Advisor
Chair of Committee

Pingjuan L. Werner
Professor of Electrical Engineering

Victor Pasko
Professor of Electrical Engineering

Brian L. Weiner
Professor of Physics

Lyle N. Long
Distinguished Professor of Aerospace Engineering

W. Kenneth Jenkins
Professor of Electrical Engineering
Head of the Department of Electrical Engineering

*Signatures are on file in the Graduate School

ABSTRACT

Heuristic numerical optimization algorithms have been gaining interest over the years as the computational power of the digital computers increases at an unprecedented level every year. While mature techniques such as the Genetic Algorithm increase their application areas, researchers also try to come up with new algorithms by simply observing the highly tuned processes provided by the nature. In this dissertation, the well-known Genetic Algorithm (GA) will be utilized to tackle various novel electromagnetic optimization problems, along with parallel implementation of the Clonal Selection Algorithm (CLONALG) and newly introduced the Wind Driven Optimization (WDO) technique. The utility of the CLONALG parallelization and the efficiency of the WDO will be illustrated by applying them to multi-dimensional and multi-modal electromagnetics problems such as antenna design and metamaterial surface synthesis.

One of the metamaterial application areas is the design synthesis of 90 degrees rotationally symmetric ultra-small unit cell artificial magnetic conducting (AMC) surfaces. AMCs are composite metallo-dielectric structures designed to behave as perfect magnetic conductors (PMC) over a certain frequency range, those exhibit a reflection coefficient magnitude of unity with an phase angle of zero degrees at the center of the band. The proposed designs consist of ultra small sized frequency selective surface (FSS) unit cells that are tightly packed and highly intertwined, yet achieve remarkable AMC band performance and field of view when compared to current state-of-the-art AMCs. In addition, planar double-sided AMC (DSAMC) structures are introduced and optimized as AMC ground planes for low profile antennas in composite platforms and separator slabs for vertical antenna applications. The proposed designs do not possess complete metallic ground planes, which makes them ideal for composite and multi-antenna systems. The versatility of the DSAMC slabs is also illustrated where designs with

lossy impedance patches on one face of the slab can be optimized for absorber applications while the other face of the slab still exhibits properties of an AMC.

Another metamaterial design synthesis targets optimization of metallo-dielectric slabs to act as low-loss matched impedance magneto-dielectric metamaterials (MIMDM). Such designs provide magneto-dielectric material properties over a certain frequency range, allowing miniaturization of planar antennas when used as substrates. Similarly, MIMDM slabs can be designed for the absorber applications, where design equations for synthesizing such absorber materials from MIMDM are established.

Finally, small sized rotationally symmetric unit cells are designed and employed as planar electromagnetic bandgap structures for microstrip patch antenna mutual coupling reduction.

TABLE OF CONTENTS

LIST OF FIGURES

LIST OF TABLES

ACKNOWLEDGEMENTS

I would like to thank my dissertation advisor, Professor Douglas H. Werner, for his guidance, patience and providing me with challenging projects and financial support throughout my undergraduate and graduate careers. I would also like to thank my co-advisor, Professor Pingjuan L. Werner, for her never-ending support over the years that I have been a member of the Computational Electromagnetic and Antennas Research Lab (CEARL). I also would like to thank Professor Victor P. Pasko, Professor Brian L. Weiner and Professor Lyle N. Long for serving on my doctoral committee and providing helpful criticism for this dissertation.

I would like to acknowledge Dr. Jeremy A. Bossard, Micah D. Gregory, Dr. Joshua S. Petko, Dr. Matthey G. Bray, Donovan Brocker, Clinton Scarborough, Dr. Do-Hoon Kwon, Dr. Douglas Kern and all other past and current members of the CEARL for providing me with valuable moral support, technical advice, fruitful discussions and unmatched friendship throughout the years. Their collaborations and support have been a key in achieving the novel work presented in this dissertation and in other technical publications.

I would also like to thank my family, especially my parents, Sacide Bayraktar and Alaaddin Bayraktar, for sending me abroad and opening up a whole new world for me. With your support, I have accomplished and with your encouragements, I will top it in the future.

At last but not the least, I would like to thank my wife, Muge Komurcu Bayraktar for dating me many years during difficult times of the graduate life, for marrying me and for baring with me during the compilation of this dissertation. Our wonderful journey just started!

Chapter 1

Introduction

This chapter introduces the topics of this dissertation, which can be categorized into two major research trusts, where the first trust is the study, development and implementation of diverse nature-inspired numerical optimization algorithms and the second trust is the automated design synthesis of novel meta-material surfaces through utilization of the numerical optimization algorithms linked with fast numerical electromagnetic solvers. The technical approach and the current state of the art are discussed as well as the original contributions to the field of study are outlined.

1.1. Statement of Problem

Increasing consumer demand for more capable wireless and high-speed data services has led to new wideband and multi-band wireless communication devices, which are physically small and aesthetically pleasing. The technology behind the new generation devices employ either conformal antennas in composite antenna systems or multi-antenna systems in physically small devices. Such systems can increase data rates, provide robustness and reduce interference with other electronic equipment [1] while requiring smaller footprint and reduced weight. However, mutual coupling issues can arise from having multiple antennas in tightly packed compact systems. To this end, research presented here can be used to develop and optimize thin meta-material surfaces for antenna applications that can reduce the coupling between closely spaced vertical antennas or can be synthesized for miniaturization of the conformal antennas with negligible performance degradation in VSWR or in radiation pattern.

With the increasing use of composite materials in aircrafts and in other large platforms, the need for composite antenna/ground plane systems is ubiquitous. Low profile antennas in aircrafts would require deployment of artificial magnetic conducting (AMC) ground planes to operate efficiently, yet, composite system requirements would demand elimination of the complete metallic ground planes, which could actually interfere with the efficient operation of multiple antennas deployed on aircrafts. An AMC ground plane that does not require complete metallic back plane have been introduced in [2], where sub-wavelength capacitively loaded loop (CLL) elements are embedded in a thick dielectric slab in a periodic fashion. However, this realization comes with the fabrication challenges and increased overall thickness which makes it not viable for practical purposes. To this end, research presented here can be used to develop and optimize thin planar easily fabricated double-sided AMC ground planes that could provide AMC ground plane behavior on either side, or could be tailored to allow transmission at one or multiple frequencies while eliminating the need for a complete metallic ground plane.

Electromagnetic absorbers represent another equally important area that can benefit from optimized thin meta-material designs. Absorbers can be used in variety of applications ranging from reducing the radar cross section of large objects [3] to reducing the reflected energy inside of an anechoic chamber [4]. In many practical applications, electromagnetic absorbers are required to cover curved surfaces of large objects, where the thickness of the absorber is a limiting design factor. Thus, engineered surfaces with thin profile and good performance are desired. In addition, there are desired traits that should be considered in the design of meta-material absorbers. The electrically small feature size of the meta-material structure becomes a very important design consideration, which can have significant effect on the field of view (FOV) of the absorber. To this end, utilizing interdigitated unit cell designs that are presented in this research can provide ultra small sized unit cells with excellent FOV even for very thin absorber designs.

The novel meta-surface designs with exotic properties targeting various applications can be synthesized and analyzed utilizing fast numerical electromagnetic solvers. Unfortunately, the structures are very complicated than any conventionally known materials and there are no analytical methods to tackle the design of such exotic meta-material surfaces, hence utilization of numerical optimization algorithms are inevitable. To this end, research presented here studies and utilizes some of the well known nature-inspired optimization algorithms such as Genetic Algorithms [5] and Particle Swarm Optimization [6], and explores some of the less known algorithms in parallel computing schema such as the Clonal Selection Algorithm. In addition, a novel nature-inspired algorithm is developed and introduced to the Computational Electromagnetics society, which is called the Wind Driven Optimization [7]. This is a simple and easy to implement algorithm, and efficient in solving multi-dimensional optimization problems.

1.2. Technical Approach and Current State of the Art

The research presented within this dissertation integrates efficient nature-inspired numerical optimization algorithms with fast numerical electromagnetics solvers for feed-forward design optimization of various thin composite meta-surfaces targeting a variety of applications.

A Perfect Magnetic Conducting (PMC) ground plane reflects an incident electromagnetic wave with no phase shift with respect to the incident wave, which is different than the conventional Perfect Electric Conducting (PEC) ground planes. This unique property makes the PMCs ideal for low-profile antenna applications, where the image of the antenna does not degrade its performance. However, PMCs do not occur naturally, hence Artificial Magnetic Conductor (AMC) ground planes are engineered instead. The first AMC ground plane, introduced by Sievenpiper *et al.*, consisted of a periodic array of mushroom-like structures with square, rectangular or hexagonally shaped patches connected to a PEC ground plane with vertical metallic vias [8] as shown in Figure 1-1 (a). Such structure behaves as a resonant high-impedance surface, where the propagation of surface waves at certain frequency bands was prohibited, hence the name electromagnetic bandgap (EBG) material. Another simpler metamaterial approach introduced by Ma *et al.* replaced the mushroom structures with a complex shaped metallic frequency selective surface (FSS) backed by a dielectric substrate and a PEC backplane [9] as shown in Figure 1-1 (b). Similar to the mushroom realization, this FSS-based metamaterial surface behaves as a high-impedance surface and has an AMC condition at resonance. The FSS-based AMC structures come with a complete metallic ground plane, which makes them ideal for low profile antenna applications when the antenna is mounted on a platform with a metallic skin, such as the fuselage or the wing of an aircraft or any other vehicle. However, with the increasing use of composites in aircrafts, metamaterials that do not require a complete metallic backplane are also of great interest for low-profile and embedded antenna systems. Recently, Erentok *et al.* introduced a volumetric AMC design with two stacked layers of vertically orientated capacitively loaded loops (CLL) [2] as seen in Figure 1-1 (c). This realization does not require a complete PEC ground plane backing, and is well-suited for antenna applications on composite platforms.

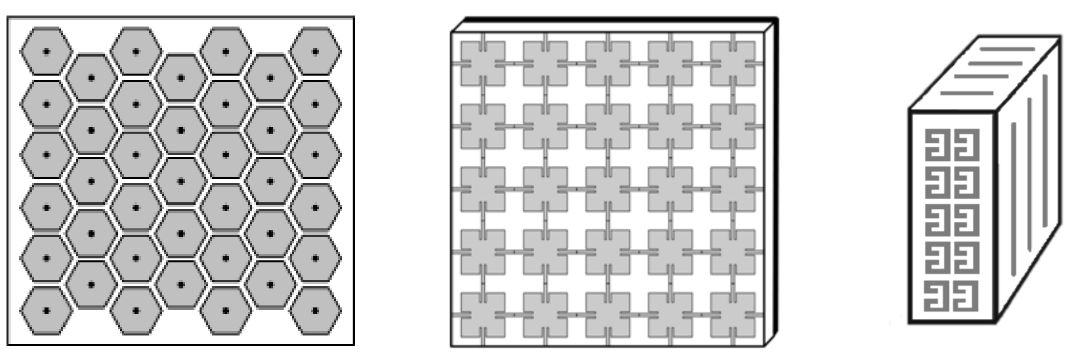

(a) (b) (c)

Figure 1-1: (a) Mushroom type high-impedance Frequency Selective Surface (FSS) designed as EBG structure consisting of hexagonal patches connected to the PEC ground plane with vertical metallic vias, (b) Periodic FSS metal pattern backed by dielectric substrate and a PEC ground plane designed as planar AMC ground plane, (c) Volumetric AMC design with stacked multi-layers of vertically oriented capacitively loaded loops printed on dielectric substrate blocks.

However, the primary drawback of the volumetric AMC design is the thickness of the structure, which is approximately $\lambda_r/3$ within the dielectric. For a practical application, it is desired to achieve an AMC ground plane thinner than the traditional quarter wavelength antenna standoff distance from a PEC ground. Also, another drawback is that the CLLs are oriented in a plane perpendicular to the metamaterial surface, which makes fabrication cumbersome. The proposed novel technique for synthesizing thin, planar, easily fabricated AMC ground surfaces are realized with two optimized, cascaded FSS screens [10] printed on either side of a dielectric slab. Bearing in mind that such a surface would be placed in close proximity of a horizontal antenna, a highly reflective composite structure with AMC phase response on the antenna side and PEC behavior on the opposite side would constitute the design goals for this structure.

The AMC structure proposed here consists of two cascaded PEC FSS screens separated by a dielectric layer as shown in Figure 1-2 (a). The FSS screens are doubly periodic and share the same unit cell dimensions but have independently pixilated geometries. The designs are limited to have a relative thickness less than $\lambda/10$ at the operating frequency. The square FSS unit cells are divided into 16 by 16 pixels, where top and bottom surfaces are independently optimized by a GA for desired responses off of the respective surfaces as seen below.

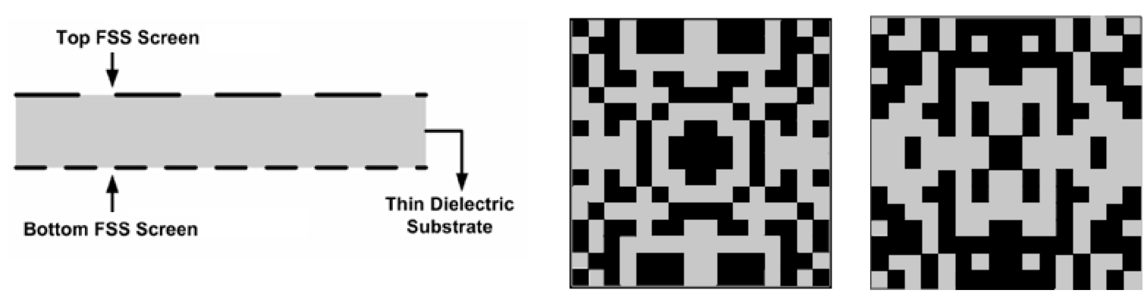

(a) (b) (c)

Figure 1-2: (a) Cross-sectional diagram of the AMC structure, showing a thin dielectric substrate sandwiched between two independently optimized FSS screens, (b) Top FSS unit cell geometry of an optimized design example, (c) Bottom FSS unit cell geometry of the same optimized design example, where black regions represent PEC pixels and gray regions represents dielectric pixels.

In addition to the ground planes for low profile antenna applications, these surfaces can be optimized for vertical monopole-type antenna systems as seen in Figure 1-3. The Double-Sided Artificial Magnetic Conductor (DSAMC) separator design technique requires both sides of the structure to be optimized for AMC characteristics at two different frequencies. In this method, two antennas of diverse operating frequencies (f_1 and f_2) can efficiently operate on opposite sides of the DSAMC structure while occupying a smaller footprint than normally would be required. For the optimization of DSAMC, a GA [5] is combined with Periodic Finite Element Boundary Integral (PFEBI) solver [11], which is a fast 3-D full-wave electromagnetic solver.

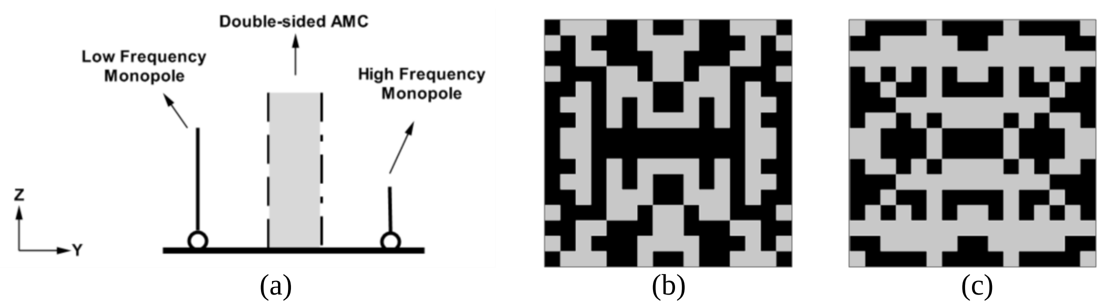

Figure 1-3: (a) The illustration of the DSAMC separator setup with two monopoles operating at different frequencies, (b) Top FSS unit cell geometry and (c) bottom FSS unit cell geometry, black regions represent the PEC pixels and gray regions represent the dielectric pixels. The bottom surface is designed for frequency f_1 and the top surface for frequency f_2.

The adaptability of the DSAMC slabs also allows for design synthesis of absorbers on one side and AMC or AEC response on the opposite. The metallic patches of the DSAMC slabs were assumed to be loss-less and for above applications only two-FSS-layered structures were considered. To achieve absorber performance from one side of the DSAMC structures, the loss-less PEC patches of that surface can be replaced with impedance patches that are optimized by the GA as well. In addition, structures with three FSS layers can also provide more flexibility for optimization of the non-absorbing face of the slab for AMC response.

Applying high permittivity dielectric loading ($\varepsilon_r > 1$) or utilizing substrates with magnetic properties ($\mu_r > 1$) can allow miniaturization of printed patch antennas. Utilization of magneto-dielectric materials ($\varepsilon_r > 1$ and $\mu_r > 1$) would provide increased miniaturization with improvements in the bandwidth performance as well. Unfortunately, most naturally occurring homogenous magnetic materials come with large losses which makes them unworkable at high frequencies. Kern *et al.* introduced a novel composite magneto-dielectric substitute, called metaferrites [12] as a possible way to address the need for magnetic materials ($\mu_r > 1$, $\varepsilon_r = 1$) that are usable beyond 1 GHz. In [12], they demonstrated that the properties of a PEC backed homogenous magnetic slab with frequency dependent permeability could effectively be achieved using a properly designed high-impedance Electromagnetic Bandgap (EBG) structures. In their simple planar configuration, a frequency selective surface (FSS) type structure was optimized and printed on top of a thin PEC backed dielectric substrate. It was also demonstrated that the real and imaginary parts of the effective permeability of an equivalent homogeneous magnetic slab ($\mu_r > 1$, $\varepsilon_r = 1$) could be related to the surface impedance values of the composite EBG structure.

A new design methodology is introduced here for creating matched impedance magneto-dielectric metamaterial (MIMDM) slabs ($\mu_r = \varepsilon_r > 1$), where a GA is combined with Periodic Method of Moments (PMM) code to optimize thin metallo-dielectric metasurfaces comprised of a periodic array of electrically small unit cells and backed by a perfectly conducting ground plane [13]. The technique is based on optimization of thin planar metallo-dielectric metasurfaces comprised of a periodic array of electrically small and rotationally symmetric unit cell structures sandwiched between two different dielectric slabs, one of which is backed by a perfectly conducting ground plane. Through optimization, the composite structure would behave as an equivalent of a PEC backed homogenous impedance matched magneto-dielectric ($\mu_r = \varepsilon_r > 1$) slab with an equivalent thickness of $d = t_1 + t_2$ as illustrated on the right of Figure 1-4.

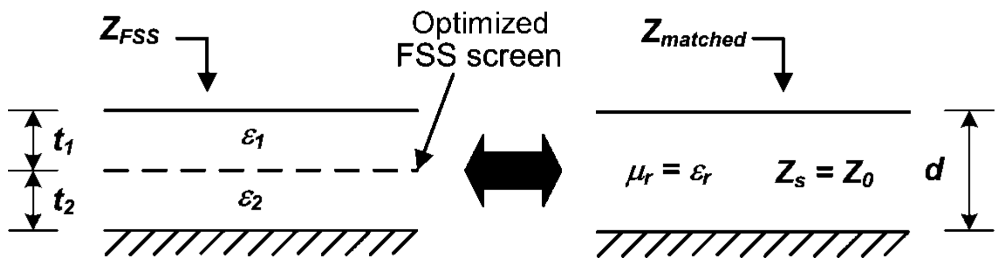

Figure 1-4: Cross-sectional diagram of the PEC backed optimized composite magneto-dielectric metamaterial structure (left) and its equivalent PEC backed homogenous ($\mu_r = \varepsilon_r > 1$) material structure (right).

The ability to optimize the design parameters of these thin planar composite metallo-dielectric structures also allows for the synthesis of low-loss matched-impedance magneto-dielectric metamaterials for planar antenna miniaturization and high-loss matched-impedance magneto-dielectric metamaterials for absorber applications. Moreover, these composite metallo-dielectric structures allow for the design of planar low-loss double-negative substrates as an alternative to volumetric split-ring resonators.

Optimized frequency selective surface (FSS) unit cells can be printed on grounded dielectric materials as tiled doubly periodic structures that behave as high impedance ground planes and operate as planar AMCs [14]. Miniaturization of an AMC unit cell provides a compact structure with an increased importance at the lower frequencies due to physical dimensional requirements. Some of the miniaturization techniques include FSS implementation of space filling curves or convoluted elements. Unfortunately, miniaturization usually comes at the cost of decreased operational bandwidth. Another technique utilizes in-phase alignment of the current vectors between closely placed wires so that currents reinforce increasing the self-inductance hence increasing effective length. In this technique, effective structures also extended from a single unit cell to the neighboring unit cells leading to increased effective length and reduced resonance frequency. Such tightly packing of the unit cells increases the capacitance among the neighboring unit cells enhancing the bandwidth of the AMC. The first resonant frequency of the surface is given by $\omega_o = 1/\sqrt{LC}$ and the bandwidth of a capacitive screen is proportional to $\sqrt{C/L}$ [15].

The proposed printed frequency selective surface (FSS) type unit cells come with an ultra-small periodicity, as shown in Figure 1-5, which provides aligned current vectors and interdigitated capacitance elements leading to much improved AMC bandwidth. While the dimensions of the unit cell is much smaller than the state-of-art AMCs in the literature, it can still provide the same bandwidth performance. The electrically much smaller dimensions of the proposed unit cell design make the AMC surface more attractive for use as a homogenous metamaterial and ninety degrees rotational symmetry makes it less sensitive to the polarization of the incident wave.

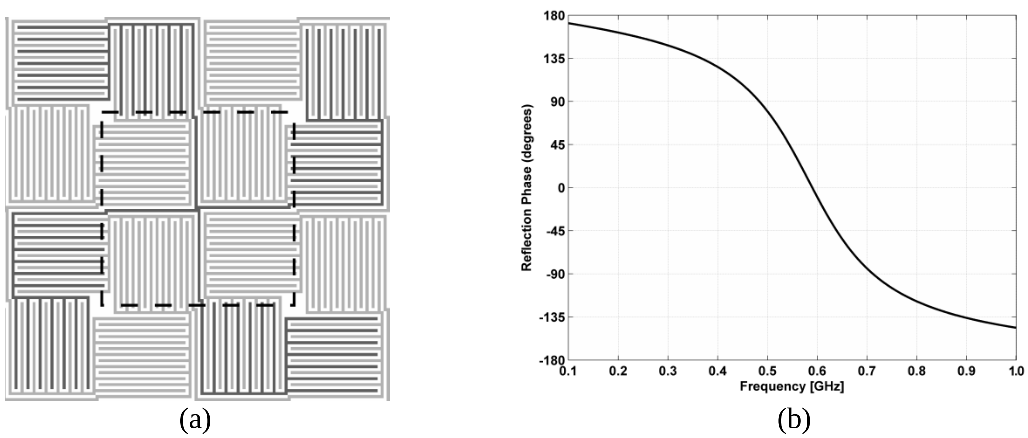

Figure 1-5: (a) The ultra-small AMC unit cell geometry is shown within the dashed square and it has interdigitated arms extending into neighboring unit cells as highlighted with the dark gray regions, (b) The reflection phase of the proposed design is centered at 600 MHz.

Another benefit of the FSS-based planar structures is the ease of fabrication of planar EBGs utilizing the printed circuit board (PCB) technologies. EBG structures can prevent the propagation of the surface waves in a certain range of frequencies and in order to reduce the mutual coupling between two patch antennas, Yang *et. al.* has proposed placement of mushroom type EBG structures between two patch antennas [16]. The patch antennas and the rectangular top shapes of the EBGs can be printed via PCB techniques but mushroom structures also require electrical connections to the PEC ground plane with the metallic vias through the dielectric. This makes the fabrication process cumbersome and their large mushroom shaped dimensions can reduce their practical usability.

A new design technique is introduced for the synthesis of planar FSS-based EBG structures to reduce the mutual coupling of the neighboring patch antennas. This EBG structure simply consists of a rotationally symmetric small unit cells that also extend into neighboring unit cells similar to the ultra-small AMC structures. Since it is a all planar surface, it does not require vertical metallic via connections to the ground plane and can be easily fabricated using conventional PCB fabrication techniques.

At last but not the least, different nature-inspired optimization algorithms are studied and utilized for various novel metamaterial surface design synthesis tasks as described previously. Genetic Algorithms is the most well-known numerical optimization algorithm that is extensively used in this dissertation, hence the theory behind this method will be discussed along with the implementations.

Clonal Selection Algorithm (CLONALG) artificially mimics the immune system of living vertebrates in which an efficient optimization method emerges. CLONALG is a relatively new to the electromagnetic optimization problems and multi-processor version of this algorithm is first implemented in here for optimization of various FSS filters at X-band. Using a Master/Worker parallel programming schema, CLONALG's almost embarrassingly parallel nature is exploited in this dissertation and shown that it is an efficient method to tackle multi-modal EM optimization problems.

In addition to the known nature-inspired optimization techniques, a new algorithm, named as the Wind Driven Optimization (WDO) is developed and implemented in this dissertation. This new algorithm is based on the atmospheric dynamics and Newtonian motion of the wind in our earth's atmosphere. The abstraction and artificial implementation of the motion of a infinitesimally small air parcel provides with unique properties that does not exist in similar algorithms like PSO and can be utilized as an efficient optimization tool with ease of implementation.

1.3. Original Contributions

The research that I conducted over the past four and a half years for my Ph.D. studies at the Pennsylvania State University has led to several new developments in the field of numerical optimization algorithms, meta-material synthesis and antenna design. The original contributions in these research areas and related publications are listed below for clarity:

- Introduced and optimized low profile stub-loaded inverted F-antenna (SLIFA) for high gain in the broadside direction [22].
- Developed and implemented the multi-processor version of the Clonal Selection Algorithm as Master/Worker parallel schema in FORTRAN 90 and MPI [20, 23].
- Proposed, developed and implemented a novel nature-inspired optimization algorithm, namely Wind Driven Optimization (WDO) technique [7, 18].
- Implemented Parallel CLONALG code to synthesize multi-layered Frequency Selective Surfaces (FSS) for operation in the X-Band from 8 GHz to 12 GHz [23].
- Introduced a synthesis technique utilizing Genetic Algorithms for designing thin double-sided FSS structures as Artificial Magnetic Conductor (AMC) ground planes eliminating the need for complete PEC ground plane backing in composite low profile antenna systems [10].

- Optimized a thin double-sided AMC (DSAMC) ground plane that has a band-stop AMC property at the operating frequency and pass-band outside the target frequency range [19].
- Optimized multi-band DSAMC ground planes that can be synthesized for multi-frequency bands of operation [19].
- Designed and optimized DSAMC structures that are tailored to operate as an absorber on one side and AMC on the other [19].
- Designed and optimized DSAMC separator where its either side is independently optimized for two vertical monopole-type antennas of diverse operating frequencies which can efficiently operate and still occupy a smaller footprint [11, 19].
- Designed and optimized matched impedance magneto-dielectric metamaterial (MIMDM) slabs to address the need for matched impedance magneto-dielectric materials that are usable at high frequencies [13]. Optimized designs include MIMDMs with double-positive or double-negative constitutive parameters.
- Synthesized low-loss MIMDMs for dual-band operation and lossy MIMDM slabs for single and dual-band absorber applications [21, 24].
- Designed, optimized and demonstrated the utility of MIMDMs as substrates for miniaturized rectangular patch antennas.
- Designed and optimized ultra-small unit cell AMC structures that provide identical bandwidth performance as the current state of the art AMCs, and can be optimized with the precise control of the operating frequency band [17].
- Designed small unit cell electromagnetic bandgap (EBG) structures to be incorporated in the design of microstrip antenna arrays to reduce the strong mutual coupling.

1.4. Overview

The research in this dissertation introduces several novel methods for synthesizing artificial magnetic conductors, magneto-dielectric surfaces, electromagnetic bandgap structures, thin planar metamaterial absorbers and new ways to implement numerical optimization algorithms. This section provides an overview of the following chapters.

Chapter 2 studies the working structure of the well known Genetic Algorithms and discusses the implementation for the optimization of various surfaces in this dissertation.

Chapter 3 discusses the Clonal Selection Theory and the implementation of the algorithm in parallel Master/Worker schema. A numerical benchmark study is carried out for parameter selection and the performance of the parallel CLONALG implementation is compared against a binary-valued Genetic Algorithm. Optimization of the three different X-band frequency selective surfaces are also presented.

Chapter 4 introduces and develops a novel numerical nature-inspired optimization algorithm called the Wind Driven Optimization. The theory behind the physical equations is presented where the working structure of the WDO algorithm is established. Additionally, multiple electromagnetics design and optimization examples are presented. These examples include linear antenna array synthesis, double-sided AMC synthesis, and optimization of low profile stub-loaded inverted-F antennas.

Chapter 5 introduces the thin double-sided artificial magnetic conductor (DSAMC) designs and develops various design examples targeting different applications. The utility of such designs are shown by the optimization of thin DSAMCs at 10 GHz, the dual band optimization of the DSAMCs, band-selective DSAMC design optimization, and absorber DSAMC designs. Its application to a system problem, where the utility of a thin DSAMC separator is illustrated with two vertical monopoles, which were operating at Wi-Fi frequencies of 2.4 GHz and 5.2 GHz.

Chapter 6 discusses the synthesis of matched-impedance magneto-dielectric meta-surfaces (MIMDM) for use at high frequencies. Designs include MIMDMs with low-loss double-positive or double-negative constitutive parameters for single band operations, MIMDMs for dual-band operations, absorber designs and a system problem for miniaturization of patch antennas by using MIMDMs as substrates.

Chapter 7 introduces ultra-small unit cell AMC structures and illustrates the improvements achieved over the state-of-the-art in AMC design. Improvements such as the ultra-small unit cell size provides better field of view while preserving the AMC operational bandwidth.

As an extension of ultra-small unit cell AMC structures, small size planar rotationally symmetrci electromagnetic bandgap structures can be synthesized for mutual coupling reduction in patch antenna arrays, which is presented in Chapter 8.

The last chapter is Chapter 9, which provides a conclusion to this dissertation as well as suggestions for future work.

Chapter 2

Genetic Algorithms (GA)

This chapter discusses the theory behind the Genetic Algorithms (GA), provides the terminology for later use, discusses some of the related literature as it has been utilized to solve electromagnetic optimization problems and also provides an overview of the implementation for tackling the synthesis of the novel metamaterial surfaces presented in this dissertation.

2.1. Theory and Terminology

As one of the oldest nature-inspired optimization algorithms, the GA has received increasing attention over the years from various fields including science, engineering, economics and social sciences. Since it was first introduced by John Holland in 1975 [25], there have been many studies on the operators of the algorithm, many attempts to improve its performance and many variants were proposed targeting discrete-valued or continuous-valued parameters, multi-objective problems as well as other hybridization attempts. Unfortunately, it would be impossible to cover all the details of the algorithm here, yet a simplified overview will follow.

In its simplest form, the Genetic Algorithm is the artificial implementation on computers of the biological processes of genetics, Darwin's theory of evolution and survival of the fittest theory applied for solving complex numerical optimization problems. It offers a robust alternative to the gradient based search algorithms with unique properties such as the ability to operate in non-differentiable or non-continues search spaces, continuous- or discrete-valued parameters, multi-dimensional and/or multi-modal problems as well as multi-objective optimization and ability to work with constraints.

In essence, the genetics is the biological study of heredity and the word stems from the word "gene" [26]. The building blocks for each living organism are encoded in the double-helical molecule called deoxyribonucleic acid, *i.e.* DNA, and a gene can be thought as a small segment of the DNA. The collection of many genes dictate the production of the proteins where the exact timing, rate of production and sequence of amino acids in the proteins provide the inherent properties to each unique species and to each individual. Long DNA molecules are aligned and categorized into chromosomes, where an individual's unique properties are encoded and controlled through the genes and through genes' ability to control the protein production within the living organism. Detailed biological description of 'genetics' can be found in [26]. In the implementation of the GA, an individual candidate solution to the optimization problem is also referred as a chromosome. The parameters of the optimization problem, *i.e.* dimensions, are the genes and each gene contains encoded information about the corresponding parameter. For example, if we optimize a rectangular patch antenna for best input impedance performance, the length and the width of the antenna would constitute the two parameters (or dimensions) of this optimization problem as seen in Figure 2-1. The combination of these two parameters create a chromosome [P1 P2] and each unique chromosome represents a solution to the antenna optimization with different dimension values. This coding schema provides mapping from the parameter space to chromosomes, where the parameter space could be continuous- or discrete-valued and chromosome space is usually a finite-length binary string as seen in Figure 2-1 (b).

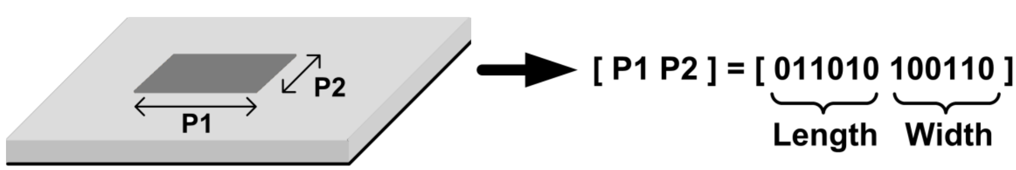

(a) (b)

Figure 2-1: (a) A sample patch antenna optimization problem, where the dimensions of the rectangular patch antenna is optimized, (b) Chromosome representation of the optimization parameters, where binary coded chromosome is also shown as [P1, P2].

GA is a population based iterative algorithm, where a group of predetermined number of chromosomes is known as the *population*, and each iteration is known as the *generation*. A comprehensive list of GA terminology is presented in Table 2-1. At each generation, the whole population undergoes *fitness evaluation*, *selection*, *crossover* and *mutation*. Fitness evaluation is to determine which chromosomes provide the best candidate solutions, *i.e.* best fitness, at that particular iteration and which ones deserve to survive and create offsprings. This is to mimic the survival of the fittest principle as well as to let children chromosomes inherit good genetic properties from their parents. The population is then ranked based on their fitness for the selection process. As it is desired to preserve and carry over the good traits of parents, it is also critical to allow a certain level of randomness in the algorithm so that the population is rather diverse and the method does not lose it exploration ability.

Table 2-1: Genetic Algorithms terminology and their descriptions.

Terminology	**Description**
Gene	Numerical encoding of one of the optimization dimensions.
Chromosome	Combination of all genes, *i.e.* numerical coding of all optimization dimensions.
Population	A group of predetermined number of individual chromosomes.
Generation	One iteration, where genetic operators are applied.
Parent	A chromosome of the present iteration, where selected two or more chromosomes produce children for the following generation.
Child (Offspring)	A chromosome of the upcoming iteration, where it is created through crossover by combination of two parents or in some cases through mutation of a single parent.
Fitness / Cost	An assigned number to each chromosome at each iteration based on their proximity to the global solution or to the desired optimization performance.
Selection	Genetic operator for choosing parents to produce child-chromosomes.
Crossover	Genetic operator to combine two or more parent chromosomes to generate new chromosomes, *i.e.* child-chromosomes.
Mutation	Genetic operator to randomly alter some of the genetic information to simulate the unexpected external influences during gene duplication.
Niching	Carrying the best chromosome of present iteration unaltered to the next iteration.
Ranking	Sorting the chromosomes at each iteration based on their fitness.

As the artificial implementation of natural selection is applied to the ranked population, a certain percentage chromosomes are discarded due to their low fitness. The ones that survive then undergo the selection process for mating, *i.e.* crossover, where different methods can be implemented for the selection of mates. Two of the most popular methods are the roulette-wheel selection (RWS) schema and the tournament selection (TS) schema. In RWS schema, the chromosomes are assigned the highest probability of being selected in a decreasing fashion starting from the fittest to the least fittest as seen in Figure 2-2 (a). The chromosome with highest fitness has the highest probability of being selected and the one with lowest fitness has the lowest probability of being selected among the surviving chromosomes. On the other hand, in TS schema, a certain percentage of chromosomes is selected at random from the population, and the fittest individual out of this sub-population is selected for mating as illustrated in Figure 2-2 (b).

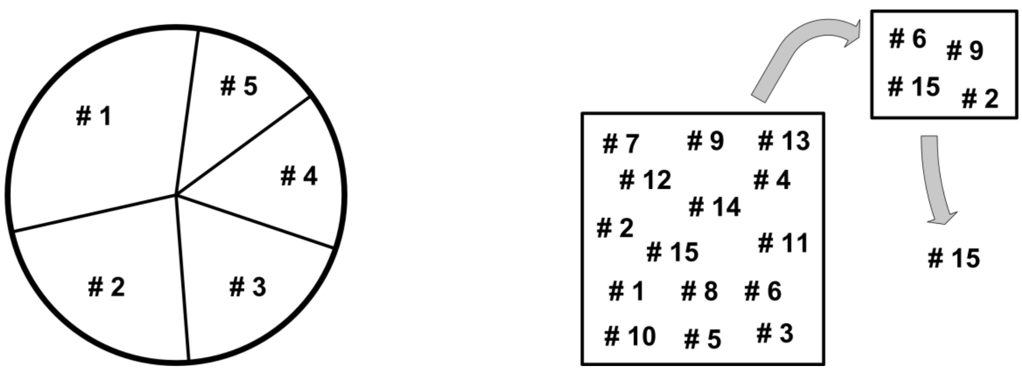

(a) (b)

Figure 2-2: (a) Roulette wheel selection for a population of ranked five chromosomes, (b) Tournament selection for an unsorted population of fifteen chromosomes.

Once the mates are selected, then the reproduction, *i.e.* crossover, stage is carried out. At this stage, a point on the parent chromosomes is randomly selected and chromosomes are divided into parts. The divided parts are then crossed-over between two parents to construct two new individual chromosomes, *i.e.* child chromosomes. This is called single-point crossover operation with two parents where multi-point crossover or more sophisticated crossover operators with more than two parents can be found in the literature [5]. Figure 2-3 illustrates a simple crossover operation where two parent chromosomes generate two child-chromosomes and their genetic information is combined with the hope that two fit parents would give life to children with higher fitness than themselves. Yet, this is may not always be the case.

Parent 1 = [0110101001101 / 1010011] **Child 1 = [01101010011010110101]**

Parent 2 = [1110001010010 / 0110101] **Child 2 = [11100010100101010011]**

Figure 2-3: Illustration of the single-point crossover with two parents with binary coded chromosomes to produce two new offsprings.

With the crossover operation, the population reaches back to its full size that it started with and then the whole population undergoes mutation operation. At this point, it is crucial to point out that different variations of GA implementation have been proposed where some versions omit the implementation of crossover and produce offsprings only through mutation operation, or vice versa. As such methods are completely acceptable, they may not provide the best outcome for all the optimization problems. From experience, it has been observed that utilization of all genetic operators provide increased robustness to the algorithm and makes it more general and better performing global optimization technique for wide variety of electromagnetic synthesis problems.

The crossover operation helps preservation of the genetic information that is carried over to next generations, which overtime may cause all chromosomes to have nearly identical chromosomes. On the other hand, the mutation operation provides a mean to diversify the population by introducing random changes to the genetic information. For a binary coded chromosome this is simply achieved by flipping '1' to '0' or vice versa at certain amounts [27].

This is to mimic the unexpected changes in our DNAs which might be caused by internal or external forces. The amount of mutation and how they implemented can vary depending on the implementation but an illustration of two bit random mutation of a binary chromosome is illustrated in Figure 2-4. While the mutation introduces new genetic information to the population, it may or may not be helpful in terms of the performance of the optimization algorithm. Too much mutation could introduce too much diversity and hinder the progression towards a global solution yet too little mutation may allow the algorithm become extremely greedy and converge to non optimal solution.

Chromosome = [0110101001101011 0101]
Mutated Chromosome = [0110111001101010 0101]

Figure 2-4: A simple mutation operation on a binary chromosome where two bits are mutated.

Once the mutation operation is completed, a brand new population has been generated. The iterative process starts over again with the evaluation of fitness, and progresses through each genetic operations targeting improved performance after each iterations. In the case of electromagnetic optimization problems, there can be multiple different solutions that satisfy the desired performance criteria. Continuing with the patch antenna design example, it might be desired a good input impedance performance as well as good gain at the broadside of the antenna. A simple fitness function would incorporate the desired performance of the optimized structure as seen below;

$$Fitness = |Gain_{chrom} - Gain_{desired}| + |VSWR_{chrom} - VSWR_{desired}| \qquad (2\text{-}1)$$

where $Gain_{chrom}$ and $VSWR_{chrom}$ are the gain and VSWR performance of a single chromosome and $Gain_{desired}$ and $VSWR_{desired}$ are the minimum desired performance we would like to achieve.

2.2. Related Literature Overview

As the theory behind the Genetic Algorithm is outlined in the previous section, it would be beneficial to provide an overview on the electromagnetics literature that have utilized GA for optimization. GA has been utilized to optimize individual antenna elements [28 - 33] covering from simple wire antennas to complex printed antenna elements in application to GPS, RADAR, Marine and satellite systems as well as optimization of the antenna arrays [34 - 37] targeting array thinning, side lobe reduction, radiation pattern synthesis, coupling reduction including novel methods to synthesize ultra-wide-band arrays. Yet, we still could not do justice to the field, where successful application of GA covers and goes beyond design of various absorbers [38 - 42], synthesis of frequency selective surfaces [43 - 45], design of novel electromagnetic bandgap structures [46, 47], and metamaterials covering a wide range of frequencies [12, 14, 34, 35, 40, 41]. Building on top of proven track record of GA, this dissertation also utilizes this optimization method for design synthesis of novel ultra-small or very thin metamaterial surfaces for various applications.

2.3. Implementation Overview

In the design synthesis of novel metamaterials and frequency selective surfaces, the GA is utilized to optimize the unit cell geometry, the appropriate dielectric material thicknesses, dielectric constants and loss tangents as well as the unit cell size that yields the desired responses. For fast numerical analysis of these composite structures, the GA is either linked with an in-house developed full-wave numerical solvers such as the Periodic Method of Moments (PMM) method and Periodic Finite Element Boundary Integral (PFEBI) method, or commercially available software such as the FEKO, Ansoft HFSS or CST Microwave Studio. The material thicknesses, the dielectric constants, loss tangents and unit cell sizes would constitute the continuous-valued optimization dimensions, where as the pixilated unit cell geometry would constitute a discrete-valued dimension. Considering that the metallic pixel geometries are printed on top of dielectric materials, then Figure 2-5 illustrates the unit cell geometry mapping to the chromosomes, where existence of a metallic pixel is represented by a "1" and the absence of the metal is represented with a "0" in the chromosome. The total number of "1" and "0" would represent the total length of the chromosome, where the GA might have difficulty with extremely long chromosomes. To simplify the geometry and reduce the number of bits, various degrees of symmetry can be applied. Along these lines, Figure 2-5 (a) represents an eight-folded symmetry where as Figure 2-5 (b) represents an four-folded symmetry.

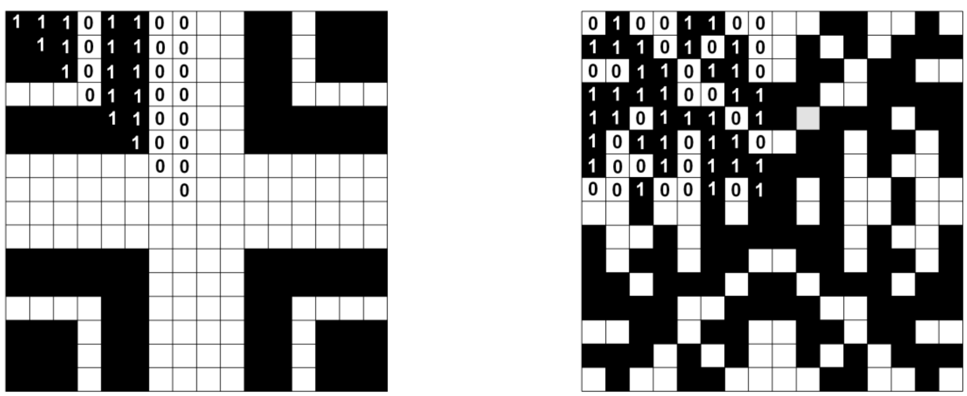

(a) (b)

Figure 2-5: Sample unit cell geometries showing the mapping of the pixelization to the binary chromosomes of the GA optimization. (a) Eight-folded symmetry is applied, (b) Four-folded symmetry applied. Black shaded pixels represent the PEC, and white shaded pixels represent the absence of the PEC where the dielectric is exposed.

The algorithm starts with the initialization where the dimensions of the optimization problem are defined and how they mapped to the chromosomes. A fitness function states the desired performance criteria and then the initial population is generated. The fitness of the all population is evaluated and the population is ranked. Inferior individuals are discarded, fit members are selected for reproduction and the population is refilled with offsprings. Then mutation is applied to the population to diversify the genetic information. As seen in the flowchart in Figure 2-6, the fitness of the new population is evaluated and the iterative process continues. One can implement one of the two stop criteria, where optimization is allowed until a predetermined number of iterations are exhausted or one can set a desired fitness threshold and the optimization is terminated as soon as the desired objectives are achieved. Such choices depend on the problem and personal preferences of the designer.

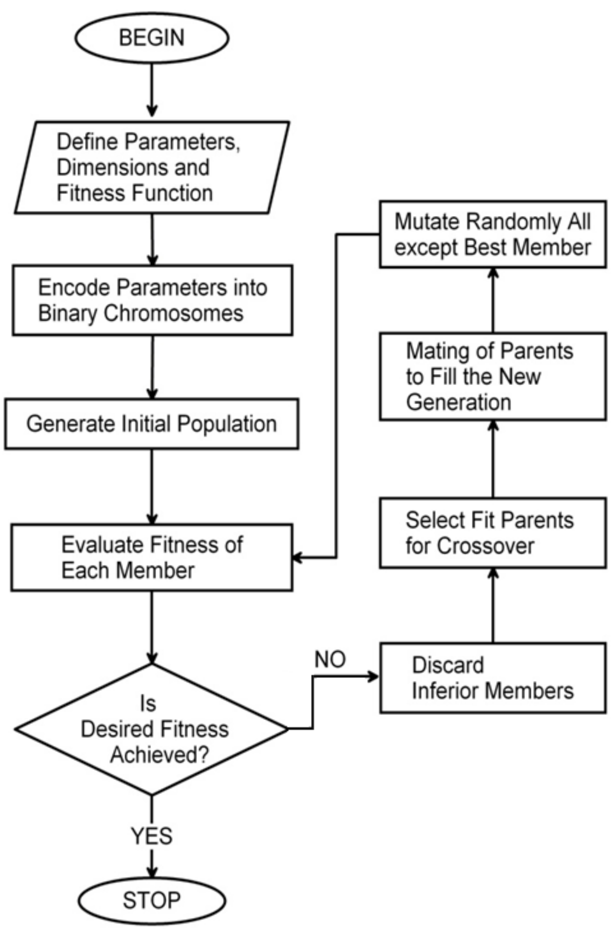

Figure 2-6: Sample flowchart for a typical Genetic Algorithm implementation, demonstrating the creation of each generation and the fitness evaluation of each member of the population.

Chapter 3

Clonal Selection Algorithm (CLONALG) Optimization Method

This chapter discusses the theory behind the Clonal Selection Algorithm (CLONALG) and introduces a parallel programming schema to exploit the embarrassingly parallel nature of the method to alleviate the burden created by the large clone population during the optimization. A parameter study and performance comparison will be made against the well known binary Genetic Algorithm and efficiency of the CLONALG will be studied when given the task to optimize multi-layered Frequency Selective Surface (FSS) filters in the X-band.

3.1. Introduction

Many of the Artificial Immune System (AIS) algorithms were inspired by biological immune processes in living vertebrates, where each algorithm exploits different working structures found within the biological immune system. The Clonal Selection Algorithm (CLONALG), which combines the clonal selection principle with the affinity maturation process, is one of the several AIS algorithms that has already been used to tackle various problems in science and engineering [50]. Clonal selection principle based AIS algorithms have been successfully applied to network intrusion detection [51], robotic system control [52], data mining [53], [54], and optimization [55], [56]. Similar to other nature-inspired numerical optimization techniques, CLONALG is a population based, iterative, heuristic global optimization method. The population consists of individual antibodies, where each antibody represents a candidate solution to the problem at hand. Those antibodies that successfully recognize the invading antigens have higher affinity, *i.e.* they present a better solution potential, and are selected to proliferate [55]. High affinity antibodies then undergo an evolution-based maturation process, allowing the algorithm to iteratively progress towards finding a global and best solution to the optimization problem. CLONALG has been shown to be very effective on multimodal problems due to its inherent properties, yet it has not become a popular choice as an optimization tool in the electromagnetics community. The primary reason for this is the large number of clones generated at each iteration, which increases the population size drastically as compared with other nature-inspired global optimization techniques and also the associated computational burden when used in conjunction with a full-wave electromagnetic solver. The lack of interest in the application of CLONALG within the electromagnetics community can be observed by the low number of manuscripts published. Campelo *et al.* [57], [58] have demonstrated CLONALG in the optimization of TEAM Workshop problem 22, which involves the minimization of the stray field in a superconducting magnetic energy storage (SMES) device, and also in the design of loudspeakers [59]. Batista *et al.* [60] have also tackled the TEAM Workshop problem 22 with a modified version of CLONALG, where different types of random noise distributions were applied in the mutation operator, and a multi-objective version of their code was utilized to optimize a microwave heating device in [61]. Ke *et al*. [62] have utilized CLONALG in channel estimation for MIMO systems, while Babayigit *et al.* [63] – [65] have used CLONALG in linear phased arrays synthesis.

In this chapter, it is demonstrated that a parallel implementation of CLONALG via Message Passing Interface (MPI) would decrease the computational burden of multiple calls to the full-wave electromagnetic solver by distributing the work load over multiple processors, thus making CLONALG an effective alternative to other popular nature-based optimizers. In order to demonstrate the effectiveness of the parallel CLONALG implementation, multi-layered frequency selective surface (FSS) filters for the X-band were chosen for optimization. FSS are spatial filters, comprised of 2-D periodic metallic screens separated by dielectric layers [66] and have been extensively investigated for a variety of electromagnetic applications such as radomes, absorbers, electromagnetic bandgap materials, and metamaterials [14, 67, 68]. FSS synthesis provides an excellent test bed for CLONALG optimization because it is a challenging design problem with many parameters and multiple local minima within the search space. In the past, Genetic Algorithms (GA) have been successfully applied to design FSS for a variety of applications [5, 14, 45, 68, 69]. In this chapter, parallel CLONALG implementation will be compared against the more traditional parallel GA optimizer [70] in order to demonstrate its effectiveness as an alternative optimization tool for use in electromagnetics design synthesis.

3.2. Artificial Immune System and Clonal Selection Algorithm

A biological immune system has the ability to differentiate between self and non-self protein structures and can generate specific responses based on the type and the origin of the protein molecules it encounters [71]. It is fault tolerant, adaptive, and can maintain diversity with the ability to respond to molecules that have never been encountered. It can detect anomalies in a distributed manner and perform reinforced learning, which means that it has memory and can learn over time [56]. Some of these intrinsic biological immune system properties can be found in the CLONALG and enable its successful employment to perform various tasks, including pattern recognition, machine learning, network intrusion detection, data mining, and optimization [55].

Early theories of acquired immunity describe the infected host as being passive [72]. However, clonal selection theory [73] postulates that the host is active and contains a large repertoire of antigen-specific T- and B-lymphocytes, even before antigen (Ag) contact occurs, and upon first encounter, the pool of lymphocytes can actively recognize the foreign antigens. As illustrated in Figure 3-1, the identification process occurs if the Ag-specific antibody (Ab) molecules that are attached to B-lymphocytes bind to the surface of the Ag to achieve recognition. Once recognition is achieved, bone marrow derived (B-) lymphocytes proliferate and differentiate into short-lived plasma cells that secrete antibody molecules against the recognized antigen stimuli for an immediate defensive response. Part of the B-lymphocytes also differentiate into long-lived memory cells circulating in the bloodstream that, in fact, constitute the large repertoire of Ab as seen at the first stage of the immune response. If the same Ag or a derivative of that Ag is encountered again during the lifetime of the host, the immune system response would be much faster and stronger due to the existence of these memory cells. Further details on acquired immunity and clonal selection theory can be found in [55], [71] and [73].

The CLONALG is an artificial implementation of the acquired immune response to malicious external stimuli, *i.e.* antigens (Ag), in living vertebrates [74], which simply combines the clonal selection principle with the affinity maturation process. It is a population based, iterative, and heuristic numerical optimization technique in which members (antibodies) with high affinity (high fitness) proliferate [57] and generate a number of clones proportionate with their affinity ranking (fitness ranking) within the population. At each iteration, population members are ranked in descending order based on their affinity, or ability to recognize malicious stimuli, *i.e.* Ag. In the case of an optimization problem, population members are ranked based on their closeness to the global optimum. The number of clones that each member generates, N^i_C, is determined by its affinity ranking, i, in the population as given by

$$N_C^i = ceil\left[\frac{\beta\, N_{pop}}{i}\right], \tag{3-1}$$

where N_{pop} is the population size and β is a multiplying factor that is chosen empirically.

The newly generated clones undergo a hypermutation process [75], in which each dimension of a clone is altered stochastically based on

$$x_i^{new} = (1-\rho)\, x_i^{old} + (\rho\, x_k^{old}) \qquad \text{if } R_N < 0.2\ , \tag{3-2}$$

where R_N and ρ are random numbers with uniform distributions from 0 to 1. If R_N for a given dimension is less than the threshold value of 0.2, the old value for that dimension, x_i^{old} , is replaced by the new value x_i^{new}, derived from x_i^{old} and the value for another dimension of the same clone, x_k^{old}. In addition to hypermutation, a percentage (d) of the low affinity members are deleted and replaced with newly generated members at each iteration.

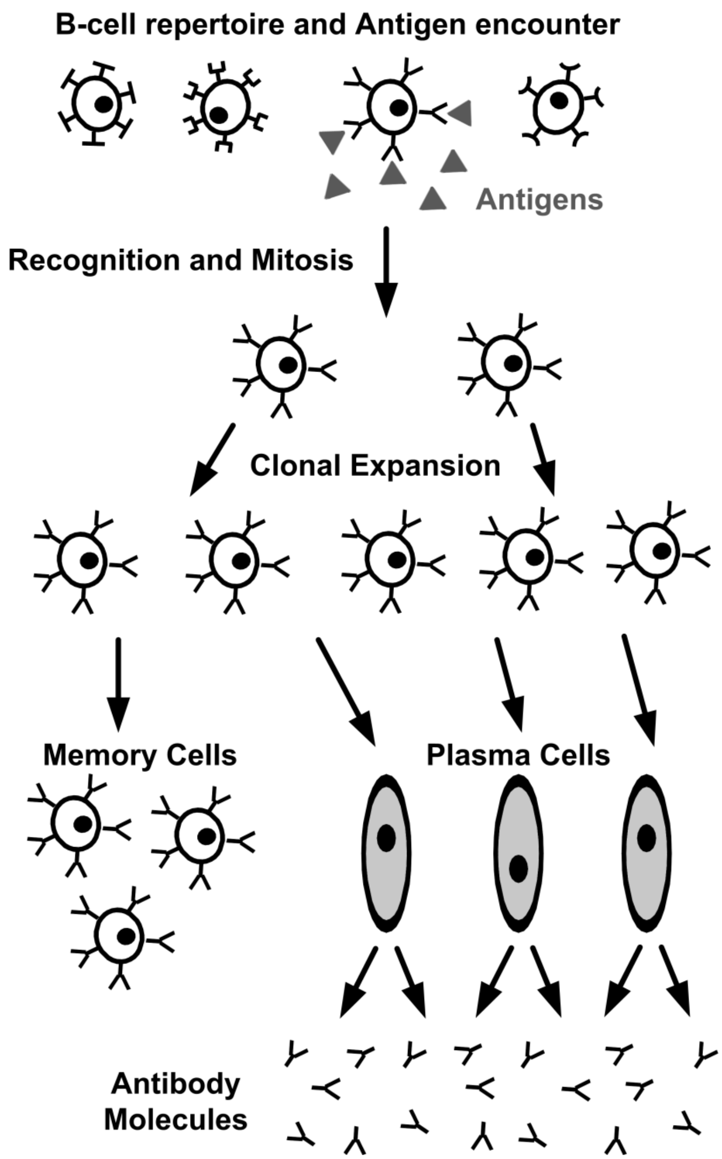

Figure 3-1: Biological clonal selection process as observed in living vertebrates.

In order to maintain diversity during the optimization process, each clone is only allowed to compete with its own parent and other clones from the same parent. The clone with the highest affinity then replaces the parent, provided it has higher affinity than the parent.

In the implementation of CLONALG, shown in Figure 3-2, Message Passing Interface (MPI) is utilized to distribute the work load to multiple processors in order to mitigate the burden of multiple calls to the full-wave electromagnetic solver at each iteration. In this parallel implementation, a master/worker schema is employed, where the master processor is responsible for executing the algorithm's tasks, such as reading the input data, affinity-based cloning, hypermutation, and replacing low affinity members. On the other hand, the worker processors are responsible for executing the full-wave EM solver given the design parameters of each clone provided by the master processor and returning the computed affinity values.

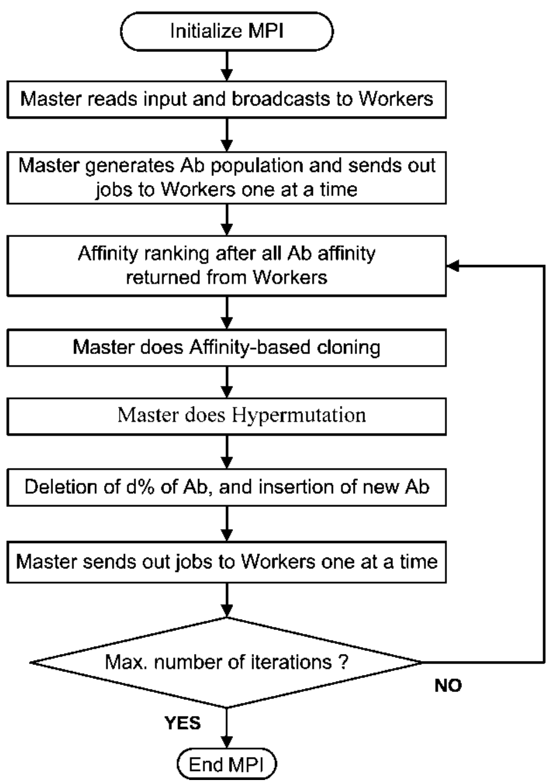

Figure 3-2: Flowchart showing the parallel CLONALG in a Master/Worker MPI schema.

This parallel implementation is more complicated than other parallel schemes, but it provides the best load balancing. The iterative procedure continues until a pre-set number of generations is exhausted. The performance of the CLONALG primarily depends on the selection of the parameters that are utilized in (3-1) and (3-2), which are N_{pop}, β and d. In order to determine the best combination of these parameters, benchmark testing of the parallel CLONALG implementation is carried out with four different test functions in Section 3.4.

3.3. Parallel Genetic Algorithm Overview

The GA is one of the earliest nature-inspired optimization algorithms and has proven to be both effective and popular within the electromagnetics community [5], which was introduced and studied previously in more detail in Chapter 2.

In this chapter, David Carroll's binary coded GA driver [70] was used in parallel schema utilizing MPI in order to speed up the GA iterations, during which many calls must be made to the full-wave electromagnetic solver. If the simulation of each chromosome is considered as a single task to be executed, the entire population of chromosomes is divided into an equal number of tasks per processor and distributed equally to all processors including the one with MPI rank zero. This functional decomposition simplifies the parallel programming model at the expense of load balancing. All of the algorithm's tasks such as reading the input data, selection, crossover, and mutation to the population are handled by the processor with MPI rank zero. The flowchart shown in Figure 3-3 illustrates the parallel GA optimization scheme. Default settings for the GA operators are utilized as suggested by Carroll [70]. Tournament selection is combined with a uniform crossover operator to generate the offspring. Both of the available mutation operators, *i.e.* creep mutation and jump mutation, are utilized with built-in niching and elitism mechanisms.

These default parameter settings along with a study of other parameters are presented in the next section.

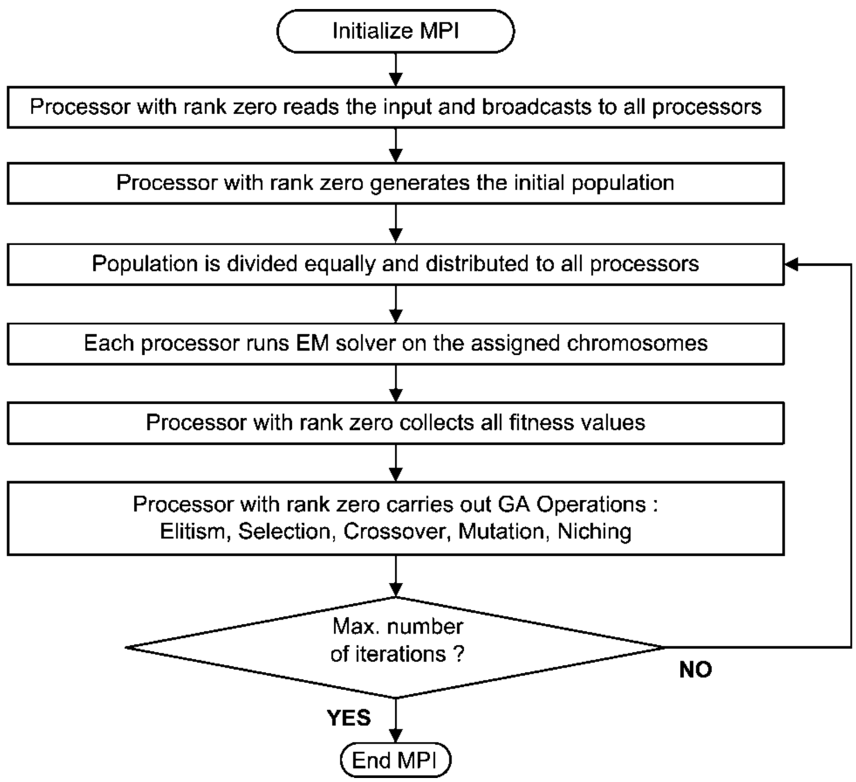

Figure 3-3: Flowchart showing the parallel GA implementation.

3.4. Parameter Studies with Test Functions

A parameter study for the GA and CLONALG is carried out using two unimodal and two multimodal test functions to determine the optimum parameter values for each algorithm. The unimodal test functions are the *Sphere* and *Rotated Hyper-Ellipsoid* functions, whereas the *Ackley* and *Rastrigin* functions are multimodal. The selected functions and their optimal set of values can be found in Table 3-1. The dimensionality of the test functions for the parametric study was chosen to be the same as the frequency selective surface (FSS) optimization problem, which is set to N=12 dimensions. The optimum performance of the CLONALG primarily depends on the selection of the parameters β, N_{pop} and d, which are utilized in (3-1) and (3-2). It is preferred that each of these parameters are maintained as small as possible because they have a direct influence on the number of clones generated at every iteration. By keeping β, N_{pop} and d small, the optimization runs efficiently, requiring fewer calls to the electromagnetic solver.

Table 3-1: Test functions used to compare CLONALG and GA numerically. All functions are N-dimensional, x is a vector of length N, and the optimal set of each function is represented by x*.

Function	Description
Sphere	$F_{SPH}\left(\mathbf{x}\right)=\sum_{i=1}^{N}x_i^2$ $x_i \in [-10,10]$, $\mathbf{x}^*=\left(0,0,...,0\right)$, $F_{SPH}\left(\mathbf{x}^*\right)=0$
Ackley	$F_{ACK}\left(\mathbf{x}\right)=20+e-20\exp\left(-0.2\sqrt{\frac{1}{N}\sum_{i=1}^{N}x_i^2}\right)-\exp\left(\frac{1}{N}\sum_{i=1}^{N}\cos(2\pi x_i)\right)$ $x_i \in [-32,32]$, $\mathbf{x}^*=\left(0,0,...,0\right)$, $F_{ACK}\left(\mathbf{x}^*\right)=0$
Rastrigin	$F_{RAS}\left(\mathbf{x}\right)=10N+\sum_{i=1}^{N}\left(x_i^2-10\cos(2\pi x_i)\right)$ $x_i \in [-5,5]$, $\mathbf{x}^*=\left(0,0,...,0\right)$, $F_{RAS}\left(\mathbf{x}^*\right)=0$
Rotated Hyper-ellipsoid (RHE)	$F_{RHE}\left(\mathbf{x}\right)=\sum_{i=1}^{N}\left(\sum_{j=1}^{i}x_j\right)^2$ $x_i \in [-65.536,\ 65.536]$, $\mathbf{x}^*=\left(0,0,...,0\right)$, $F_{RHE}\left(\mathbf{x}^*\right)=0$

In the parametric study for CLONALG, all possible combinations of population sizes N_{pop} = [20, 30, 40, 50], d = [0, 10, 20, 30, 40, 50, 60, 70, 80, 90] and β = [0.1, 0.3, 0.5, 0.7, 0.9, 1.1, 1.3, 1.5, 1.7, 1.9] were tested. For each combination, 10 trials were run for a maximum of 200 iterations using the N=12 dimension benchmark functions. The acceptable convergence threshold for the real-valued CLONALG was set to a *Cost* value of 10^{-6}, where *Cost* is the difference between the test function value and the optimal function value. The average final *Cost* of 10 trials for each test function is plotted in Figure 3-4, Figure 3-5, Figure 3-6, and Figure 3-7, for the *Sphere*, *Ackley*, *Rastrigin*, and *Rotated Hyper-Ellipsoid* functions, respectively. In each figure four subplots are shown, representing different population sizes of N_{pop} = [20, 30, 40, 50]. Yellow highlighted regions in these plots illustrate parameter combinations that achieved an average *Cost* within the acceptable threshold of 10^{-6} in less than 200 iterations over 10 trial runs per combination.

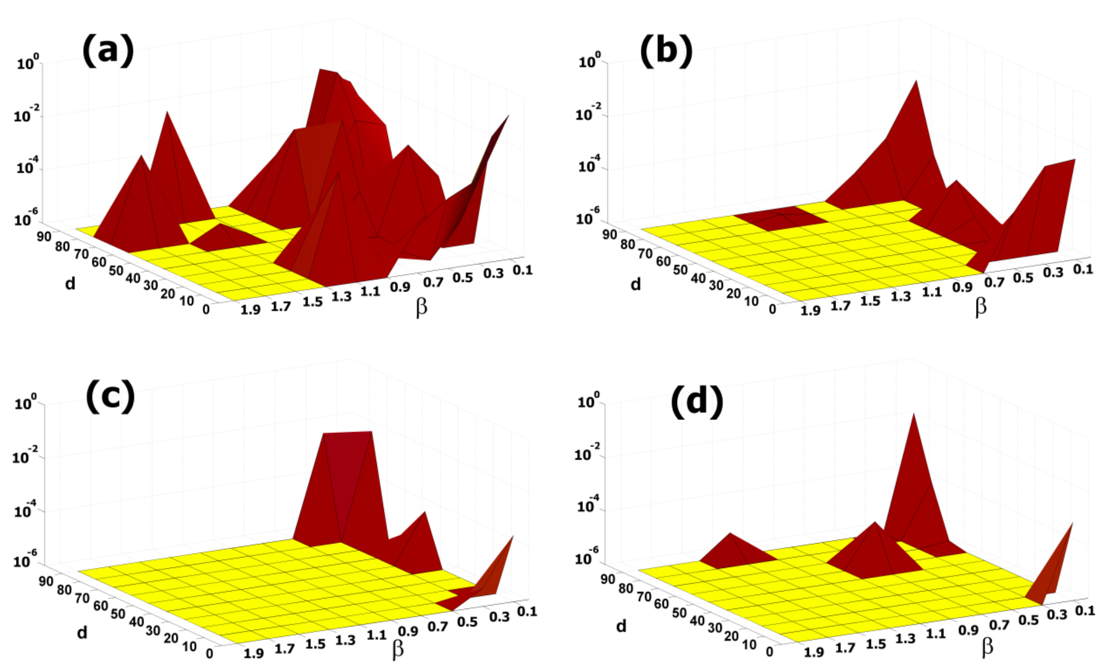

Figure 3-4: CLONALG *Cost* performance results with the *Sphere* test function for varying β and d, tested using four different values of (a) N_{pop} = 20, (b) N_{pop} = 30, (c) N_{pop} = 40, and (d) N_{pop} = 50. Yellow highlighted regions illustrate the parameter combinations which achieved the desired cost of 10^{-6} in less than 200 iterations.

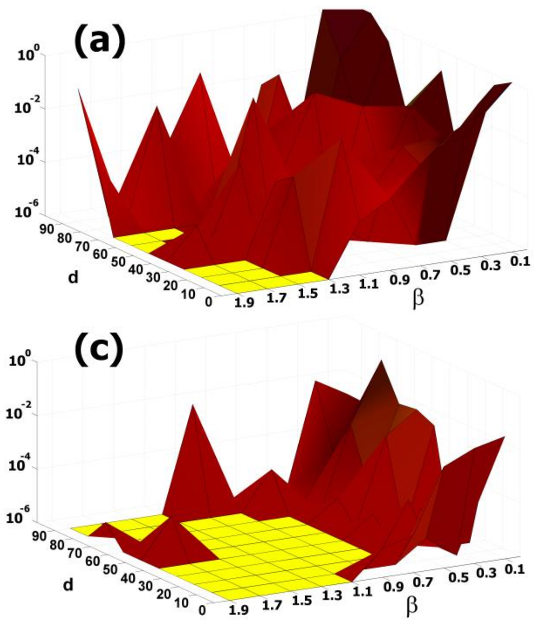

Figure 3-5: CLONALG *Cost* performance results with the *Ackley* test function for varying β and d, tested using four different values of (a) N_{pop} = 20, (b) N_{pop} = 30, (c) N_{pop} = 40, and (d) N_{pop} = 50. Yellow highlighted regions illustrate the parameter combinations which achieved the desired cost of 10^{-6} in less than 200 iterations.

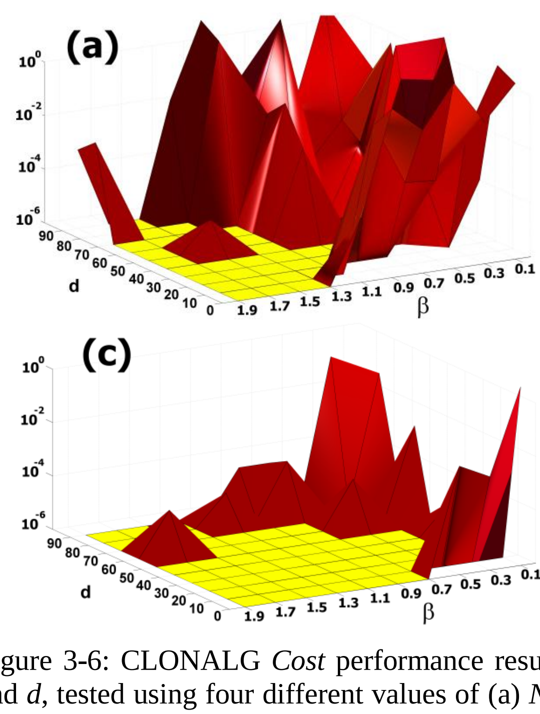

Figure 3-6: CLONALG *Cost* performance results with the *Rastrigin* test function for varying β and d, tested using four different values of (a) N_{pop} = 20, (b) N_{pop} = 30, (c) N_{pop} = 40, and (d) N_{pop} = 50. Yellow highlighted regions illustrate the parameter combinations which achieved the desired cost of 10^{-6} in less than 200 iterations.

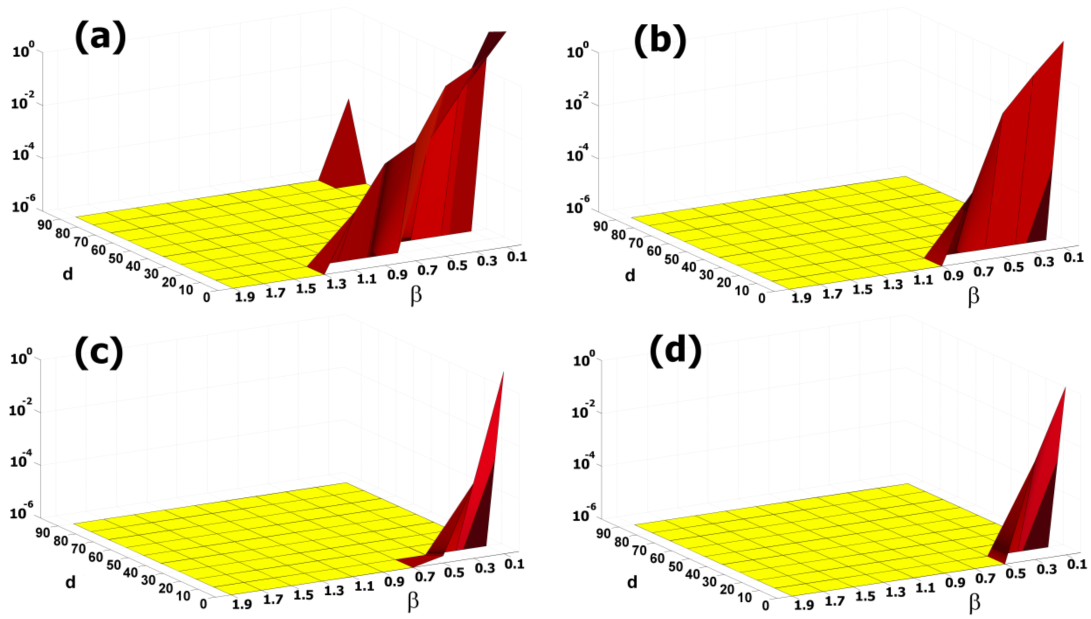

Figure 3-7: CLONALG *Cost* performance results with the *Rotated Hyper-ellipsoid* test function results for varying β and d, tested using four different values of (a) N_{pop} = 20, (b) N_{pop} = 30, (c) N_{pop} = 40, and (d) N_{pop} = 50. Yellow highlighted regions illustrate the parameter combinations which achieved the desired cost of 10^{-6} in less than 200 iterations.

This study illustrates that CLONALG efficiently achieves desired *Cost* levels on both unimodal and multimodal problems, which is a valuable advantage for electromagnetics optimization problems. After an initial study of these plots, it can be seen that the smallest population size may not be the best choice for all problems, whereas a moderate population size, *i.e.* N_{pop} = 40, produces good results with lower values for β and d. This reduces the number of clones generated at each iteration and, in turn, the computational burden from the electromagnetic solver. Based on this study, the following minimum values are chosen to be utilized in the FSS optimizations: N_{pop} = 40, d = 10, and β = 0.7. Utilizing these values, the CLONALG generates 135 clones and replaces 4 members at each iteration. For the design optimization of the multi-layered FSS structures, the CLONALG will be set to run for a maximum of 100 iterations, where some of these parameters may be increased if needed.

A parametric study of Carroll's Binary GA code [70] is also carried out using the same set of test functions as shown in Table 3-1. In this study, each dimension of the N=12 dimensional problem is discretized with a 10-bit resolution, constituting chromosomes of 120 bits in length. The parameters that we studied for this algorithm are the population size (N_{pop}), the creep mutation probability (*pcreep*), the jump mutation probability (*pmutate*), and the crossover probability (*pcross*). The recommended value in [70] is used for *pcreep*, which is calculated according to

$$pcreep = \frac{total\ number\ of\ bits}{number\ of\ parameters} \times pmutate = 10 \times pmutate. \tag{3-3}$$

In the parametric study for Carroll's Binary GA, four different population sizes of N_{pop} = [20, 30, 40, 50], several values of *pmutate* = [0.001, 0.01, 0.02, 0.03, 0.04, 0.05, 0.1, 0.2, 0.3, 0.4] and *pcross* = [0.1, 0.2, 0.3, 0.4, 0.5, 0.6, 0.7, 0.8 0.9] were tested. Values for *pcreep* are derived using (3-3) for each case of *pmutate*. For each parameter combination, 10 trials were run for a maximum of 27,800 function calls for each test function, corresponding to the total number of function calls executed by the CLONALG subject to the chosen set of parameters mentioned previously. This way both algorithms will run for the same number of function calls under the optimum parameter values. The acceptable convergence threshold for the binary GA was determined not based on the final *Cost* value but, rather, based on the shape of the binary chromosomes. If each dimension on a chromosome is either at the optimum value or only one bit away from the global optimum for that dimension, it was accepted as converged to the desired threshold value. The difference in threshold calculations is made because the CLONALG is real-valued and the GA is binary-valued. As such, the GA would need to have impractically long chromosomes in order to reach a *Cost* threshold value with a resolution of 10^{-6}. The performance of the GA for each test function is illustrated in Figure 3-8, Figure 3-9, Figure 3-10, and Figure 3-11, respectively. In each figure, there are four subplots for each population size N_{pop} = [20, 30, 40, 50]. The yellow highlighted regions in each plot illustrate the parameter combinations which achieved the desired *Cost* threshold in less than 27,800 function calls. For the *Rastrigin* function, which is a multimodal function with multiple peaks, the GA could not achieve the acceptable threshold value for any of the parameter combinations as seen in the subplots of Figure 3-10.

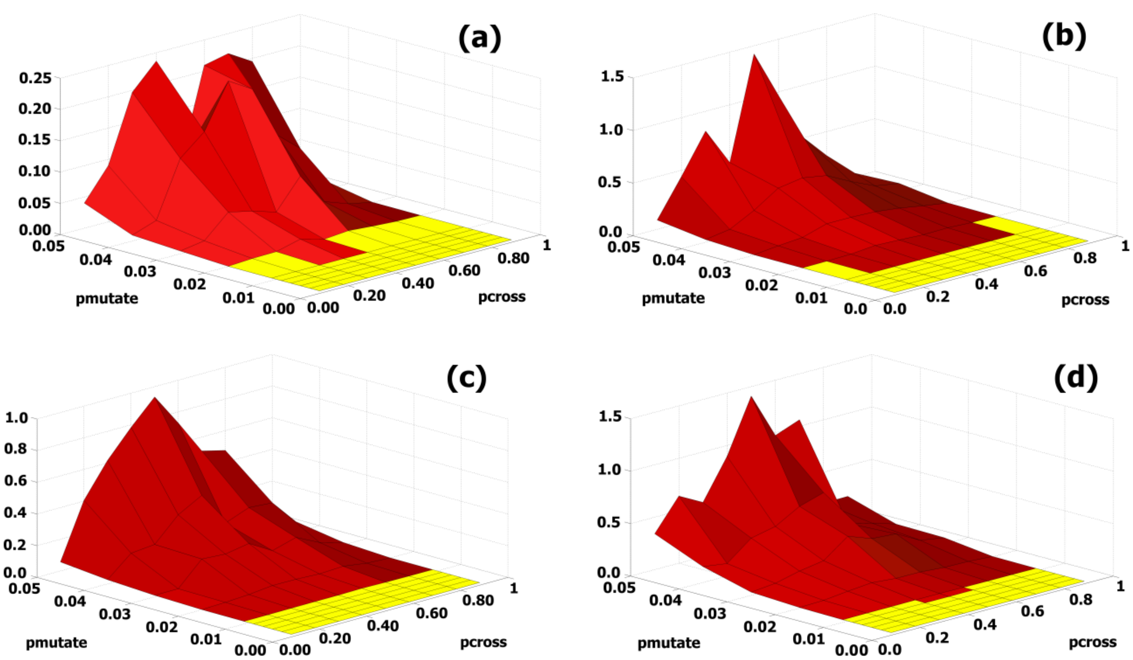

Figure 3-8: Binary GA *Cost* performance results with the *Sphere* test function for varying *pmutate* and *pcross*, tested using four different values of (a) N_{pop} = 20, (b) N_{pop} = 30, (c) N_{pop} = 40, and (d) N_{pop} = 50. The color yellow indicates the regions where the desired cost threshold is achieved in less than 27,800 function calls.

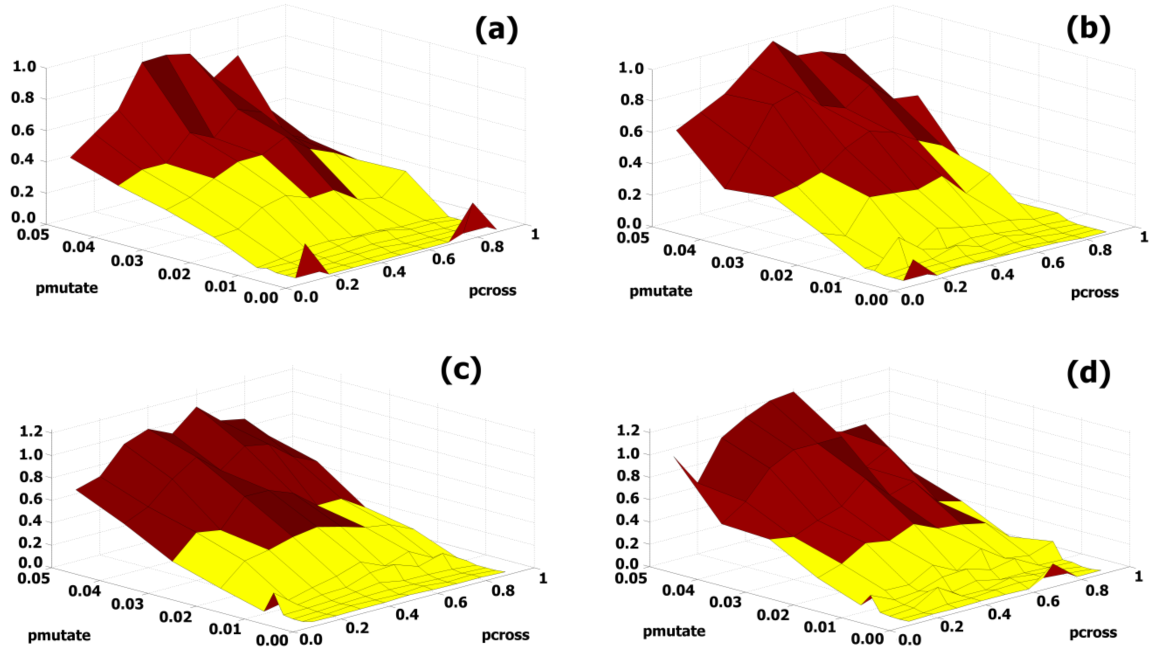

Figure 3-9: Binary GA *Cost* performance results with the *Ackley* test function for varying *pmutate* and *pcross*, tested using four different values of (a) N_{pop} = 20, (b) N_{pop} = 30, (c) N_{pop} = 40, and (d) N_{pop} = 50. The color yellow indicates the regions where the desired cost threshold is achieved in less than 27,800 function calls.

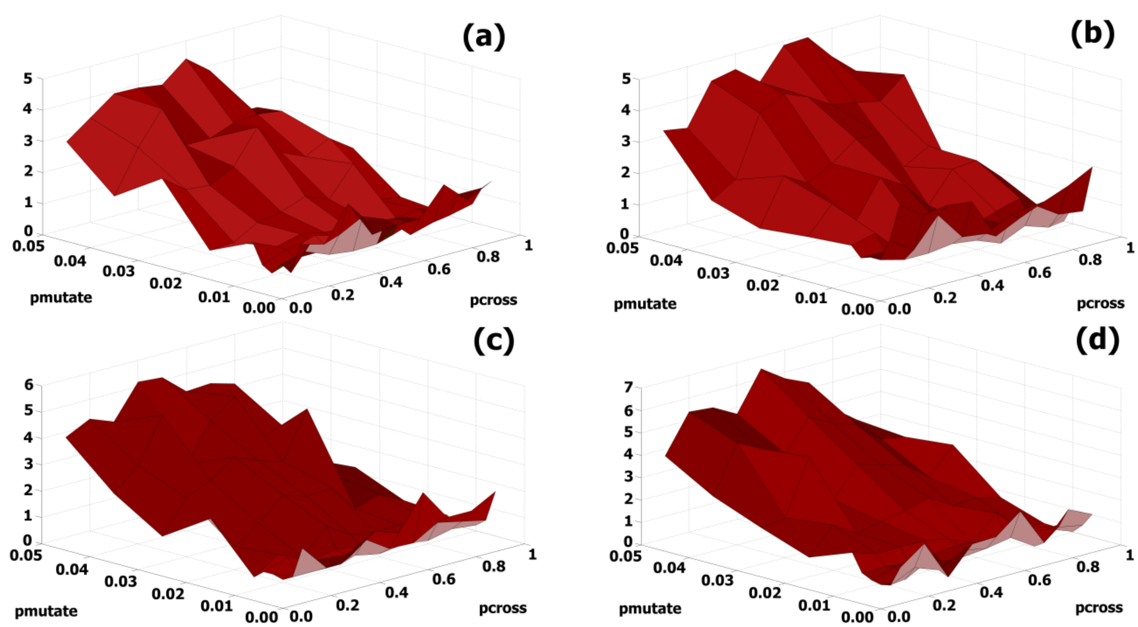

Figure 3-10: Binary GA *Cost* performance results with the *Rastrigin* test function for varying *pmutate* and *pcross*, tested using four different values of (a) N_{pop} = 20, (b) N_{pop} = 30, (c) N_{pop} = 40, and (d) N_{pop} = 50. The GA did not reach the desired cost threshold in less than 27,800 function calls. Hence, no yellow region is shown.

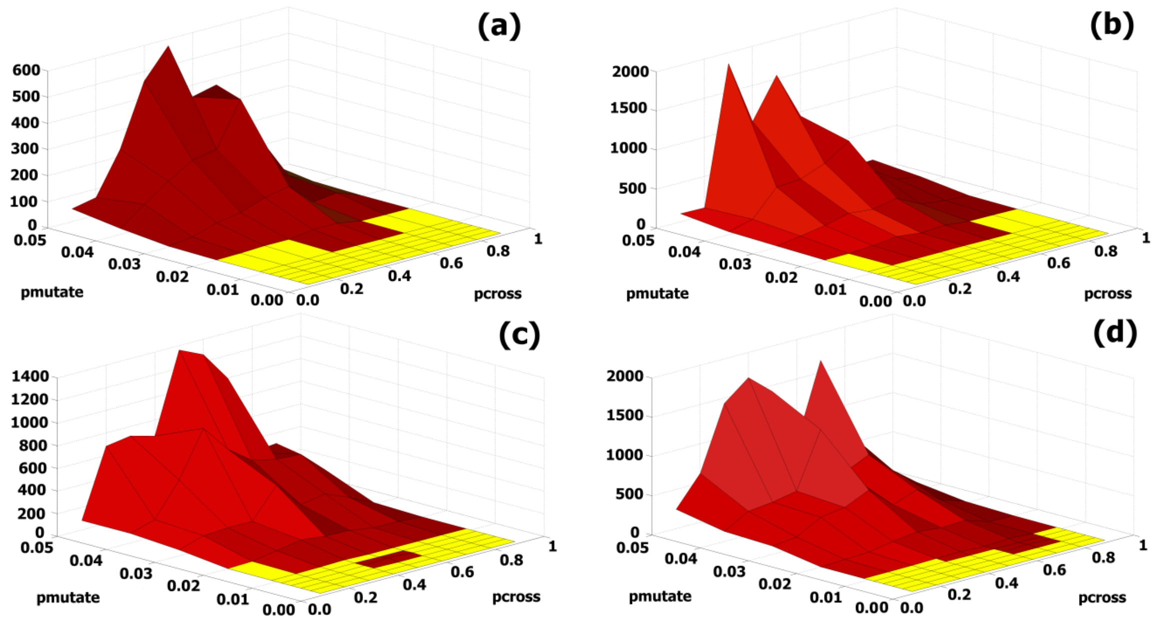

Figure 3-11: Binary GA *Cost* performance results with the *Rotated Hyper-Ellipsoid* test function for varying *pmutate* and *pcross*, tested using four different values of (a) N_{pop} = 20, (b) N_{pop} = 30, (c) N_{pop} = 40, and (d) N_{pop} = 50. The color yellow indicates the regions where the desired cost threshold is achieved in less than 27,800 function calls.

This study demonstrates that the GA works effectively for unimodal problems but is not as efficient as the CLONALG on achieving the desired performance for multimodal problems. This could be attributed to the population-wide competition between each member, whereas in CLONALG each member generates clones and competes only with its own clones. Such a schema helps to preserve diversity throughout the optimization process and makes CLONALG a very valuable optimization tool for multimodal electromagnetics optimization problems. While the GA has a disadvantage when optimizing multimodal problems, it is apparent from all test functions that the GA produces better results for smaller population sizes and smaller mutation probabilities. The crossover probability, on the other hand, does not seem to have a strong influence on the GA performance. Based on these observations, we have chosen the following parameters for the GA optimization: N_{pop} = 32, *pmutate* = 0.02, and *pcross* = 0.5, where N_{pop} is a multiple of the 8 processing cores used during the parallel optimizations. For the optimizations presented in the next section, the GA were allowed to run for 600 generations during each trial, which is usually long enough for it to converge to a solution given the complexity of the problem at hand.

3.5. Multi-layered Frequency Selective Surface Design Synthesis

The performance of both optimizers is assessed by synthesizing two-screen FSS structures for X-band operation targeting three different filter responses. The structures considered are comprised of 2-D periodic metallic screens separated by a dielectric layer. The square unit cell screen geometry is pixelized into a 17 x 17 grid and divided into eight symmetric folds, as depicted in Figure 3-12. Eight-fold symmetry provides polarization independence at normal incidence, which is desirable in many filtering applications (the symmetry can also be removed to allow for custom responses in each polarization). The nine rows of pixels in one triangular fold are encoded into the first nine dimensions of each population member. Each pixel is represented by a binary bit indicating the presence, “1”, or absence, “0”, of perfect electric conducting (PEC) metal, and all pixels from a given row are concatenated together to form a binary number, or gene in the chromosome. Fabrication rules were also implemented in the geometry generation preventing diagonal connections between metal patches because such geometries are difficult to accurately reproduce in practice. If any such diagonal connections are found in the generated geometry, one of the metal pixels is removed to eliminate the connection. The remaining three dimensions represent the unit cell size, dielectric thickness, *D*, and dielectric permittivity, ε_r, and are allowed to range from 1 cm to 2 cm, 1 mm to 5 mm, and 2 to 4, respectively. This set of optimization parameters contains a mix of both binary strings, as in the case of the unit cell geometry, and real-valued parameters. Hence, this design problem is expected to provide a fair competition between the real-coded CLONALG and the binary-coded GA optimization algorithms used in the study.

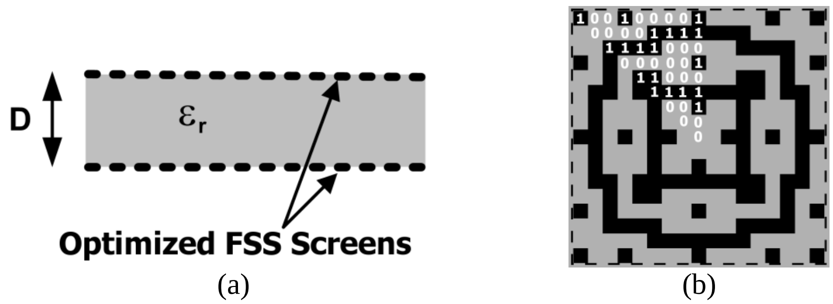

Figure 3-12: (a) Cross-section view of the two-screen FSS filters. (b) An example of an optimized metallic unit cell screen geometry for an X-band filter, where black pixels represent the metallic patches and gray pixels represent the absence of metallic patches. The chromosome values representing the screen geometry are overlaid on one triangular fold. The boundaries of the doubly periodic unit cell are illustrated with dashed lines.

The performance of each filter is evaluated by first constructing the geometry and then calculating the scattering parameters using a full-wave Periodic Finite Element Boundary Integral (PFEBI) code [76]. The PFEBI analysis tool is a hybrid technique in which the region interior to the unit cell is analyzed with the Finite Element Method (FEM) while applying periodic boundaries to the four side walls. The Method of Moments (MoM) is then employed to calculate the scattering from the device using the computed fields on the top and bottom walls of the unit cell. Brick element basis functions are employed to represent the region interior to the unit cell in order to improve the efficiency of the analysis. The advantages of the PFEBI technique include its computational efficiency and its ability to simulate inhomogeneous layers containing a mixture of lossy dielectric, metallic, or impedance surfaces. The PFEBI code is directly linked to the CLONALG and GA executables in order to improve the performance of the *Cost* evaluation.

Reflection and transmission values are computed by PFEBI at multiple frequency points and used to calculate the *Cost* for each candidate design according to

$$Cost = \sum_{stopfreqs} \left(0 - |T|\right)^2 + \sum_{passfreqs} \left(1 - |T|\right)^2 \ , \tag{3-4}$$

where *stopfreqs* and *passfreqs* are the desired stop and pass band frequencies, and T is the transmission coefficient. Thus, an ideal filter would have 100% transmission at every pass band point and no transmission at every stop band point. However, we will set a minimum performance requirement of 10 dB attenuation in transmission for stop bands and reflection for pass bands when we evaluate the final, optimized designs.

For the first design example, a pass band filter is optimized with the desired pass band from 9.5 GHz to 10.5 GHz, represented by 5 frequencies, and stop bands from 8 GHz to 9 GHz and from 11 GHz to 12 GHz, represented by a total of 6 frequencies. The stop-band frequencies are *stopfreqs* = [8.0, 8.5, 9.0, 11.0, 11.5, 12.0] GHz, and the pass-band frequencies are *passfreqs* = [9.5, 9.75, 10.0, 10.25, 10.5] GHz. Scattering parameters at each of the eleven frequency points are computed for every candidate design via PFEBI in order to compute the *Cost* for each population member. After a minimum of five runs were carried out by both the CLONALG and the GA, the best FSS designs for each algorithm were selected and are shown in Figure 3-13. In the CLONALG optimization the utilized parameter values were N_{pop} = 40, d = 30, and β = 0.7, where the optimized design shown in Figure 3-13 (a) has a unit cell size of 1.5764 cm, a thickness of 0.4525 cm, and a substrate permittivity of 3.76. The screen geometry for the GA optimized design in Figure 3-13 (b) is very different in appearance from that found by the CLONALG, illustrating that the design flexibility afforded by the pixelized FSS geometry can result in many local minima in the parameter space. The unit cell size for GA synthesized design is 1.1922 cm, the thickness is 0.3164 cm, and the relative permittivity is 2.84. The magnitudes of the transmission and reflection spectra for both FSS filter designs are plotted in Figure 3-14 with gray regions highlighting the specified pass band and stop bands. Both designs meet the desired optimization goals, where the reflection in the pass band is less than -10 dB and transmission in the stop bands is less than -10 dB.

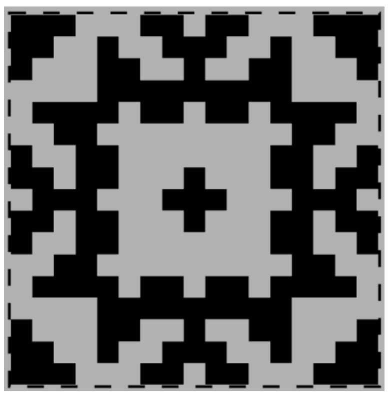

(a)

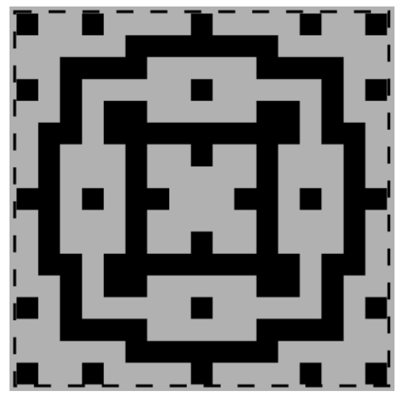

(b)

Figure 3-13: Optimized PEC unit cell screen geometries for the first X-band filter design are shown. (a) CLONALG and (b) GA optimized designs are depicted with unit cell dimensions of 1.5764 cm and 1.19216 cm, respectively. Black shaded pixels represent the PEC pixels and gray shaded pixels represent the absence of the PEC where the dielectric is exposed.

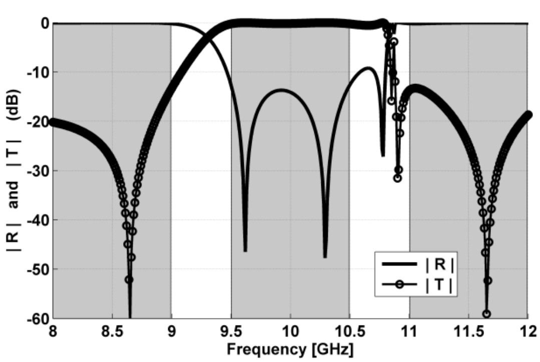

(a)

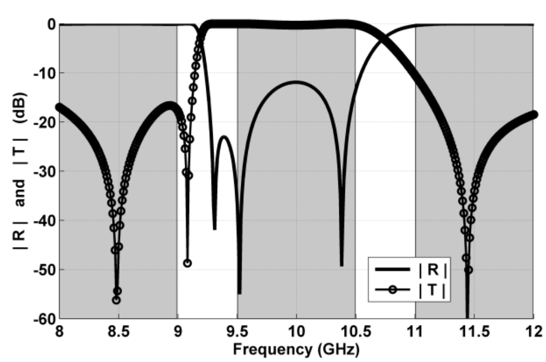

(b)

Figure 3-14: Reflection and transmission spectra for the (a) CLONALG and (b) GA synthesized designs shown in Figure 3-13. Both designs exhibit a strong pass band from 9.5 GHz to 10.5 GHz and strong stop bands below 9 GHz and above 11 GHz in the X-band frequency range. The frequency regions of interest for optimization are highlighted in grey.

For the second design example, a tri-band filter is optimized, with narrow pass bands at 9.0 GHz, 10.0 GHz, and 11.0 GHz and with stop bands specified elsewhere over the entire X-band from 8 GHz to 12 GHz. The specified pass band frequency points are *passfreqs* = [9.0, 10.0, 11.0] GHz, and the stop band frequencies are *stopfreqs* = [8.0, 8.5, 9.5, 10.5, 11.5, 12.0] GHz, for a total of nine frequency points evaluated by the PFEBI for each population member. Both the GA and CLONALG were run for a minimum of five trials in order to obtain the best FSS designs, which are illustrated in Figure 3-15. In the CLONALG optimization the utilized parameter values were N_{pop} = 50, d = 20, and β = 0.8, and the optimized design depicted in Figure 3-15 (a) has a unit cell dimension of 1.6754 cm, a thickness of 0.4086 cm, and a substrate permittivity of 3.52. The GA optimized design shown in Figure 3-15 (b) has a unit cell dimension of 1.9960 cm, a thickness of 0.2866 cm, and a substrate permittivity of 3.40. Once again, both screen geometries appear very different, indicating the flexibility of the platform and highlighting the usefulness of both optimizers to isolate designs that meet custom performance criteria.

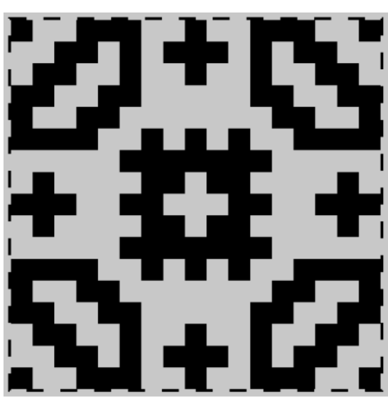

(a)

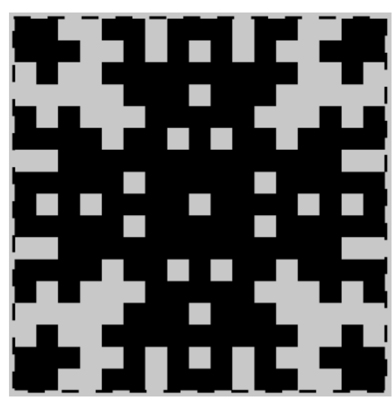

(b)

Figure 3-15: Optimized PEC unit cell screen geometries for the second X-band filter design are shown. (a) CLONALG and (b) GA optimized designs are depicted with unit cell dimensions of 1.67565 cm, and 1.99608 cm, respectively. Black shaded pixels represent the PEC pixels and gray shaded pixels represent the absence of the PEC where the dielectric is exposed.

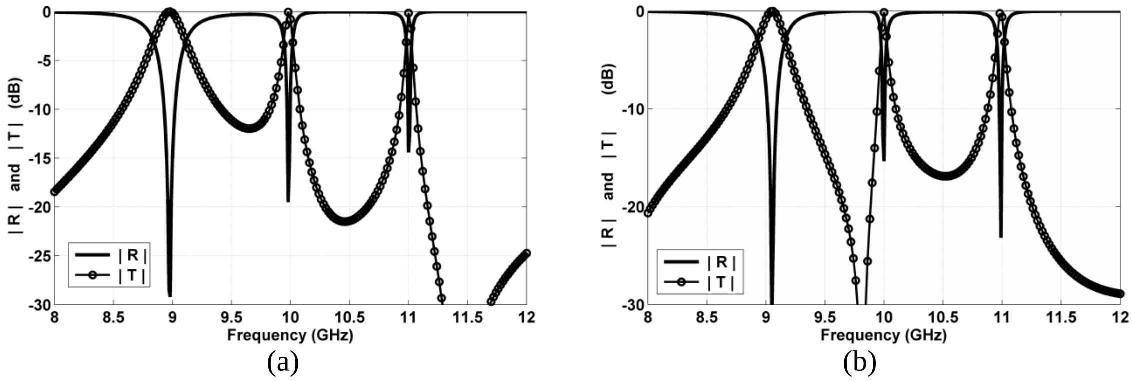

Figure 3-16: Reflection and transmission spectra for the (a) CLONALG and (b) GA synthesized designs shown in Figure 3-15. Both designs exhibit three strong, narrow pass bands at 9 GHz, 10, GHz, and 11 GHz and strong stop bands elsewhere over the X-band frequency range

The transmission and reflection responses for both designs are plotted in Figure 3-16, demonstrating strong, narrow pass bands at 9 GHz, 10 GHz, and 11 GHz as well as stop bands at the specified frequencies elsewhere across the X-band. While this example only seeks to demonstrate tri-band performance, the shape and bandwidth of each pass band could be tailored to be more uniform by specifying more pass and stop band frequency points in the *Cost* function.

For the third design example, a low-pass filter is optimized with a broad pass band spanning from the lower edge of the X-band to 9.75 GHz and a broad stop band from 10.0 GHz to the upper edge of the X-band. The pass band frequencies for this design are *passfreqs* = [8.0, 8.5, 9.0, 9.5, 9.75] GHz, while the stop band frequencies are *stopfreqs* = [10.0, 10.25, 10.5, 11.0, 11.5, 12.0] GHz, for a total of eleven frequency points to be evaluated by the PFEBI code for each population member. A minimum of five runs were carried out by both the CLONALG and GA, resulting in the best designs shown in Figure 3-17. In the CLONALG optimization the utilized parameter values were N_{pop} = 50, d = 30, and β = 0.8, where the synthesized design shown in Figure 3-17 (a) has a unit cell dimension of 1.1865 cm, a thickness of 0.4984 cm, and a permittivity of 3.91. On the other hand, the GA synthesized design is shown in Figure 3-17 (b) and has a unit cell dimension of 1.3647 cm, a thickness of 0.4686 cm, and a substrate permittivity of 2.44. The scattering responses from both of these designs plotted in Figure 3-18 exhibit excellent low-pass filter performance, with the reflection suppressed under -10 dB for frequencies below 9.75 GHz and the transmission magnitude below -10 dB for frequencies above 10 GHz.

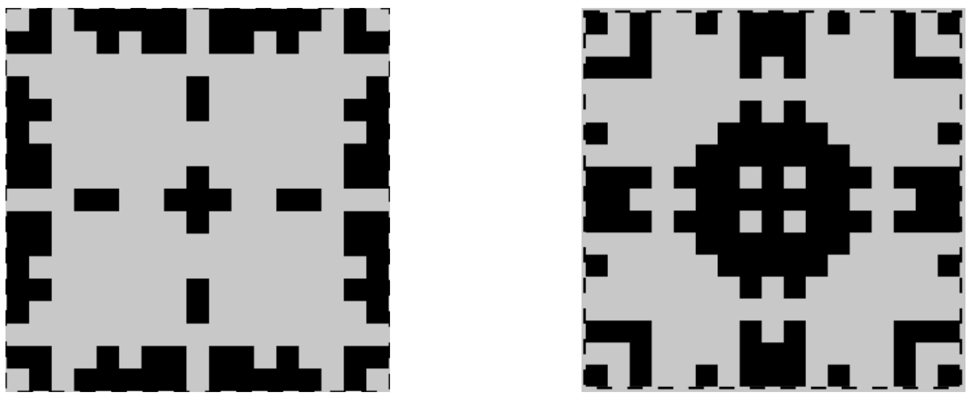

(a) (b)

Figure 3-17: Optimized PEC unit cell screen geometries for the third X-band filter design are shown. (a) CLONALG and (b) GA optimized designs are depicted with unit cell dimensions of 1.1865 cm, and 1.3647 cm, respectively. Black shaded pixels represent the PEC pixels and gray shaded pixels represent the absence of the PEC where the dielectric is exposed.

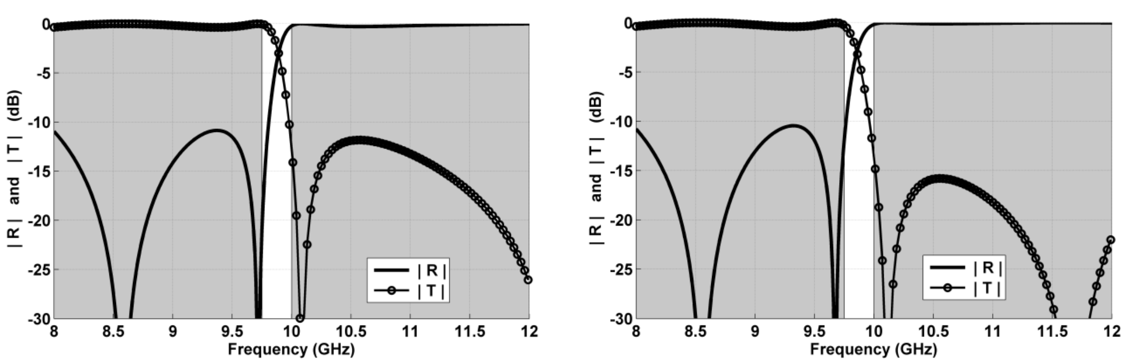

(a) (b)

Figure 3-18: Reflection and transmission spectra for the (a) CLONALG and (b) GA synthesized designs shown in Figure 3-17. Both designs exhibit low-pass filter responses with strong transmission below 9.5 GHz and strong reflection above 10 GHz within the X-band frequency range of 8 GHz to 12 GHz. The frequency regions of interest for optimization are highlighted in grey.

The *Cost* per number of evaluations for each of the three design examples is plotted in Figure 3-19 in order to compare the performance of the CLONALG and GA techniques over the course of the optimizations. For the first and second filter design problems, CLONALG provides a faster convergence than the GA and a better final *Cost* value. For the third filter design problem, the performance of both algorithms is very comparable. These results clearly indicate that CLONALG performs remarkably well on multi-modal problems and offers an excellent alternative to the traditionally used GA for complex electromagnetic design optimization problems.

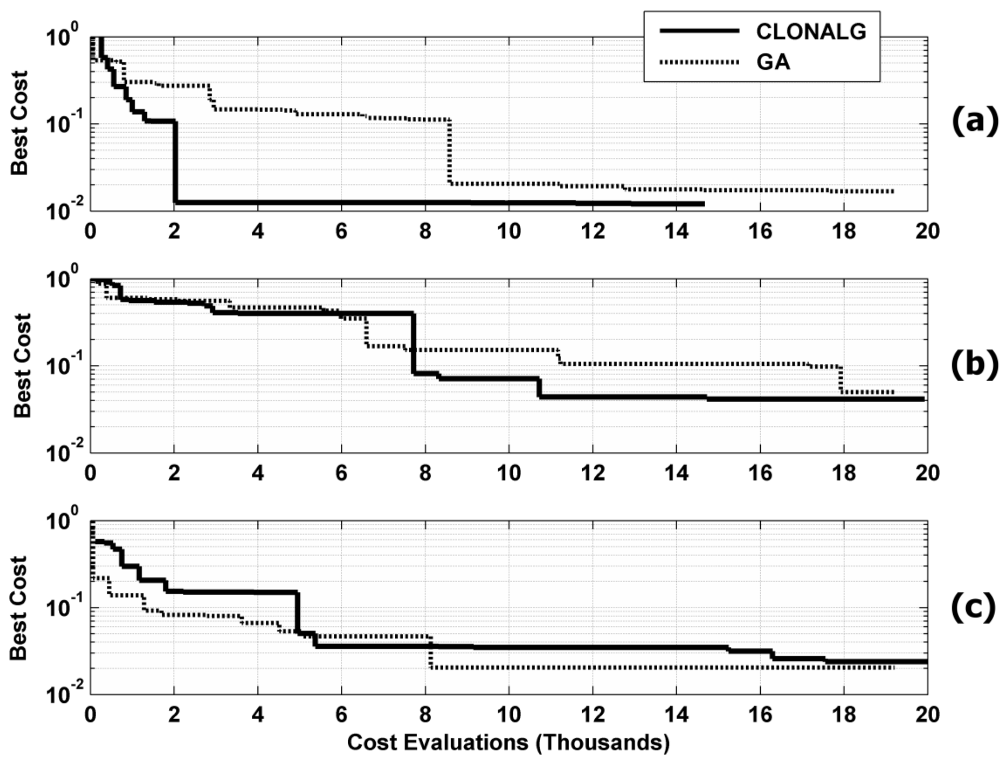

Figure 3-19: Performance comparison between the parallel CLONALG and parallel GA techniques. Best *Cost* vs. the number of cost evaluations is plotted for the three FSS filter design examples. (a) The first and (b) the second FSS design examples show that the CLONALG demonstrated faster convergence and better final design performance compared with the GA, and the (c) third FSS design example shows similar performance between the CLONALG and GA.

3.6. Summary

The goal of this chapter was to demonstrate an efficient, parallel implementation of the Clonal Selection Algorithm, its ease of implementation, and its effectiveness in tackling optimization problems in electromagnetics. Through the analysis of various test functions and the optimization of three different multi-layered FSS filters for operation at the X-band, the real-valued CLONALG has shown itself to be very efficient both in unimodal and in multimodal optimization problems, whereas the binary GA implementation may struggle with multimodal problems due to its higher competitive nature among all members. By carefully choosing a small number of parameters, it was demonstrated that the CLONALG could be easily tuned to efficiently optimize a challenging practical electromagnetic design problem. The parallel implementation utilizing the Message Passing Interface (MPI) provided an effective way to overcome the computational burden of evaluating a large clone population by distributing the work load to multiple processors. It was also shown through the multi-layered FSS filter design examples that when comparing the *Cost* per number of evaluations, the parallel CLONALG can compete on equal footing or even outperform a parallel binary GA.

Chapter 4

Wind Driven Optimization (WDO)

This chapter introduces a novel numerical nature-inspired optimization algorithm called the Wind Driven Optimization (WDO), discusses the theory behind the WDO, provides the terminology for later use, and illustrates its efficiency and versatility by applying WDO to solve various electromagnetic optimization problems.

4.1. Theory and Terminology

Nature can be considered as a big system with a vast number of sub-systems, all of which have been existing for millions of years. Such accumulation of knowledge and ability to perfect it over time makes the nature as one of the biggest source of information and an unmatched inspiration to scientists and engineers alike. Since early 1970s, starting with the Genetic Algorithms (GA) [5], there has been various nature-inspired optimization algorithms proposed and some of which have been proven to be very efficient global optimization strategies. Along with the GA, the Particle Swarm Optimization (PSO) [77], Ant Colony Optimization (ACO) [78], Differential Evolution (DE) [79], Clonal Selection Algorithm (CLONALG) [55], Covariance Matrix Adaptation Evolutionary Strategy (CMA-ES) [80] and many more have been proposed, and implemented successfully. Unfortunately, there is no single method that stands out as the best among the family of the nature-inspired optimization algorithms where each algorithm comes with their strengths and weaknesses.

In the search for new methods, a novel nature-inspired optimization algorithm called the Wind Driven Optimization (WDO) technique is introduced in this chapter. In essence, the WDO is a population based iterative heuristic global numerical optimization technique for multi-dimensional and multi-modal problems with the ability to implement constraints on the search domain.

The inspiration comes from the Earth's atmosphere, where the wind blows in an attempt to equalize horizontal imbalances in air pressure [81]. The term "wind" actually refers to the large-scale horizontal air motion particularly in the lowest layer of the Earth's atmosphere called the troposphere. The troposphere is the lowest layer which extends from the surface of the earth's crust up to 18 km, where the layer thickness may vary based on the location's latitude [82]. The troposphere layer contains up to 75% of the atmosphere's mass and most of the weather activities, such as the wind, occur within. The amount of radiation reaching from the sun causes heating both on the surface of the earth and in the atmosphere itself. However, the amount of heating varies depending on various factors such as the location on earth, whether the area is a body of water or soil and also varies with the amount of cloud coverage in the region. In addition, the spherical shape of the earth allows illumination of only half of the surface at a time and its daily rotation causes amount of energy falling on a single location to vary every day. Due to differences in the solar energy reaching to the different locations on earth surface, the temperature can vary significantly among regions. Areas with higher temperature would have rising warm air and regions with lower temperatures would have sinking cold air causing the air density to decrease in high temperature areas and to increase in low temperature areas. Due to earth's gravitational field, $\boldsymbol{g}$, the mass of atmosphere applies a force on the earth's crust, where the air pressure can simply be defined by the force exerted per unit area [83]. Since temperature differences lead to variations in air pressure at different locations, horizontal differences in air pressure causes the air to move from high pressure regions to low pressure regions [84]. This movement is due to the pressure gradient, ∇P, which can be calculated as the pressure change over a distance as expressed in (4-1) in rectangular coordinate system [85].

$$\nabla P = \left(\frac{\partial P}{\partial x}, \frac{\partial P}{\partial y}, \frac{\partial P}{\partial z} \right). \tag{4-1}$$

More specifically, wind blows in the direction from a high pressure zone to low pressure zone at a velocity proportional to the pressure gradient force [81], [86]. Considering the fact that the air has a finite mass and a finite volume (δV), then the pressure gradient force ($\boldsymbol{F}_{PG}$) can be expressed as

$$\vec{F}_{PG} = -\nabla P \ \delta V \tag{4-2}$$

There are two distinct descriptions of atmospheric behavior, which are Lagrangian and Euler descriptions [87]. In the Euler description, the air is treated as a fluid system and a continuum which is described by the fluid motion governed by the equations of continuum mechanics [87], [88]. On the other hand, the Lagrangian description represents the atmosphere as the collection of many infinitesimal fluid parcels [88], [89]. In the derivation of the equations for WDO, the Lagrangian description is preferred due to fact that it would simplify the numerical algorithm and reduce computational overhead that the WDO would need during the optimization of a real world problem. Another simplification is critical for the air parcel description, which is assumed to be cuboid in rectangular coordinate system in Lagrangian description. In WDO abstraction though, an air parcel has to be dimensionless otherwise the different corners of it would represent different coordinates, which would complicate the WDO implementation. In addition, the different faces of cuboids could experience different pressure values, which may cause the deformation of the cuboid, sheering, twisting or stretching would have to be taken into account, which render the WDO implementation as computationally demanding and impractical. Thus, in the implementation of the WDO, the air parcels are assumed to be dimensionless, and weightless, which simplifies the equations yet preserves the accuracy of the physical interpretation.

In the abstraction of the wind, it is also assumed that the atmosphere is an homogenous ideal gas in hydrostatic balance. Utilizing the fact the equations derived in atmospheric dynamic are in rectangular coordinate system and considering the fact that the horizontal movement of air is stronger compared to its vertical movement, the wind can be treated as a horizontal motion only due to the horizontal pressure variation [81]. In the WDO though, the algorithm would work on a *N*-dimensional search space hence the three dimensional atmospheric dynamics equations have to be mapped to multi-dimensional problems, which only can be possible through certain assumptions and simplifications.

The starting point for computation of the trajectory of an air parcel is the Newton's second law of motion, which provides accurate results when applied to the analysis of atmospheric motion in the Lagrangian description [83], [84], [88]. It states that the total force applied on an air parcel causes the air parcel to accelerate, $\boldsymbol{a}$, in the same direction as the applied total force,

$$\rho\,\vec{a} = \sum \vec{F}_i\,, \tag{4-3}$$

where ρ is the air density for an infinitesimally small air parcel, and $\boldsymbol{F_i}$ are the forces acting on it. To relate the air pressure to the air parcel's density and temperature the ideal gas law can be utilized,

$$P = \rho\,R\,T, \tag{4-4}$$

where P is the pressure, R is the universal gas constant and T is the temperature.

The pressure gradient force can be considered as the fundamental force to start the air motion, but there are other forces that also effect the trajectory and speed of the movement. In

(4-3), there can be four major forces included, that either cause the wind to move in a certain direction at a certain velocity or deflect it from its existing path. The most observable force causing the air to move is the pressure gradient force ($\boldsymbol{F}_{PG}$), which is already defined in (3-1). Another force is the friction force ($\boldsymbol{F}_F$), and it would simply act to oppose such motion started by the pressure gradient force. The exact description of the friction force in the atmosphere is very complex and hence a simplified form can be utilized as follows,

$$\vec{F}_F = -\rho \alpha \vec{u} \ , \tag{4-5}$$

where α is the friction coefficient and $\boldsymbol{u}$ is the velocity vector of the wind.

In our physical three-dimensional atmosphere, the gravitational force ($\boldsymbol{F}_G$) is treated as a vertical force. However, if the center of the earth is considered as the center of the rectangular coordinate system, then it can be claimed that the gravitational force pulls towards the origin of the coordinate system on any dimension, then it can be easily mapped to N-dimensional space. For this reason, the gravitational force is included in the algorithm as a force on all N-dimensions directed towards the center of the coordinate system. In its simplest form, the gravitational force ($\boldsymbol{F}_G$) can be defined as [89],

$$\vec{F}_G = \rho \ \delta V \ \vec{g} \ . \tag{4-6}$$

The rotation of earth causes the reference frame to rotate leading to the coriolis force ($\boldsymbol{F}_C$), named after French scientist Gaspard Coriolis, which in turn causes the deflection of the wind from its exiting path in our atmosphere [84]. While the amount of deflection depends on the direction of the rotation of the earth, the latitude (which hemisphere) and the air parcel's speed in our atmosphere, in WDO, it is implemented as a motion in one dimension that affects the velocity in another dimension. For example, if a two dimensional motion is considered in XY plane, then the velocity vector has two major components; one in the x-direction and the other is in the y-direction. In WDO, the coriolis force implemented such a way that the speed in the x-direction is influenced by the speed in the y-direction. In *N*-dimensional space, this is randomized so that different direction could influence other direction over the duration of optimization process. The coriolis force is defined by

$$\vec{F}_C = -2\Omega \times \vec{u} \,, \tag{4-7}$$

where, $\mathbf{\Omega}$ represents the rotation of the earth, and ***u*** is the velocity vector of the wind.

While these four forces are the major contributors to the motion of the wind, there are other forces that are not included in the implementation of the WDO. For example, advection, which is defined in the Eulerian description, along with the centrifugal force are ignored in the *N*-dimensional WDO implementation where as the turbulent drag force is assumed as a part of the friction force [88]. It is crucial to understand that the WDO implementation is not an attempt to duplicate the atmospheric motion, yet is it is an attempt to use the inspiration provided by the nature in the abstraction and invention of an efficient numerical optimization algorithm that is fundamentally based on the physical equations of the large-scale atmospheric motion.

The forces described above can be summed and plugged in the right-hand side of the Newton's second law of motion as in (4-3), which combines in to,

$$\rho \;\Delta\vec{u}/\Delta t \;= (\rho\,\delta V\;\vec{g}) + (-\nabla P\;\delta V) + (-\rho\alpha\vec{u}) + (-2\Omega\times\vec{u}) \tag{4-8}$$

where the acceleration term in (4-3) is rewritten as $\vec{a} = \Delta\vec{u} / \Delta t$ above, and $\Delta t = 1$ is assumed for simplicity. For an infinitesimally small, dimensionless air parcel, the term δV assumed no contribution hence dropped from (4-8), which simplifies to,

$$\rho\Delta\vec{u} = (\rho\vec{g}) + (-\nabla P) + (-\rho\alpha\vec{u}) + (-2\Omega\times\vec{u}). \tag{4-9}$$

Utilizing the ideal gas law from (4-4), the density (ρ) can be written in terms of the pressure, the temperature and the universal gas constant and inserted in (4-9) as,

$$\frac{P_{cur}}{RT}\Delta\vec{u} = (\frac{P_{cur}}{RT}\,\vec{g}) + (-\nabla P) + (-\frac{P_{cur}}{RT}\,\alpha\vec{u}) + (-2\Omega\times\vec{u}), \qquad (4\text{-}10)$$

where P_{cur} represents the pressure value for an individual parcel at its current location. Dividing both sides of (4-10) by P_{cur} / RT gives

$$\Delta\vec{u} = (\vec{g}) + (-\nabla P\frac{RT}{P_{cur}}) + (-\alpha\vec{u}) + (\frac{-2\Omega\times\vec{u}\,RT}{P_{cur}}). \qquad (4\text{-}11)$$

At this point, it is should be obvious that the change in velocity and position can be computed from the Newton's second law of motion and it is assumed in the WDO that each air parcel's velocity and position varies at each iteration as their exploration of the search space continues. Thus, the change in velocity, $\Delta\vec{u}$, can be written as $\Delta\vec{u} = \vec{u}_{new} - \vec{u}_{cur}$, where $\vec{u}_{cur}$ is the velocity at the current iteration and $\vec{u}_{new}$ is the velocity in the next iteration. The friction force in (4-5) is computed using the current velocity value as well, thus (4-12) can be rewritten as

$$\vec{u}_{new} = (1-\alpha)\vec{u}_{cur} + (\vec{g}) + (-\nabla P\frac{RT}{P_{cur}}) + (\frac{-2\Omega\times\vec{u}\,RT}{P_{cur}}). \qquad (4\text{-}12)$$

In (4-12), there are two terms that are not written in terms of velocity or position vectors and these terms are **g** and $-\nabla P$. Since the gravitational force is considered as the force pulling an air parcel from its current location towards the center of the coordinate systems, it can be illustrated on a single dimension as seen in Figure 4-1(a), where the vector, **g**, can be broken down in direction and magnitude as **g** = |g| (0 - x_{cur}). This tells us the magnitude and the direction of the gravitational field that can be plugged in (4-12).

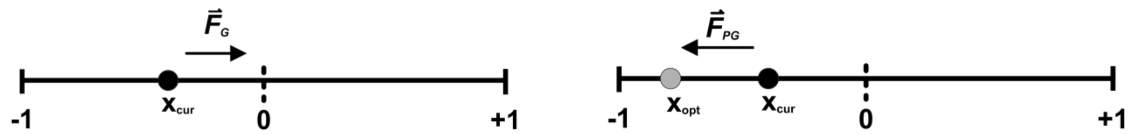

(a) (b)

Figure 4-1: (a) Illustration of the gravitational force (F_G) in one dimensional search space where the dimension spans in the range of [-1, 1] and the center of the coordinate system is defined at zero. (b) Illustration of the pressure gradient force (F_{PG}) in one dimensional space, where x_{cur} represents the location of an air parcel at the current iteration and the x_{opt} represents the optimum pressure location found throughout the optimization.

The other term is the pressure gradient, $-\nabla P$, which is defined as the force moving an air parcel from its current location to an optimum pressure point, as seen in Figure 4-1(b). Similar to the gravitational field, the pressure gradient can be broken down in to magnitude and direction terms and can be written as $-\nabla P = \left|P_{opt} - P_{cur}\right|(x_{opt} - x_{cur})$. This tells us the magnitude of the pressure gradient is simply the pressure difference between the current location of an air parcel and the optimum pressure found so far and directed from the current location to the optimum location.

Updating the (4-12) with the new equations for the gravitational field and pressure gradient, equation (4-12) can be rewritten as

$$\vec{u}_{new} = (1-\alpha)\vec{u}_{cur} - g\,x_{cur} + \left(\frac{RT}{P_{cur}}\left|P_{opt} - P_{cur}\right|\left(x_{opt} - x_{cur}\right)\right) + \left(\frac{-2\Omega\times\vec{u}\,RT}{P_{cur}}\right). \tag{4-13}$$

Lastly, there are two additional substitutions needed, where the coriolis force was represented by the cross product of the earth's rotation vector and the velocity vector of air parcel by the term ($\Omega\times\vec{u}$) in (4-13). As described previously, the influence of the coriolis force is replaced by the velocity influence from another dimension, $\vec{u}_{cur}^{\,other\dim}$, and all coefficients can be combined into a single term, *i.e.* $c = -2RT$, which simplifies the coriolios force contribution in (4-13) and can be rewritten as

$$\vec{u}_{new} = (1-\alpha)\vec{u}_{cur} - g\,x_{cur} + \left(RT\,\frac{\left|P_{opt} - P_{cur}\right|}{P_{cur}}\left(x_{opt} - x_{cur}\right)\right) + \left(\frac{c\,\vec{u}_{cur}^{\,other\dim}}{P_{cur}}\right). \tag{4-14}$$

A potential pitfall in the above form of the velocity update equation is that the pressure values are explicitly used. In cases where the pressure value is extremely large, the updated velocities could become impractically large and the performance of the WDO would diminish. Instead of using the actual pressure values, one can use a ranking-based approach, where the population of air parcels are ranked in descending order based on their pressure values and the (4-14) can be rewritten as,

$$\vec{u}_{new} = (1-\alpha)\,\vec{u}_{cur} - g\,x_{cur} + \left(RT\left|1-\frac{1}{i}\right|\left(x_{opt} - x_{cur}\right)\right) + \left(\frac{c\,\vec{u}_{cur}^{\,other\dim}}{i}\right). \tag{4-15}$$

where *i* represents the ranking among all air parcels. The first term in (4-15) states that if there is no other forces acting on the air parcel, then it would continue its current path with velocity proportionally reduced by the friction. The second term states that gravity would pull the air parcel from its current location towards the center of the coordinate system at a magnitude proportional with the constant g. The third term in the equation states that the highest ranked air parcels will most likely be at locations closer to the x_{opt}, hence the effect of the pressure gradient would be smaller. The last term states that the movement on other dimensions can affect other dimensions which may have larger effect for the higher ranked air parcels.

As it can be clearly seen in (4-15), there are multiple coefficients that have to be assigned a value prior to the start of the optimization, and these coefficients are; α, g, RT, and c. A numerical study is carried out in the following section to establish the optimum values for these parameters.

At each iteration, the velocity and then the position of the air parcels have to be updated and the velocity update equation is established in (4-15). The position can be updated simply by utilizing the following equation,

$$\vec{x}_{new} = \vec{x}_{old} + (\vec{u}_{new} \times \Delta t) \tag{4-16}$$

where $\boldsymbol{u_{new}}$ is the updated velocity for the next iteration as established in (4-15), $\boldsymbol{x_{old}}$ is the current position of the air parcel in the search space, and $\boldsymbol{x_{new}}$ is the new position for the next iteration. For simplicity, $\Delta t = 1$ is assumed.

A population of air parcels would start at random positions in the search space and utilizing (4-15) and (4-16), their velocity and position would be adjusted at each iteration and they would move towards an optimum pressure location at the end of the last iteration. Considering that actually the optimum pressure point on the *N*-dimensional search space corresponds to the optimum solution for the optimization problems, WDO offers a simple but efficient way to tackle them.

For each dimension, WDO allows the air parcels to travel only in the bounds of [-1, 1] and if an air parcel tries to travel outside of these bounds at any dimension, the its position at that particular dimensions is set to the boundary value. For example, if the air parcel tries to go from 0.82 to beyond 1 at the x-dimension, the position for the next iteration is forced to be 1 on the x-dimension. In literature, there has been many other boundary conditions proposed [90], yet for the WDO, the gravitational pull would pull any air parcels that are stuck at the boundaries back in to the feasible search space.

It also should be pointed out that the updated velocity of the air parcels should be limited to a maximum value per iteration. The main reason for this is to simply prevent air parcels from taking large steps and overlook certain regions in the search space. To limit the magnitude of the velocity following simple rule is implemented,

$$\vec{u}_{new}^{*} = u_{\max} \frac{\vec{u}_{new}}{|\vec{u}_{new}|} \tag{4-17}$$

where the direction of the motion is preserved but the magnitude is limited to be no more than u_{max} at any dimension and $\vec{u}_{new}^{*}$ represents the velocity after limited to maximum speed.

So far the theory behind the WDO, the operators of the algorithm and implemented constraints are discussed. For clarity, the terminology of the WDO is summarized in Table 4-1.

Table 4-1 : The terminology of the Wind Driven Optimization algorithm.

Terminology	**Description**
Air parcel	An individual member, whose coordinate values represents a candidate solution to the optimization problem at hand.
Population	A group of predetermined number of diverse air parcels.
Generation	One iteration, where the WDO operators are applied.
Position	The coordinates of an air parcel, which corresponds to a solution to the optimization problem.
Velocity	The amount of position displacement per iteration.
Pressure	An assigned number to air parcels based on their proximity to the global solution, which establishes how well an air parcel meets the desired design performance. Analogy can be made with fitness, cost, penalty functions.
Ranking	Sorting of the air parcels at each iteration based on their pressure values.

One can observe various similarities between WDO and other nature-inspired optimization algorithms. All are population based iterative methods aiming to improve the best candidate solution over time. There can also analogies be made such as the pressure function and the fitness function, or the cost function, which could also be called the penalty function. The purpose is to evaluate the goodness of the candidate solution. In terms of having the position and velocity update rules, WDO could be compared against the Particle Swarm Optimization (PSO), where PSO is based on a swarm of particles those share information about the search space to achieve better results.

For the implementation of the WDO, a pseudo code is provided in Table 4-2 along with a flowchart as illustrated in Figure 4-2 , and a sample Matlab / Octave code is provided in Appendix A.

Table 4-2: Pseudo Code for the WDO Implementation

1. Define dimension limits, population size, maximum number of iterations, coefficients, and all other parameters.
2. Initialize the position and velocity of all air parcels, where the initial population is randomly distributed over the *N*-Dimensional search space.
3. Evaluate the pressure of the whole population at their current positions and rank them.
4. Update velocity and check velocity limits.
5. Update position and check position boundaries.
6. Continue from step 3 until the maximum number of iterations are exhausted.

As seen both in the pseudo code and in the Figure 4-2, the algorithm starts with the initialization stage where all parameters related to the WDO as well as the other parameters related to the optimization problem have to be defined. Also, one has to define a pressure function (fitness function) and define parameter boundaries. Once the optimization problem is set up, then the population of air parcels are randomly distributed over the *N*-Dimensional search space with a random velocity assigned to them. Next step is to evaluate the pressure (fitness) values of each air parcel at their current positions. Once, the pressure values are evaluated, the population is ranked based on their pressure and velocity update is applied as given in (4-15) along with the restrictions as given in (4-17). The positions for the next iteration are updated by utilizing (4-16) and the boundaries are checked to prevent any air parcel from running out of feasible search space. One all the updates are carried out, the pressure at new locations is to be evaluated once again and this iterative procedure continues until the maximum number of iterations are reached. Finally, the best pressure location at the end of the last iteration is the optimization result and the best candidate solution to the problem.

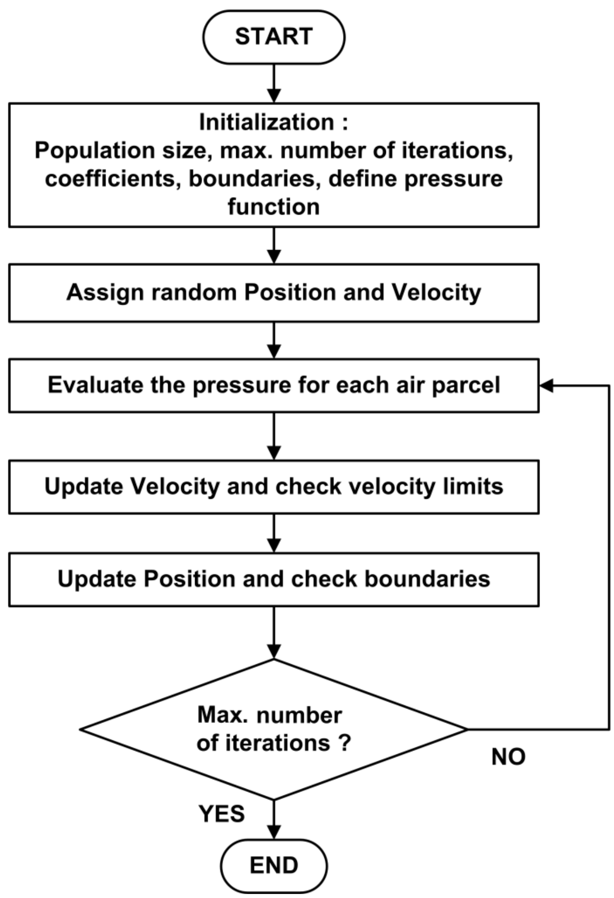

Figure 4-2: Flowchart of the Wind Driven Optimization implementation. A sample Matlab / Octave code is also provide in the Appendix A.

Next section carries out a numerical study on the coefficients of the WDO utilizing four different test function to discover the optimum values for these coefficients those lead to efficient performance of the WDO on different search topologies.

4.2. Numerical Parameter Study

The optimum performance of the WDO can be achieved by properly selecting the values for the coefficients that are utilized in the velocity update equation (4-15), and these coefficients are; α, g, RT, and c. Since all optimization problems differ from each other, the optimum choice for one optimization problem may not be a good choice for another problem. In order to determine the best parameter combination ranges, four different benchmark function are utilized [91], which are the *Sphere*, *Rotated Hyper-Ellipsoid*, *Ackley* and *Rastrigin* Functions. The description and properties of each function are provided in Table 4-3 for *N*-dimensions, and figures of these function in 2-D are illustrated in Figure 4-3, Figure 4-4, Figure 4-5, and Figure 4-6, respectively.

Table 4-3 : *N*-Dimensional modified test functions used in the numerical parameter study of the WDO algorithm. The global best position vector of each function is represented by **x***, and optimum values are indicated by $\boldsymbol{F(x^*)}$.

Function Name	**Description and Properties**
Sphere	$F_{SPH}(\mathbf{x}) = \sum_{i=1}^{N}(x_i - 5)^2$ $x_i \in [-10,10]$, $\mathbf{x}^* = (5,5,\ldots,5)$, $F_{SPH}(\mathbf{x}^*) = 0$
Rotated Hyper-Ellipsoid	$F_{RHE}(\mathbf{x}) = \sum_{i=1}^{N}\left(\sum_{j=1}^{i}(x_j - 28)\right)^2$ $x_i \in [-100,100]$, $\mathbf{x}^* = (28,28,\ldots,28)$, $F_{RHE}(\mathbf{x}^*) = 0$
Ackley	$F_{ACK}(\mathbf{x}) = 20 + e - 20\exp\left(-0.2\sqrt{\frac{1}{N}\sum_{i=1}^{N}(x_i - 5)^2}\right) - \exp\left(\frac{1}{N}\sum_{i=1}^{N}\cos(2\pi(x_i - 5))\right)$ $x_i \in [-32,32]$, $\mathbf{x}^* = (5,5,\ldots,5)$, $F_{ACK}(\mathbf{x}^*) = 0$
Rastrigin	$F_{RAS}(\mathbf{x}) = 10N + \sum_{i=1}^{N}\left((x_i + 0.5)^2 - 10\cos(2\pi(x_i + 0.5))\right)$ $x_i \in [-5,5]$, $\mathbf{x}^* = (-0.5,-0.5,\ldots,-0.5)$, $F_{RAS}(\mathbf{x}^*) = 0$

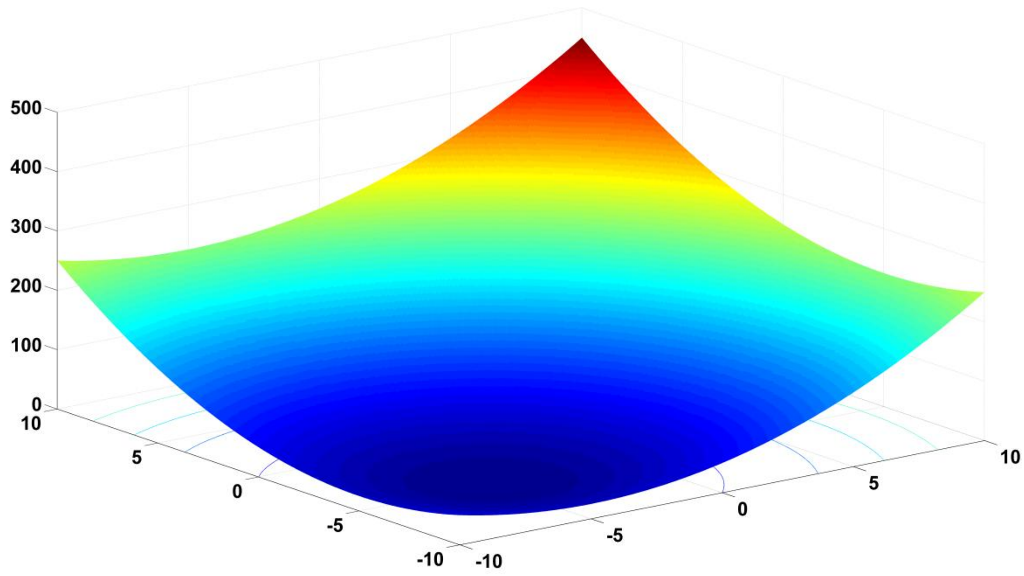

Figure 4-3: Two dimensional illustration of the modified Sphere function in the range of [-10, 10]. The properties of this function is given in Table 4-3.

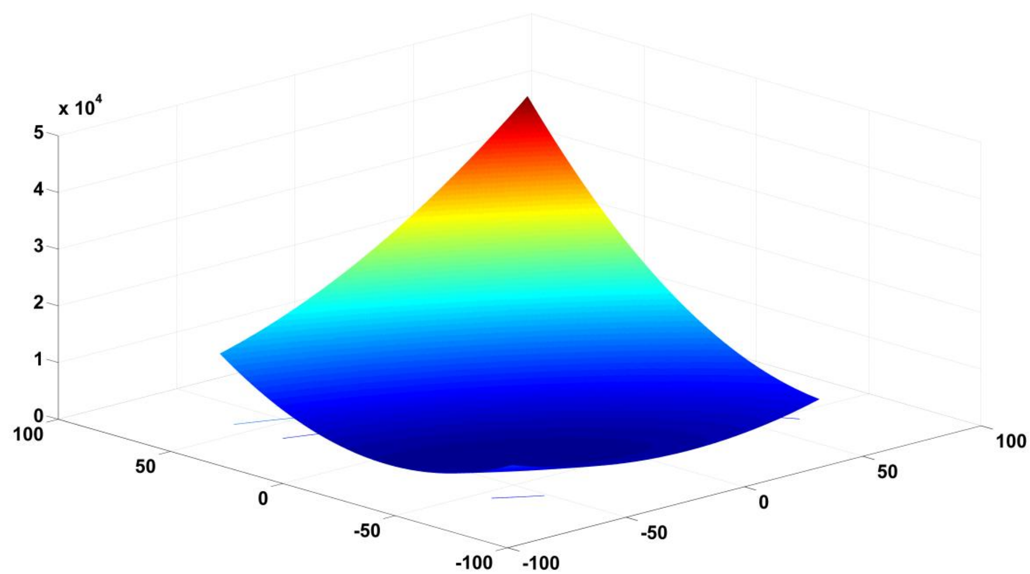

Figure 4-4: Two dimensional illustration of the modified Rotated Hyper-Ellipsoid function in the range of [-100, 100]. The properties of this function is given in Table 4-3.

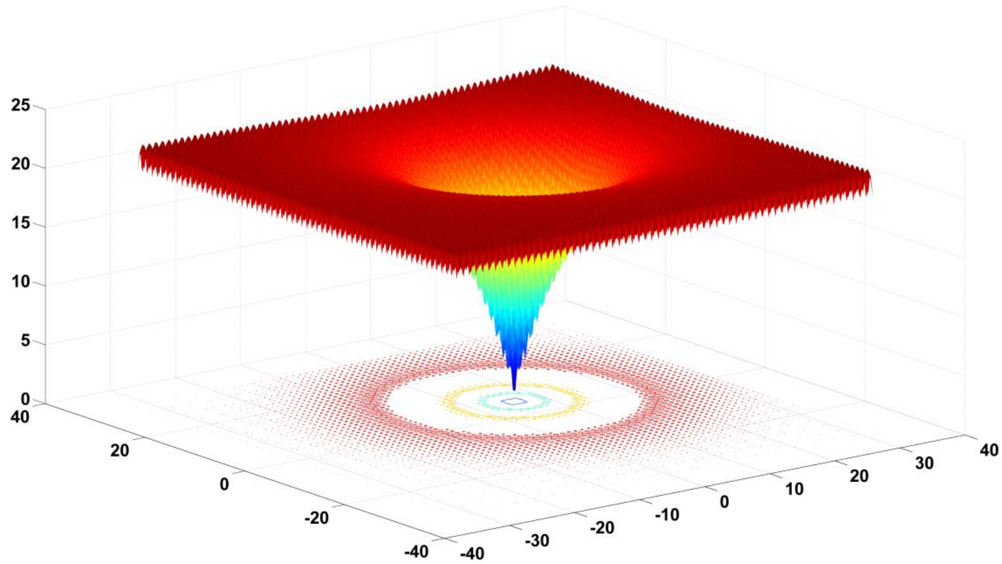

Figure 4-5: Two dimensional illustration of the modified Ackley function in the range of [-32, 32]. The properties of this function is given in Table 4-3.

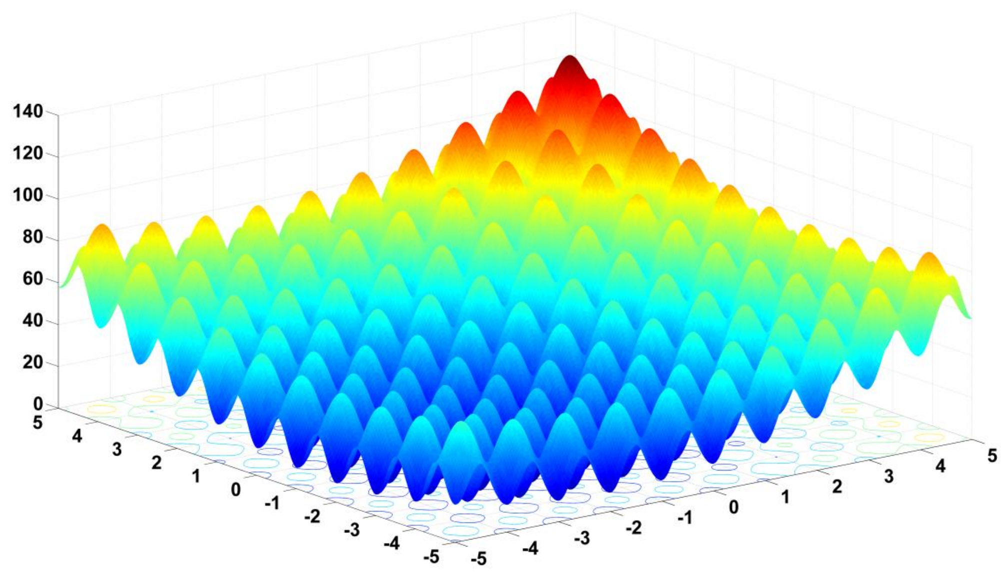

Figure 4-6: Two dimensional illustration of the modified Rastrigin function in the range of [-5,5]. The properties of this function is given in Table 4-3.

Each test function is defined in different ranges as shown in Table 4-3, and the total number of dimension is selected to be N=5 for the numerical study. It should be pointed out that the modified version of the benchmark functions is utilized in this study, where the global best locations, $\boldsymbol{x^*}$, are altered. Unmodified, all these test functions have a global best at the coordinate system center, which would be misleading for the WDO simply due to fact that the gravitational force would dominate overtime and all air parcels would converge to the solution. Unfortunately, such scenario would not provide any valuable information for the determination of the best values for the rest of the parameters. For this reason, the global best positions had to be modified.

A quick look at (4-15) points out that the friction coefficient, α, and the gravitational force coefficient, g, can only vary in the ranges of [0,1], while other coefficients, RT and c, can have a wider range of values. To accommodate all possibilities following values are tested for 10 different random seeds and results are plotted;

α = [0.01/0.03/0.05/0.07/0.09/0.1/0.2/0.3/0.4/0.5/0.6/0.7/0.8/0.9]
g = [0.01/0.03/0.05/0.07/0.09/0.1/0.2/0.3/0.4/0.5/0.6/0.7/0.8/0.9]
RT = [0.01/0.03/0.05/0.09/0.1/0.3/0.5/0.7/0.8/0.9/1.0/1.3/1.6/2.0/2.2/2.6/3.0/3.2/3.6/4.0/4.2/4.6/5.0]
c = [0.01/0.03/0.05/0.09/0.1/0.3/0.5/0.7/0.8/0.9/1.0/1.3/1.6/2.0/2.2/2.6/3.0/3.2/3.6/4.0/4.2/4.6/5.0]

Starting with the Sphere function, a population size of 50 air parcels were run for a maximum of 200 iterations for V_{max} = 0.3. To be able to study the effects of RT and c, other parameters fixed to following values; α = 0.5, g = 0.2. While the values for α and g are not optimal, they are still useful for the study of the parameters, RT and c.

The best pressure values for all test functions resulted for the following parameter ranges; $0.5 \le RT \le 2.2$ and $c = 0.7$, as seen in Figure 4-7, Figure 4-8, and Figure 4-9, whereas $c = 0.03$ was preferred in Figure 4-10, respectively. From this study, it seems like WDO would prefer RT in a large range of values, and c value less than 0.7.

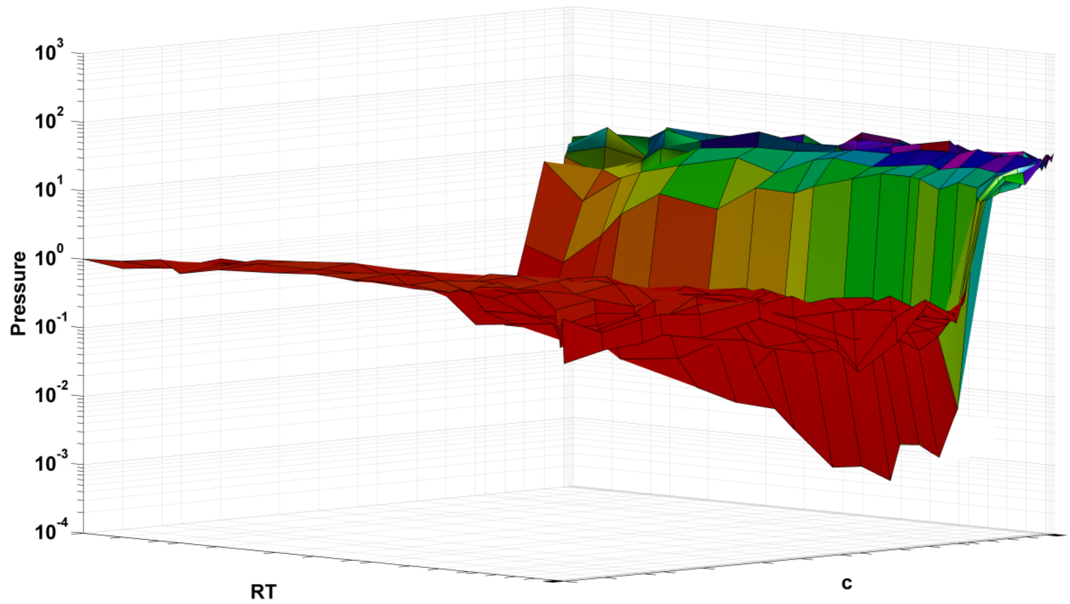

Figure 4-7 : Study of the coefficients of *RT* vs. *c* for the Sphere function with *N*=5.

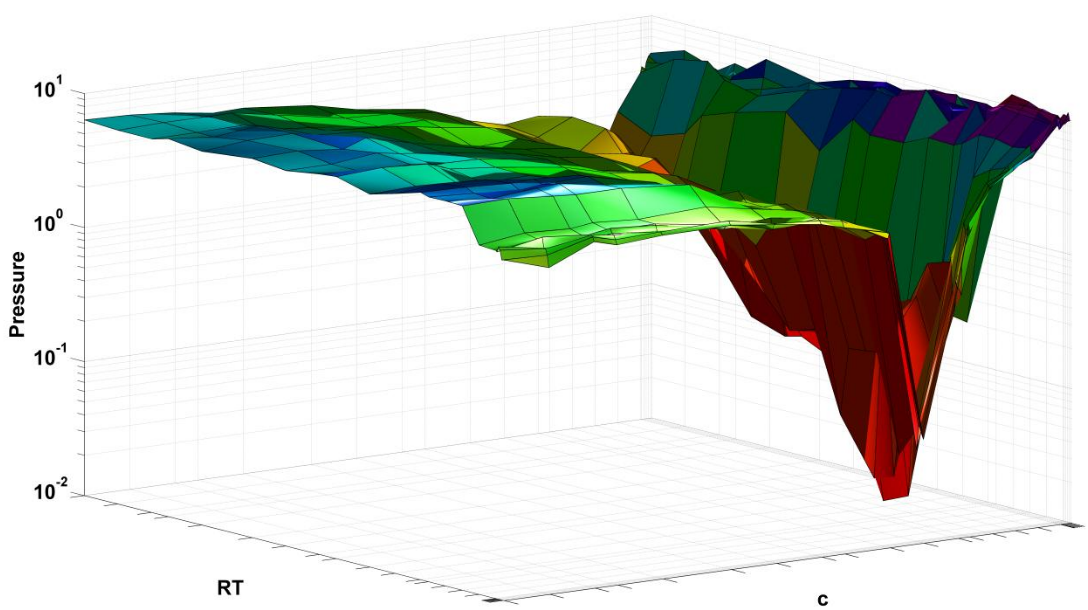

Figure 4-8 : Study of the coefficients of *RT* vs. *c* for the Ackley function with *N*=5.

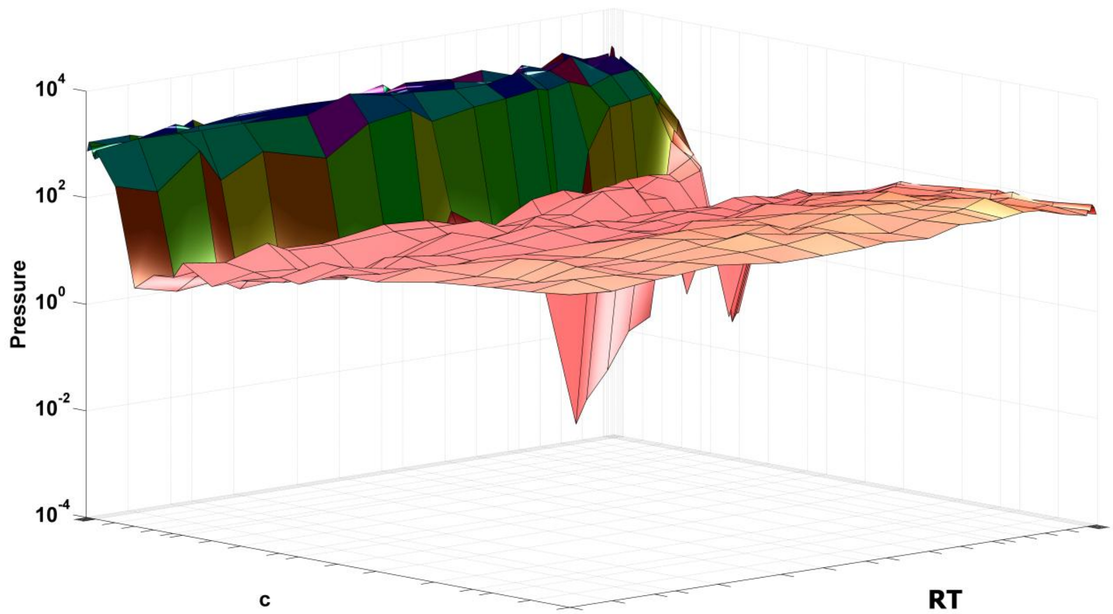

Figure 4-9 : Study of the coefficients of *RT* vs. *c* for the Rotated Hyper-Ellipsoid function with *N*=5.

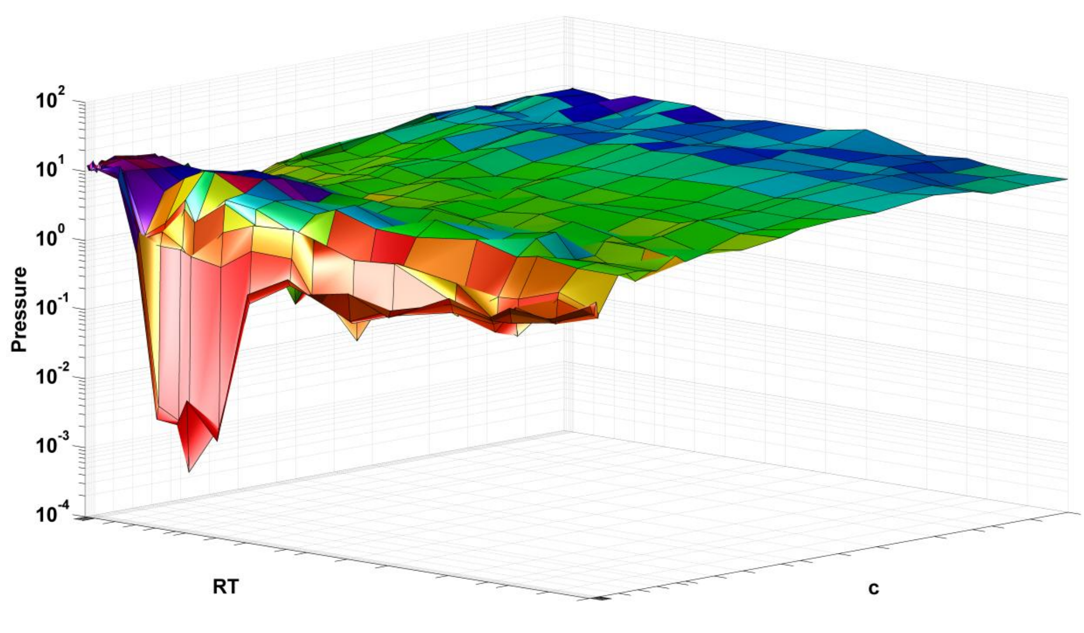

Figure 4-10 : Study of the coefficients of *RT* vs. *c* for the Rastrigin function with *N*=5.

For the next study, let's set RT = 0.8, and c = 0.9 and analyze α and g for a population size of 50 and maximum number of iteration of 200 for N=5 and V_{max} = 0.3.

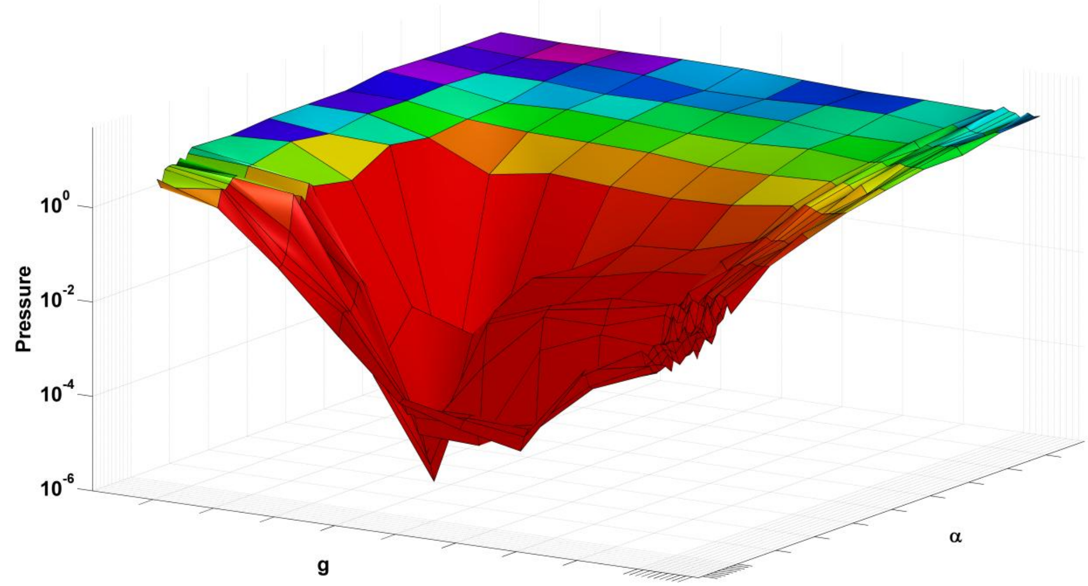

Figure 4-11: Study of the coefficients of α vs. g for the Sphere function with N=5.

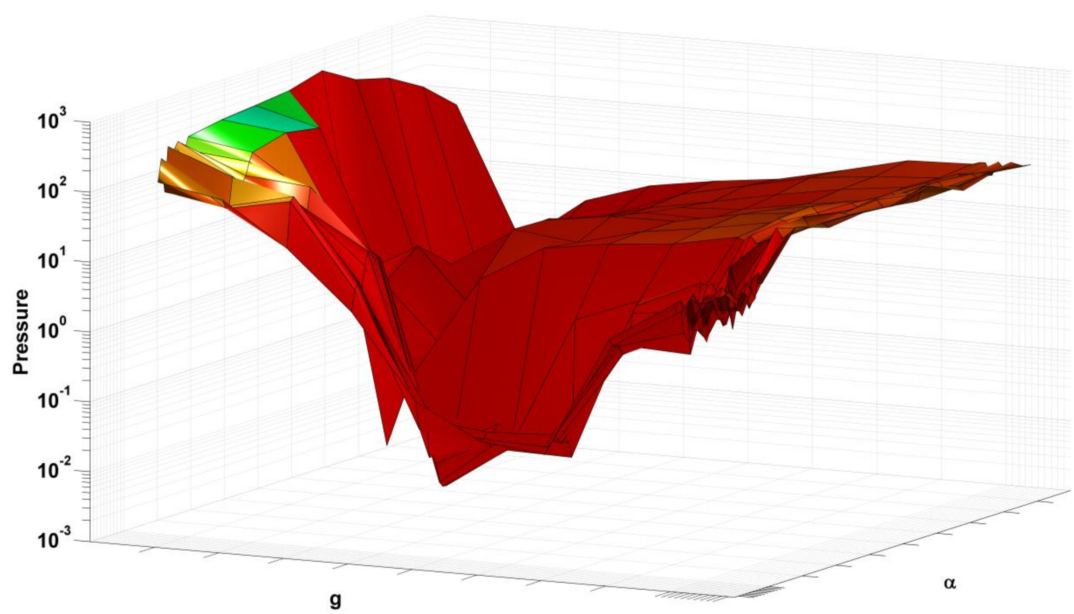

Figure 4-12: Study of the coefficients of α vs. g for the Rotated Hyper-Ellipsoid function with N=5.

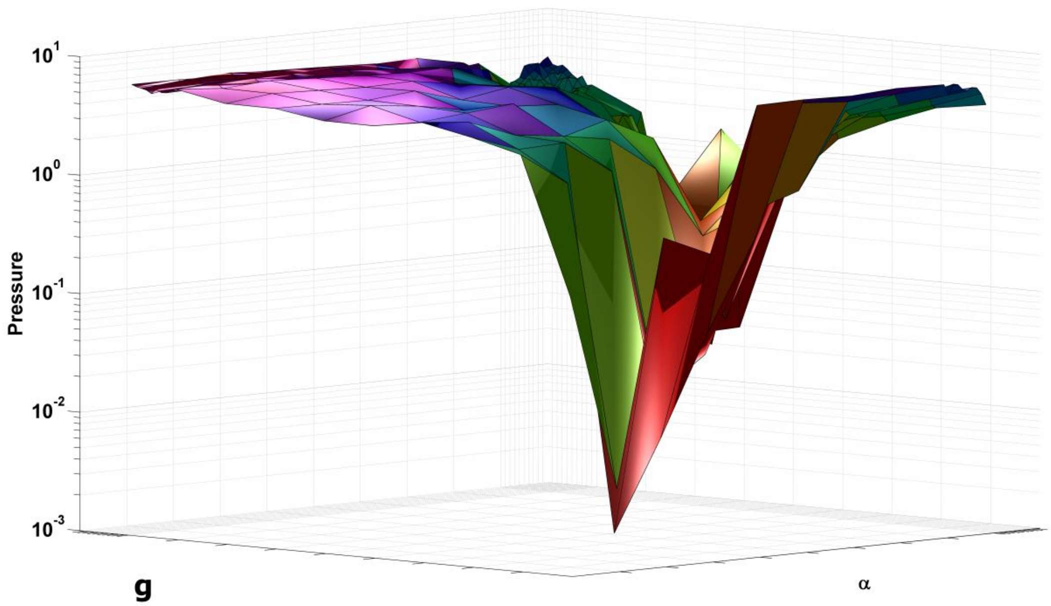

Figure 4-13: Study of the coefficients of α vs. g for the Ackley function with N=5.

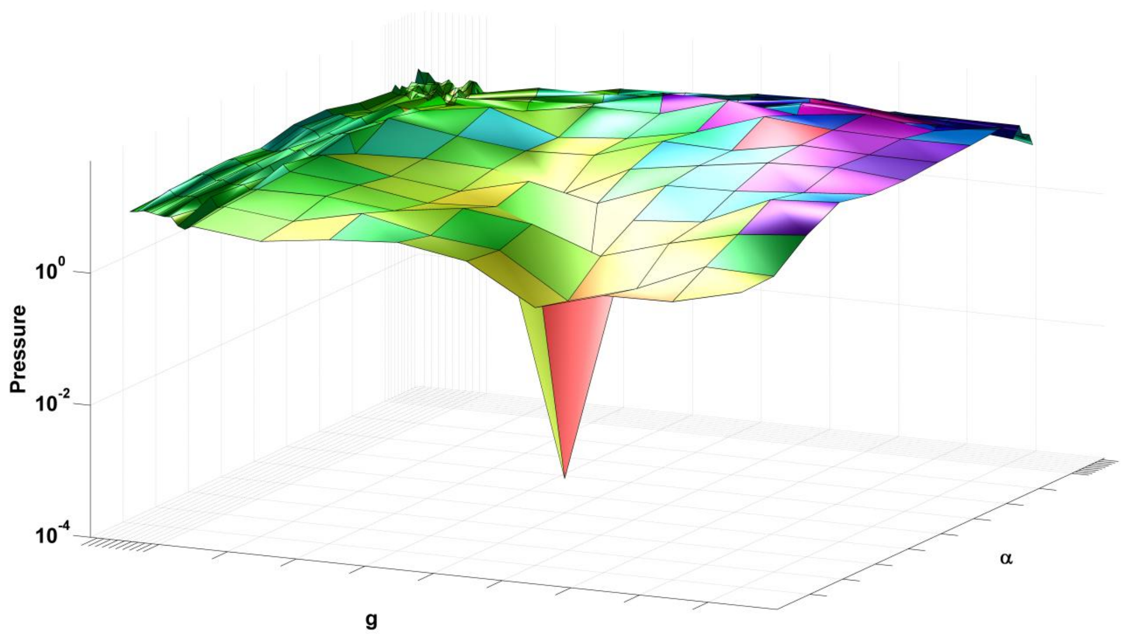

Figure 4-14: Study of the coefficients of α vs. g for the Rastrigin function with N=5.

The second study shows that for the unimodal functions, *i.e.* Sphere and Rotated Hyper-Ellipsoid, the values of α=0.1 or lower and g=0.5 provide good performance for the WDO, whereas for the multimodal functions, *i.e.* Ackley and Rastrigin, a different set of values may perform better. As seen from Figure 4-13, there is a range of values for α and g which almost looks like a linear relation between these two coefficients. There is almost a 1:1 ratio between α and g, specifically for the values ranging between 0.4 and 0.9, where WDO seems to perform better. In Figure 4-14, the Rastrigin function seem to prefer α = 0.6 and g = 0.5.

From these studies we can conclude that for some coefficients there might be a single best value, *i.e.* c, but for others, there is a range of values depending on the optimization problem at hand. In the following section, the WDO will be applied to electromagnetic optimization problems, some of which have been studied in the literature, and some are new contributions. Various implementation of WDO in electromagnetics should provide the confidence for the WDO as an efficient optimization tool.

4.3. Linear Antenna Array Synthesis

The linear antenna array synthesis has been studied many times in the literature utilizing various optimization methods [92] - [96] targeting sidelobe suppression, null placement, array thinning, or unique radiation pattern synthesis.

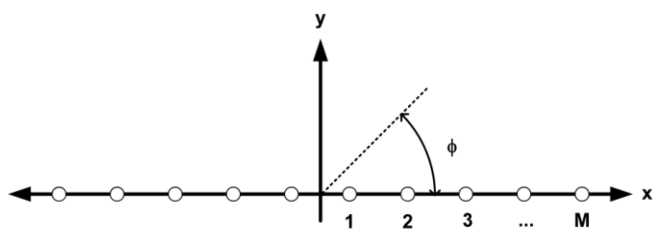

Figure 4-15: Geometry of the 2M-element linear antenna array is shown where elements are positioned along the x-axis. The antenna array is symmetric respect to the origin.

In this section, the WDO will be given the task to determine the optimum element layout of a linear antenna array to suppress the sidelobe levels (SLL) of the radiation pattern. For the radiating elements, isotropic radiators are assumed which are symmetrically positioned along the x-axis as seen in Figure 4-15. This same problem is addressed in [92] using the Particle Swarm Optimization, and for fair comparison between the PSO and the WDO, uniform excitation of amplitude ($a_i = 1$) with no phase differences ($\varphi_i = 0$) are assumed in (4-18).

The array factor for this linear antenna array can be simply written as,

$$AF(\phi) = 2\sum_{i=1}^{M} a_i \cos(k\, d_i \cos(\phi) + \varphi_i) \ , \tag{4-18}$$

where a_i, d_i and φ_i present the excitation amplitude, the location of the i^{th} antenna element and the phase of the excitation, respectively, where as k is the wavenumber.

For uniform excitation and no phase, the equation (4-18) simplifies to

$$AF(\phi) = 2\sum_{i=1}^{M} \cos(k\, d_i \cos(\phi)) \ . \tag{4-19}$$

The WDO will be used to find the optimum locations for the antenna elements, i.e. d_i, to achieve minimum SLL for antenna array size of 2M = 10. Since the main radiation beam is directed in the broadside ($\phi = 90°$), only the following bands [0°, 82°] and [98°, 180°] are optimized for minimization of SLL. According to [92], velocity vector of the PSO quickly nears to zero in about 400 iterations which causes PSO to lose its exploration ability.

The WDO ran with a population size of 20 air parcels for a maximum of 500 iterations. The following parameters are used for the coefficients; α=0.4, g=0.2, RT=3, and c=0.4 with V_{max}

= 0.3. The air parcels were to optimize the antenna distances where the range of [0, λ_0] was allowed. Following pressure function is utilized for the minimization of the array factor,

$$Pressure = \max\{AF_{dB}(\phi)\} \tag{4-20}$$

The dimensions of the optimized design is listed in Table 4-4, and its comparison against the PSO optimized array and conventional uniformly spaced antenna array is also illustrated in Figure 4-16.

Table 4-4: Element locations of the 10-element linear antenna array for different array geometries, where the distances are normalized with respect to λ_0.

	1st	2nd	3rd	4th	5th
Conventional	±0.25	±0.75	±1.25	±1.75	±2.25
PSO	±0.2515	±0.555	±1.065	±1.50	±2.11
WDO	±0.319	±0.8785	±1.5423	±2.3349	±3.1596

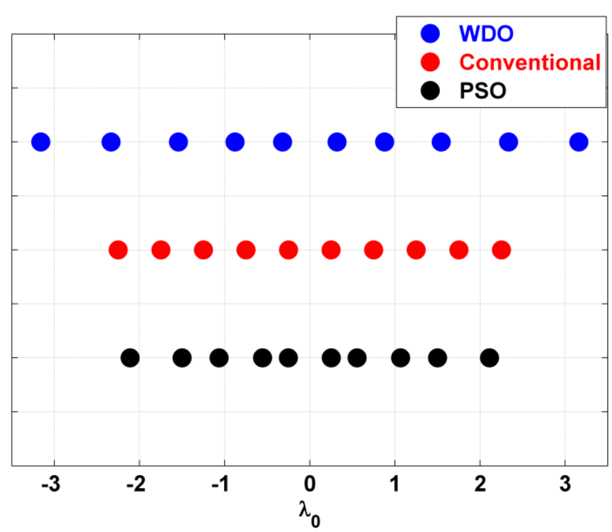

Figure 4-16: Comparison of the antenna geometries, WDO optimized, PSO optimized [92] and conventional uniformly spaced antenna array.

The WDO optimized linear antenna array provides a uniform sidelobe level distribution due to minimizing pressure function and the maximum SLL is -17.68 dB as seen in Figure 4-17. The conventional uniformly spaced λ/2 linear antenna array provides a maximum SLL of -12.96 dB, where as the PSO optimized array provides -17.41 dB. As it can be seen from the results, WDO can outperform the PSO performance in linear antenna array optimization.

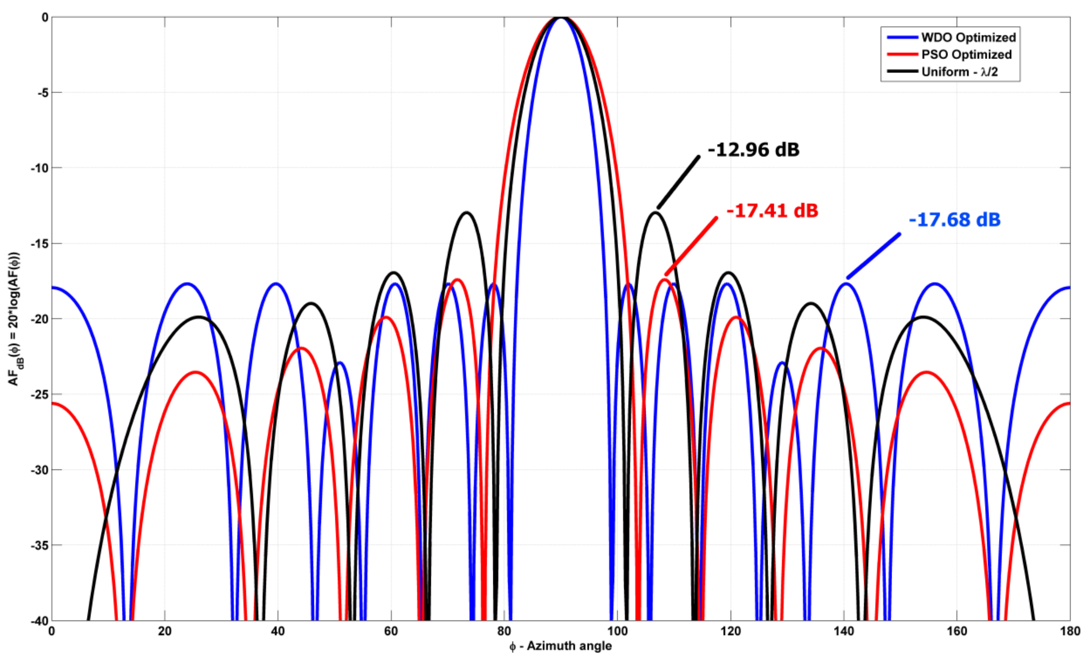

Figure 4-17: Array factor comparison of the WDO optimized linear antenna array against the conventional uniformly spaced antenna array and PSO optimized antenna array [92]. Maximum sidelobe levels for each antenna array are also labeled, where the WDO optimized array provides the lowest SLL among all.

4.4. Double-Sided Artificial Magnetic Conductor Synthesis

Artificial magnetic conducting ground planes are widely utilized in low profile antenna applications, where a radiating antenna element can be placed very close to the surface. This is possible due to the in-phase reflection that constructively interfere providing good input impedance match at the antenna feed, whereas a PEC ground plane would destructively interfere and reduce the efficiency of the antenna.

The theory of the double-sided artificial magnetic conducting (DSAMC) surfaces is introduced in Chapter 5 of this dissertation and various examples that are synthesized via Genetic Algorithm (GA). Thus, details of the design synthesis will be omitted here and one can refer to Chapter 5 for details. In shortest description, a DSAMC is a thin metallo-dielectric slab of engineered surface, which consists of two doubly periodic frequency selective surfaces (FSS) printed on either side of a thin dielectric slab of material. For the optimization example here, a commercially available dielectric layer of Rogers High Frequency Laminate™ RT 6010 with a dielectric permittivity of $\varepsilon_r = 10.2 - j0.0253$ and a thickness of 0.9 mm is utilized. The WDO is linked with a full-wave Periodic Finite Element Boundary Integral (PFEBI) solver for optimization of the top surface for artificial magnetic conductor (AMC) response and bottom surface for artificial electric conductor (AEC) response at the frequency of 10 GHZ.

Since the thickness, unit cell dimensions and dielectric permittivity are all preset, the WDO was given the task of optimizing the unit cell geometry of the top and bottom FSS structures. The square unit cell dimensions are set to be 1.0 cm in each dimension and the unit cells are pixilated into 16x16 grids for ease of optimization. The two pixilated FSS screen geometries are doubly periodic and share the same unit cell dimensions, where the WDO optimizes only one quarter of each FSS screen and four-folded symmetry is applied to complete the unit cells as illustrated in Figure 4-18. Each row represents a dimension with 8 bits, where the

WDO optimization range is in [0, 2^8]. Since there is a total of 16 rows to be optimized, this constitutes a N=16 dimensional optimization problem.

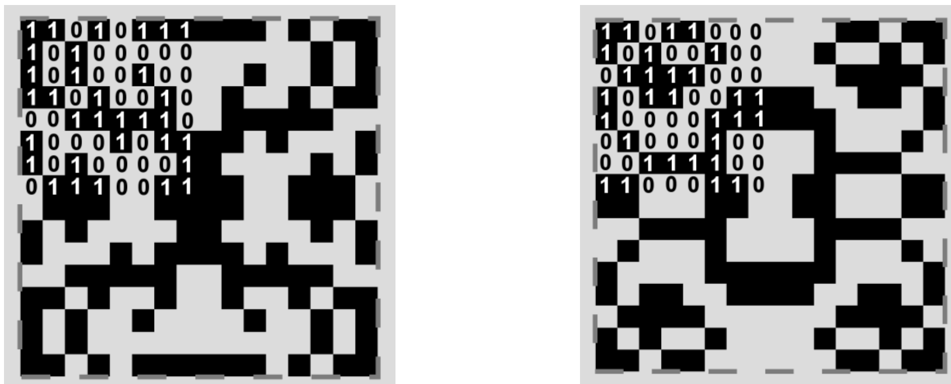

(a) (b)

Figure 4-18: WDO optimized unit cell geometries, (a) top FSS geometry shown with four-folded symmetry implementation, (b) bottom FSS geometry shown with four-folded geometry implementation.

A population of 30 air parcels was run for 200 iterations, where the following parameters are used for the coefficients; α=0.4, g=0.2, RT=3, and c=0.4 with V_{max} = 0.3. The optimized FSS geometries are illustrated in Figure 4-18, where the top surface behaves as an AMC and bottom surface behaves as a AEC as seen from the reflection phase and magnitude plots in Figure 4-19 and Figure 4-20, respectively, where the S_{11} is -0.8 dB and S_{12} is -13.18 dB. The unit cell boundaries are illustrated with the dashed gray lines in Figure 4-18, where the black shaded pixels represents the metal and gray pixels represent the absence of the metal where the dielectric is exposed. This optimization problem is better suited for binary-coded algorithms such as GA but the results show that the WDO can easily handle binary-coded optimization problems as well.

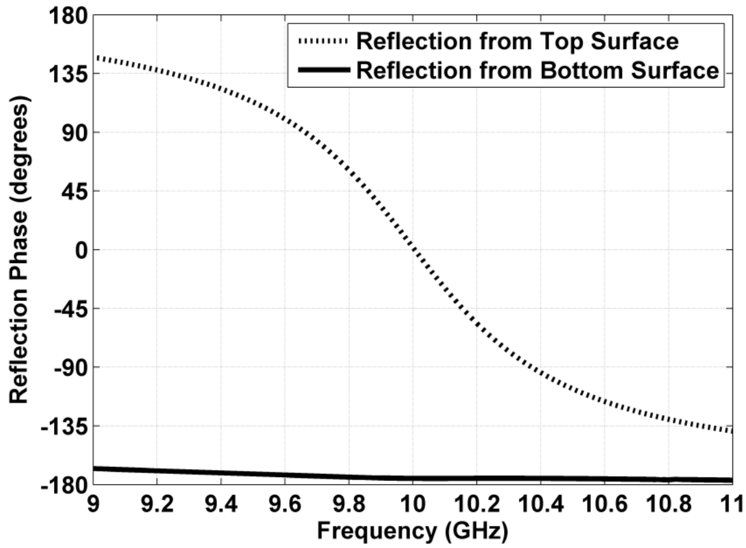

Figure 4-19: Illustration of the reflection phase values both from top surface and bottom surfaces. The top surface provides an in-phase reflection, *i.e.* AMC band, at 10 GHz and bottom surface provides out-of-phase reflection, *i.e.* AEC band, at 10 GHz.

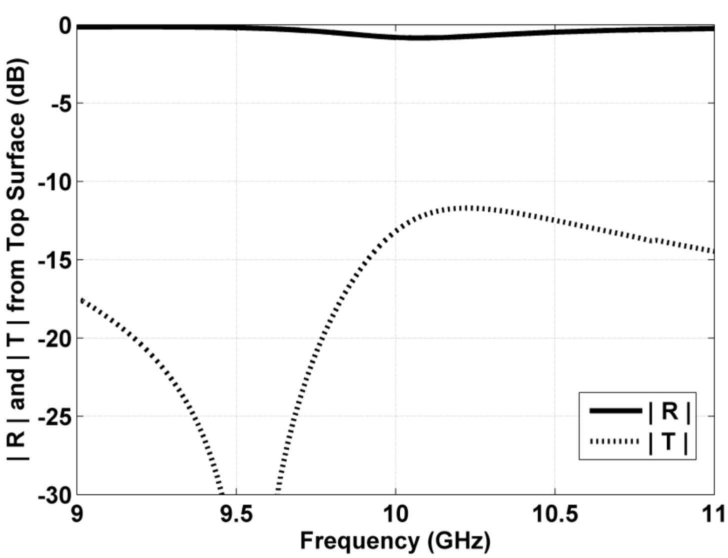

Figure 4-20: Illustration of the reflection and transmission magnitudes from top surface. A highly reflective surface is achieved at 10 GHz.

4.5. Stub-loaded Inverted-F Antenna Synthesis

In this section, the WDO is given the task to optimize a novel low profile wire antenna with a high gain in the broadside direction. For the design examples presented in this chapter, the target frequency of 500 MHz is chosen. The proposed novel antenna is a low profile wire antenna in the shape of an inverted-F antenna (IFA), which is loaded with two optimized length wire stubs at optimum locations along the antenna body, hence the name stub-loaded inverted-F antenna (SLIFA).

Based on their geometries, there are two general categories that the conventional IFAs can be classified into, which are namely the wire IFAs and planar IFAs (PIFAs). In either category, the antenna consists of four fundamental metallic elements; a ground plane, a radiating plate or a wire that is certain distance above the ground plane, a vertical feeding structure and a vertical shorting pin connecting the radiating section to the ground plane.

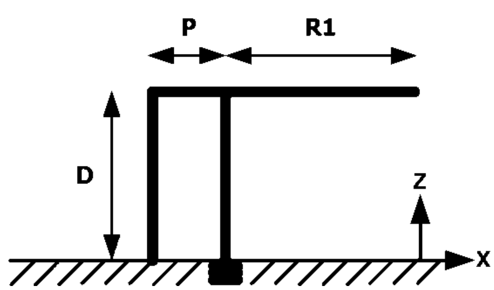

Figure 4-21: Illustration of a conventional wire IFA, where **D** is the distance between the radiating element and the ground plane. The antenna is fed by a coax connector through the vertical center wire connecting at a point between P and R1.

As seen in Figure 4-21, the antenna can be viewed as a wire monopole antenna folded parallel to the ground plane at a certain distance, D, above with a shorting pin attached at a strategic location along the antenna, shown with a distance P in Figure 4-21. Its shape looks like an inverted F, which can be fed by a coax at the vertical center wire. The bent wire and the ground plane couple strongly, that can be compensated by proper placement of the shorting pin, which allows the better control of the input impedance resulting in a low profile resonant antenna. The radiation pattern of a conventional wire IFA is similar to a conventional monopole, with a null at broadside (*i.e.* $\theta = 0°$), as illustrated in Figure 4-24. A detailed numerical study of the IFA is performed in [97] and optimal dimensions are reproduced in Table 4-5. Additionally, several studies in the literature attempted various performance improvements on the IFA. It was shown in [98] and [99], that utilization of parasitic elements together with the driven element in the IFA geometry can improve the impedance matching and provide improved VSWR bandwidth without any effect on the radiation or the gain. To reduce the antenna length, Schulteis *et al.* [100] replaced one of the wires, designated by R1 in Figure 4-21, with a smaller size circular segment thus capacitively loading the antenna and achieving smaller length. At the expense of having a higher profile, wire IFAs can be loaded by stacking additional inverted L shaped wires on top of the upper wire. Such loading achieves a multi resonance response and increased gain, while the antenna profile is much higher compared to its unmodified shape [101]. Loop-shaped IFAs along with additional parasitic elements within the feeding element are investigated in [102] to achieve dual resonance operation.

Werner *et al.* has shown that stub-loading an electrically long wire could achieve omnidirectional high gain at the expense of longer total antenna length [103]-[104]. Similarly, stub-loading technique can be applied in the design of SLIFAs to achieve high broadside gain. The objective in the synthesis of SLIFAs is to achieve highest possible gain in the broadside direction at 500 MHz as well as achieving lower profile compared to the conventional IFAs. For the designs considered here, only the designs with two stubs are optimized by the WDO to achieve the desired performance. The geometry of a SLIFA is illustrated in Figure 4-22.

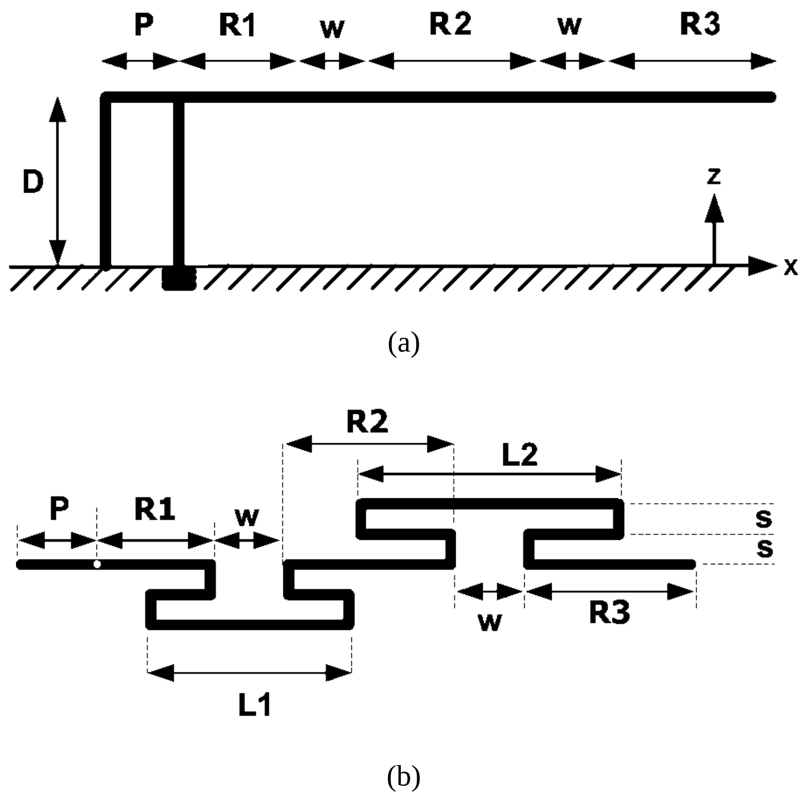

Figure 4-22: (a) Side view of a stub-loaded inverted-F antenna (SLIFA), (b) Top view of the same antenna. Dimensions of an IFA and optimized SLIFAs are provided in Table 4-5.

The electrically long antenna typically introduces drawbacks and undesirable features, such as poor impedance match and multi-lobes in the radiation pattern, but adding optimized stubs at optimized locations along the antenna body can compensate for these features as well as they could provide certain benefits. The WDO is given the task to optimize the stub locations (R1, R2, R3), the stud lengths (L1, L2), the stub insertion separation (w), the distance from the ground (D), as well as the stub separation distance from the antenna body (s) to achieve a good input impedance at 500 MHz while providing high gain at the broadside direction (z-axis), where IFA has a null.

The optimization goals are incorporated into the *Pressure* function of the optimization as given in (4-21), where the minimization of the pressure will be achieved for lower S_{11}(dB) and higher gain (dB),

$$Pressure = |\ 20 + S_{11}\ | + |\ 20\ -\ \mathrm{Gain}(\theta=0°)\ | \qquad (4\text{-}21)$$

In the optimization of the SLIFAs, the WDO is linked with the Method of Moments (MoM) solver of the commercially available FEKO software for fast evaluation of the candidate designs. When used in wire antenna design problems, particularly on infinite ground planes, MoM provides very accurate results very fast. The performance of the optimized antenna designs are then confirmed with Ansoft HFSS, which utilizes a finite element solver, both on infinite and finite size ground planes.

This optimization constitutes a N=9 dimensional problem, where dimensions are listed in Table 4-5. For the first design example presented here, a population of 50 air parcels ran for 200 iterations with the following coefficient values during optimization process; $\boldsymbol{\alpha}$ = 0.4, $\boldsymbol{g}$ = 0.2, $\boldsymbol{c}$ = 0.4, $\boldsymbol{RT}$ = 3, $\boldsymbol{V_{max}}$ = $\underline{+}$ |0.3|. FEKO evaluates the input impedance and radiation pattern of each candidate design, which are then used in the *Pressure* function as shown in (4-21). The height D of the final design is only 0.08 λ_0, which represents a lower profile than that of a conventional IFA along with a broadside gain of 8.2 dB, where as the IFA has a null.

In Figure 4-23, the S_{11} of the optimized design is compared to a conventional IFA, where both FEKO and HFSS calculations are shown on infinite size ground planes. Save for a small frequency shift, both solvers show a resonance at around 500 MHz. Changing the ground plane size to 2 λ_0 by 2 $\lambda_{0.}$ does not degrade neither the S_{11} performance nor the gain pattern, where the radiation pattern cuts are illustrated in Figure 4-24.

Table 4-5: Dimensions of the conventional IFA and both of the optimized SLIFA design examples are listed, where dimensions are shown both in mm and in terms of wavelength.

Dimen.	IFA	IFA	1st SLIFA	1st SLIFA	2nd SLIFA	2nd SLIFA
	(mm)	(λ_0)	(mm)	(λ_0)	(mm)	(λ_0)
D	66.00	0.110	48.00	0.08	48.00	0.08
P	24.00	0.040	50.48	0.084133	59.76	0.0996
R1	94.00	0.1567	289.41	0.48235	270.30	0.4505
R2	-	-	223.62	0.3727	94.66	0.1577
R3	-	-	60.00	0.10	204.88	0.3414
L1	-	-	84.50	0.14083	133.37	0.222
L2	-	-	239.17	0.3986	304.35	0.507
w	-	-	54.50	0.9083	70.99	0.1183
s	-	-	67.88	0.1131	82.09	0.1368

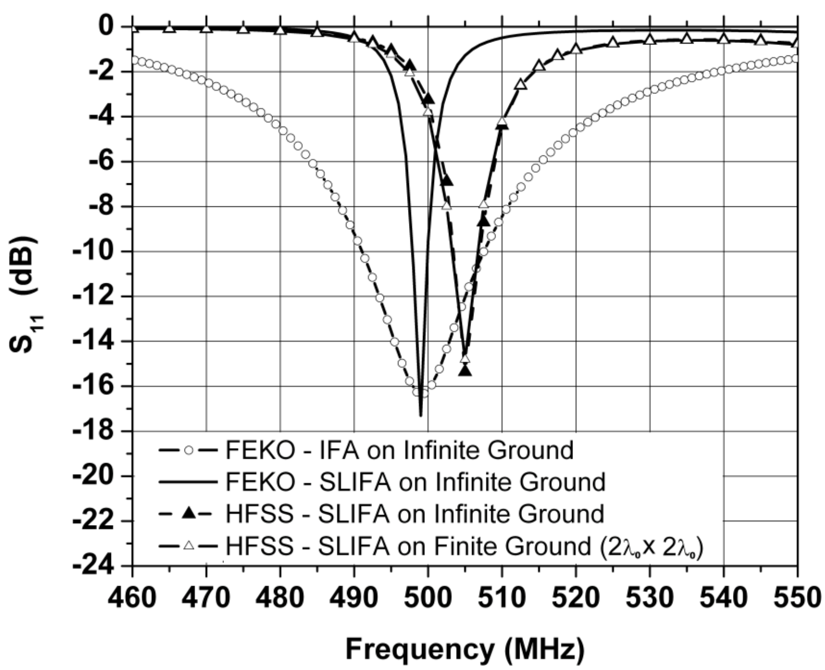

Figure 4-23: S_{11} comparison of the first optimized SLIFA design against the conventional IFA, where both FEKO and HFSS results are shown.

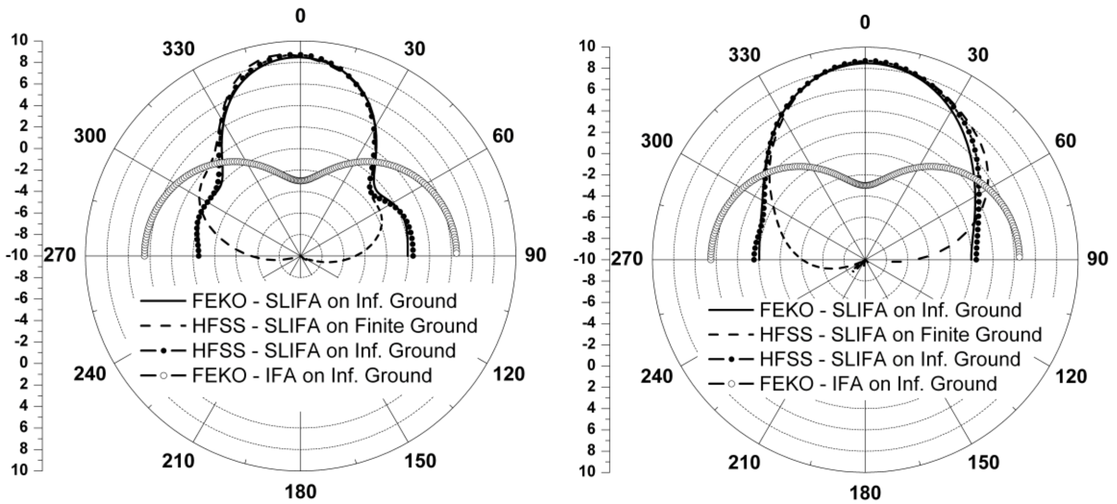

(a) (b)

Figure 4-24: (a) Radiation pattern comparison in the XZ plane, (b) Radiation pattern comparison in the YZ plane.

For the second design example, the WDO was allowed to run for 300 iteration with a population size of 50 air parcels. The coefficients used were ; $\boldsymbol{\alpha}$ = 0.4, $\boldsymbol{g}$ = 0.2, $\boldsymbol{c}$ = 0.4, $\boldsymbol{RT}$ = 3, $\boldsymbol{V_{max}} = \pm |0.3|$ and FEKO was utilized for the evaluation of the antenna designs, where the *Pressure* is calculated based on

$$Pressure = |\,10 + S_{11}\,| + |\,25 - \mathrm{Gain}(\theta{=}0°)\,| \tag{4-22}$$

The dimensions of the final design is provided in Table 4-5, where the height of the antenna is 0.08 λ_0 and the antenna resonates nearly at 500 MHz with a broadside gain of 10.10 dB. The S_{11} of the antenna on infinite ground plane is illustrated in Figure 4-25 and the two plane cuts of the radiation pattern is shown in Figure 4-26. A high gain of 10.10 dB can be observed at the broadside of the antenna.

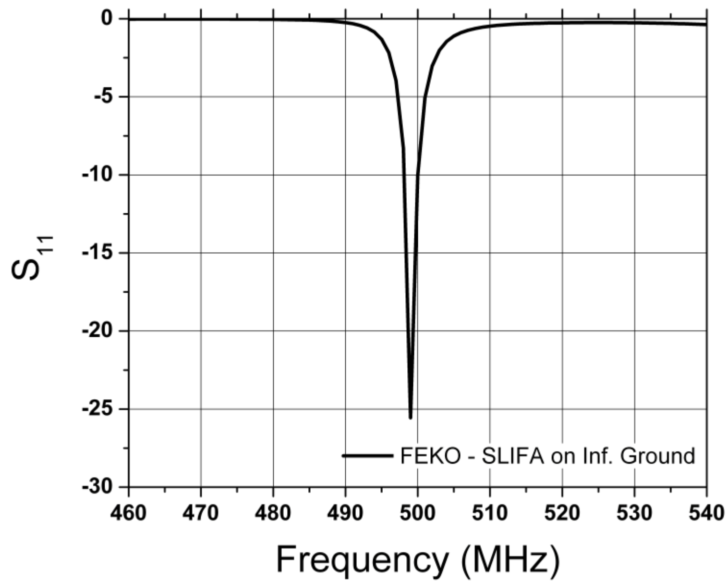

Figure 4-25: S_{11} performance of the second optimized SLIFA design, where the antenna is placed on infinite ground plane.

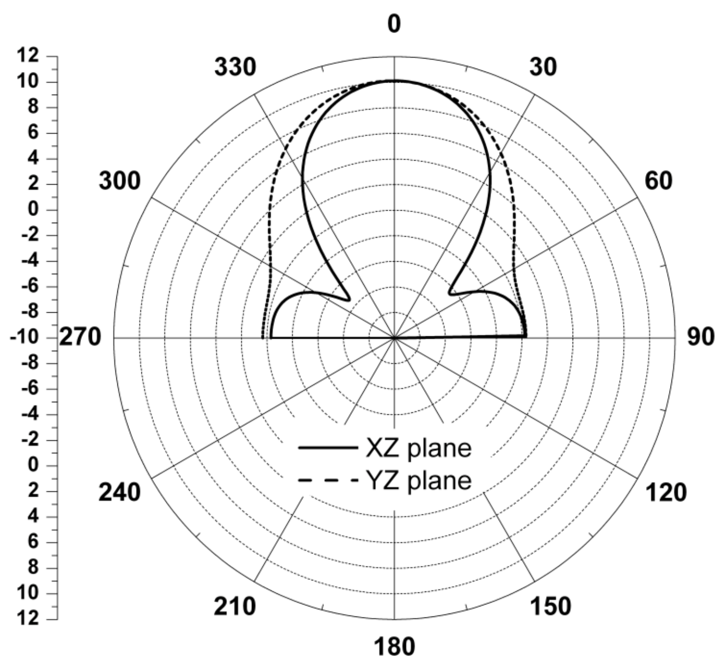

Figure 4-26: Radiation pattern cuts for the second optimized SLIFA antenna, where the coordinate system is referred in Figure 4-22.

4.6. Summary

In this chapter of the dissertation a novel numerical nature-inspired optimization algorithm called the Wind Driven Optimization (WDO) is introduced, and the theory behind the WDO is discussed in detail. A numerical study conducted for determination of the best parameter values, and efficiency of the WDO is illustrated by applying it to various electromagnetics optimization problems.

Chapter 5

Double-Sided Artificial Magnetic Conducting Surfaces

This chapter introduces a novel methodology for the design synthesis of thin planar realization of the volumetric artificial magnetic conducting surfaces (AMC). Several examples of thin double-sided AMC ground planes that are optimized for use in the X-band will be presented along with additional design examples that provide AMC behavior on one side and absorber behavior on the other are discussed. A system example illustrating the utility of the double-sided AMC separator between vertical antennas is shown for operation at the standard Wi-Fi frequencies of 2.4 GHz and 5.2 GHz.

5.1. Introduction

Over the past decade, the development of artificial magnetic conductors (AMC) has become an area of increasing interest. Sievenpiper [8] *et al.* has demonstrated the first AMC metamaterial ground plane realization which consisted of a doubly periodic array of mushroom-like metallic structures with square, rectangular or hexagonally shaped patches linked to a complete metallic ground plane with vertical metallic vias. The designs present a resonant high-impedance surface, where the tangential magnetic field is small and hence the artificial magnetic conductor behavior can be observed. In addition to an AMC band of operation, the propagation of electromagnetic waves at certain frequencies is prohibited, hence these structures can also be called as an electromagnetic bandgap (EBG) material. Ma *et al.* took a metamaterial approach to design high impedance AMC surfaces [9], where they replaced mushroom shaped structures with a complex metallic frequency selective surfaces (FSS). With this realization of a doubly periodic electromagnetic bandgap (EBG) structure, the FSS unit cells are printed on a dielectric substrate, which is backed by a complete metallic ground plane and omits the vertical vias providing a simpler fabrication process. To obtain more control of the behavior and the operating frequency of the structures, Kern *et al.* optimized FSS-based EBG structures with a Genetic Algorithm (GA) for multiband response, angular stability, and a broadband AMC condition using magnetic loading [14], [105]. These FSS-based EBG structures are fabricated rather easily using printed circuit technology, making them ideal for low-profile antenna applications. They can be easily mounted on a metallic platform such as the fuselage or wing of an aircraft, yet recent trends in aircraft construction lend to the increased use of composites. Thus, there is a growing interest in metamaterials that do not require a complete metallic backplane, which can be easily integrated in low-profile and embedded antenna systems.

The first volumetric AMC realization for antenna applications was introduced by Erentok *et al.* in [2]. Their design consisted of stacked layers of vertically oriented capacitively loaded loops (CLL), which provides AMC response on one surface and artificial electric conductor (AEC) response on the other. This realization eliminates the need for a complete metallic ground plane backing and is well-suited for antenna applications on composite platforms. This realization comes with two drawbacks, however. First, the structure must be electrically thick, consisting of at least two CLLs to attain AMC behavior, which results in a structure thickness of approximately $\lambda_r/3$ within the dielectric. For practical applications involving low-profile antennas, it is desired that the thickness of the volumetric AMC ground planes to be thinner than the traditional quarter wavelength antenna standoff distance from a metallic ground plane. Secondly, the vertical orientation of the CLLs require multiple stacks which are aligned and glued to each other, making fabrication cumbersome. Utilizing this method, Ferrer *et al.* constructed volumetric metamaterial AMC separators for decorrelation of two closely spaced monopole antennas [106], and in a similar attempt, Bait-Suwailam *et al.* utilized split ring resonators (SRRs) to design single-negative magnetic metamaterials to reduce the mutual coupling between two high-profile antennas [107].

In this chapter, a new design technique is introduced for the realization of thin, planar, and easily fabricated volumetric metamaterial AMC surfaces. The technique is based on using a Genetic Algorithm [5] to optimize two cascaded FSS screen geometries printed on each side of a thin dielectric substrate to achieve a highly reflective composite structure that does not possess a complete metallic ground plane. The response from either side of the composite structure can be independently optimized for AMC, AEC, or absorber behavior at a desired frequency or over multiple frequency bands. This provides great flexibility for composite antenna systems with ease of planar fabrication techniques.

5.2. Overview of Volumetric AMC Surfaces

Erentok *et al*. demonstrated in [2] that it is possible to design volumetric metamaterial AMC slabs for antenna application by utilizing stacked capacitively-loaded loops (CLLs). This metamaterial, shown in Figure 5-1, is doubly periodic in the XY plane and does not possess a complete ground plane yet it still provides AMC response for a wave propagating in the -z direction. If a wave traveling in the +z direction encounters the same structure, then the slab provides artificial electric conductor (AEC) response. In its simplest form, the metamaterial slab consists of a two CLL-deep unit cell along the z-axis. The in-house developed full-wave PFEBI solver was used not only to verify the results in [2], but also to demonstrate the accuracy of PFEBI for the GA optimization schema. Since PFEBI is a periodic structure solver, it is sufficient to analyze only one unit cell of the volumetric AMC structure. The unit cell dimensions for this structure are 5.1 mm in the y-direction, 0.75 mm in the x-direction and 6.45 mm in the z-direction.

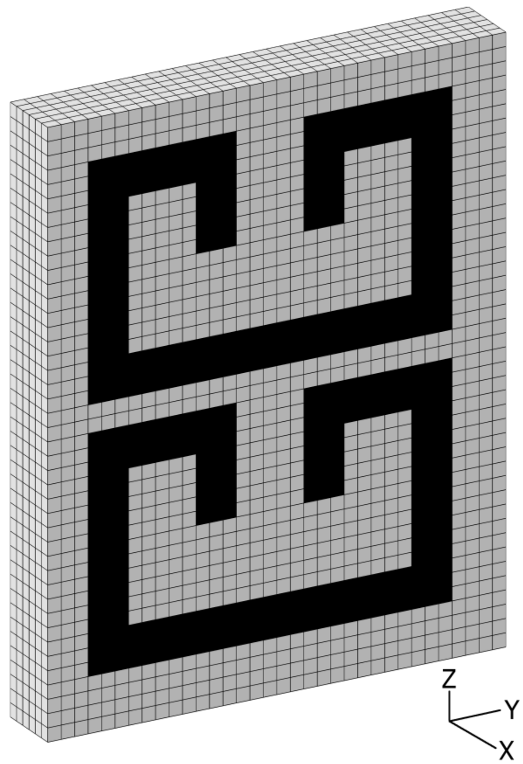

Figure 5-1: Pixelized two CLL-deep unit cell geometry for the Periodic Finite Element Boundary Integral (PFEBI) method simulation. The black colored pixel faces represent the printed metal (PEC) and gray colored pixels represent the absence of metal where the dielectric is exposed. The structure is doubly periodic in the XY plane and TM plane wave that is traveling along the z-axis, is impinging on top and bottom surfaces.

The PFEBI tool utilizes brick elements in its solver hence each dimension of the unit cell is discretized in to bricks of nearly equal dimensions. The dimensions of each brick element in Figure 5-1 are set uniformly as $\Delta x = 0.125$ mm, $\Delta y = 0.15$ mm, $\Delta z = 0.15$ mm. Black pixels represent a perfectly conducting (PEC) metal screen on the face of a pixel, while grey shaded pixels represent the absence of metal, where the dielectric is exposed. Dielectric permittivity is set to $\varepsilon_r = 2.2$ and response of this slab is computed for TM wave propagation along the z-axis in the X-Band, *i.e.* 8-12 GHz. The free space wavelength at 10 GHz is $\lambda_0 = 30.0$ mm and the wavelength in the dielectric medium is $\lambda_r = 20.23$ mm. Considering the total thickness of the slab in the z-direction is 6.45 mm or 0.319 λ_r, this AMC structure is quite thick for practical applications involving low profile antennas. The magnitudes and phases of the reflection and transmission coefficients as calculated by the PFEBI solver are displayed in Figure 5-2. S_{11} designates the reflection from the top surface, where the openings of CLLs are directed and S_{22} designates the reflection from the bottom surface, where the continuous parts of the CLLs are directed. The phase value of S_{11} passes through the zero at 9.90 GHz, hence the top surface of the metamaterial behaves as AMC. The magnitude of the S_{11} at 9.90 GHz is -0.051 dB and S_{21} is -29.08 dB, respectively. On the other hand, the phase and the magnitude of the S_{22} are 170° and -0.025 dB, respectively. This demonstrates that the bottom face of the metamaterial behaves as an AEC without requiring a complete metallic ground plane and PFEBI simulations provide excellent agreement with the results provided in [2].

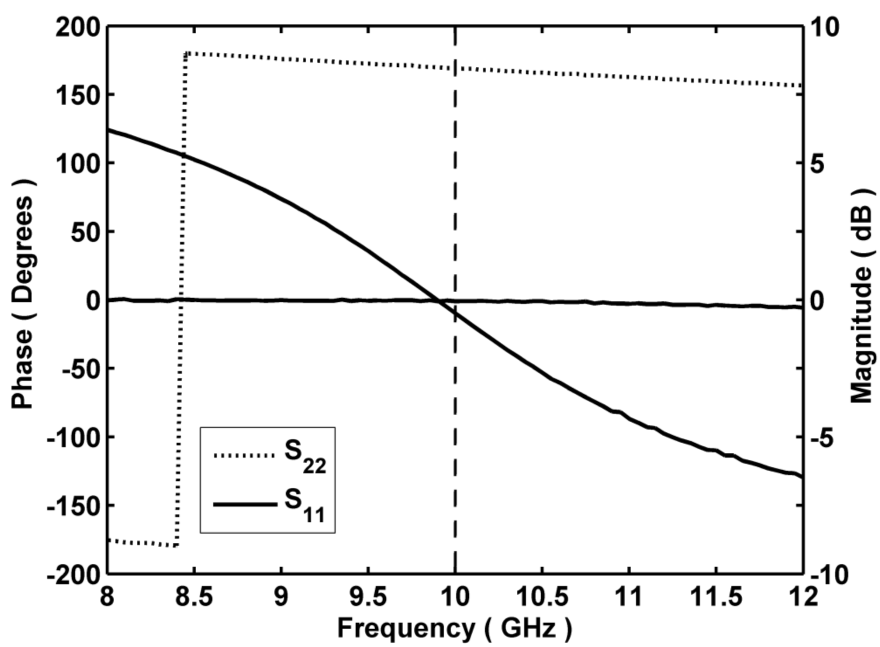

Figure 5-2: TM reflection and transmission phase and magnitude from the top and bottom surfaces of the doubly periodic two CLL-deep volumetric AMC structure calculated by the PFEBI. The phase values for the reflection from top surface show an in-phase reflection (solid line) with the zero phase crossing at 9.90 GHz, whereas phase values for the reflection from bottom surface show out-of-phase reflection (dashed line). PFEBI results agree very well with the results presented in [2].

5.3. Planar Double-Sided AMC Surfaces

The proposed composite structure consists of two optimized metallic FSS screens printed on opposite sides of a commercially available dielectric slab, as shown in Figure 5-3. The doubly periodic FSS screens share the same unit cell dimensions. Each square unit cell is divided into an equal number of pixels and four-fold symmetry is applied in FSS design. For practical applications, the thickness of the composite structure is limited to a thickness less than $\lambda_r/10$ at the optimization frequency of 10 GHz. Using standard printed circuit fabrication technology, the FSS screens can easily be etched on the appropriate side of the substrate.

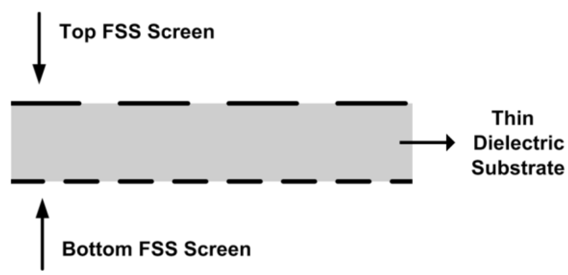

Figure 5-3: Cross-sectional diagram of the proposed AMC structure. The top and bottom FSS screen geometries are optimized by the GA optimization procedure. Material properties and thickness of the thin dielectric substrate are predefined before optimizations, hence only the FSS geometries are optimized

A standard binary-coded GA is used to optimize the each metallic FSS. Shown in Figure 5-4, the unit cell is divided into 16 by 16 pixels, where only one quarter of each unit cell is optimized because of four-fold symmetry. The metallic pixels are shown with black color in Figure 5-4 and represented with a "1" in the GA chromosomes, where as the absence of metallic pixels is shown in gray and represented by a "0" in the chromosome. The design optimization targets a highly reflective composite structure with surfaces having either AMC, AEC or double-sided AMC behavior. The GA is linked via a fitness function to the full-wave Periodic Finite-Element Boundary Integral (PFEBI) electromagnetic solver for calculation of reflection and transmission magnitudes and phases [76], which we also utilized in the previous section to verify the results provided in [2].

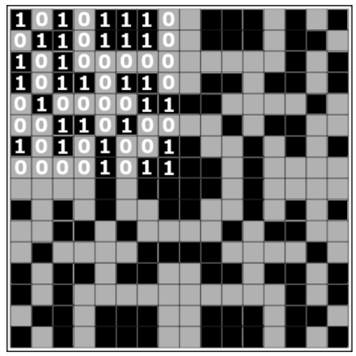

Figure 5-4: GA chromosome mapping to the top and bottom FSS geometries. Metallic patch covered pixels are illustrated with black color and dielectric exposed pixels are illustrated with gray color. Binary GA chromosomes are mapped such that a "1" represents a metallic patch pixel and a "0" represents absence of metallic pixel. Four-folded symmetry is applied to simplify the structure.

5.4. Genetic Algorithm Optimization

The GA is a widely used in this dissertation due to ease of implementation and efficiency in optimizing discrete-valued problems. The binary-valued GA is well suited for discrete-valued parameterization in the design synthesis of the thin double-sided AMC structures. The dimensions of the unit cell, thickness of the substrate, and permittivity of the dielectric substrate are predefined; the GA is used to search for the best FSS geometries to obtain the desired surface response. For fast and accurate numerical analysis of the composite structures, the GA is linked with a full-wave Periodic Finite Element Boundary Integral (PFEBI), where the structures that are selected by the GA are evaluated and scattering coefficients are returned for the cost computations. A simple cost function of

$$Cost = \left| 1 - R_{Top}^{10GHz} \right| , \tag{5-1}$$

can be used to obtain AMC conditions, where R_{Top} represents the complex reflection coefficient from the top surface of the composite structure at the optimization frequency of 10 GHz. For the top surface to behave as an AMC, high in-phase reflection is desired, *i.e.* $R_{Top} = 1$. Keeping the practical applications in mind, an acceptable design threshold of -10 dB is defined as minimum criteria for the transmission magnitude. The GA is permitted to run until the maximum number of iterations is reached or the fitness goal is obtained.

5.5. Optimized Design Examples

In order to demonstrate the versatility of the thin composite double-sided planar AMCs, several structures were optimized targeting various surface responses for different incident polarizations at diverse frequencies. The designs include single band and multiple band AMC optimizations, a single pass-band and AMC band designs, a band-selective AMC, an absorber-AMC combination, as well as a double-sided AMC separator targeting Wi-Fi frequencies of 2.4 GHz and 5.2 GHz on opposite sides. The PFEBI simulated magnitude and phase of the scattering coefficients are utilized in different cost functions to achieve the desired results.

The first design example was optimized for a normally incident TE plane wave on the top surface at 10 GHz. A population of 20 chromosomes was evolved for a maximum of 200 iterations. The dimensions of the square unit cell were prescribed to be 1.0 cm by 1.0 cm, with a thickness of 0.9 mm (0.095 λ_r). The permittivity of the dielectric was fixed at $\varepsilon_r = 10.2 - j\ 0.0253$, which corresponds to the commercially available high frequency laminate; Rogers RT/Duroid® 6010 [109]. The metallic geometry of the optimized top and bottom surfaces are illustrated in Figure 5-5 (a) and in Figure 5-5 (b), respectively. To increase the computational accuracy of the

PFEBI solver, each pixel is divided into 4 smaller pixels to obtain a finer meshing resolution. Black colored pixels represent the metallic pixels and gray pixels represent the absence of metal where the dielectric is exposed.

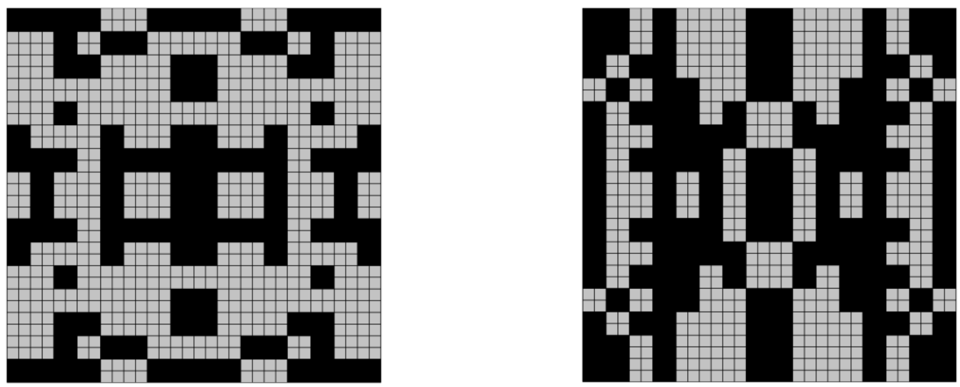

(a) (b)

Figure 5-5: GA optimized pixelized square unit cell geometries for a thin AMC structure at 10 GHz. Top FSS geometry is shown in (a), and bottom FSS geometry is shown in (b). Black pixels represent the metallic patches and gray pixels represent the absence of metallic patches where the dielectric is exposed.

In Figure 5-6, S_{11} represents the reflection from top surface of the composite structure. For the geometry in Figure 5-5, $\angle S_{11}$ passes through zero at 10 GHz, hence the top surface of the metamaterial behaves as AMC at this frequency. At 10 GHz, $|S_{11}|$ is -0.527 dB and $|S_{21}|$ is -13.68 dB, respectively. On the other side of the structure, the phase and the magnitude of the S_{22} are 177° and -0.19 dB, respectively. This demonstrates that the bottom face of the metamaterial behaves as an AEC ground plane without requiring complete metallic backing.

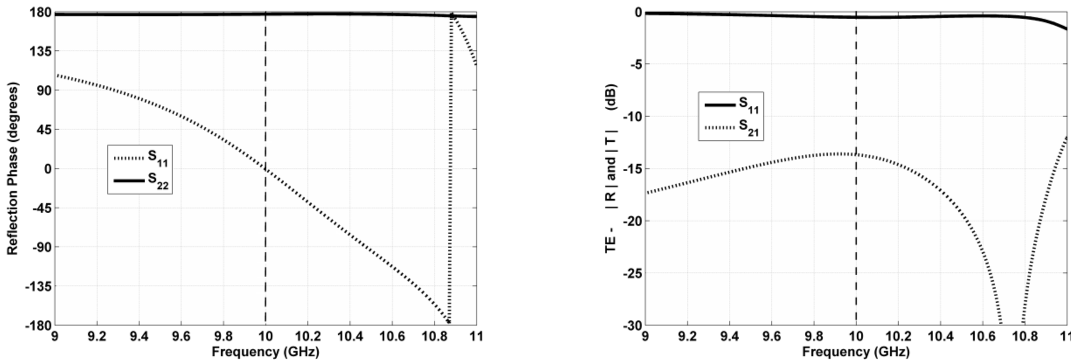

(a) (b)

Figure 5-6: (a) TE reflection phase from the top and bottom surfaces, (b) reflection and transmission magnitudes.

In order to demonstrate the flexibility of the optimization procedure and the proposed design methodology, a second optimization is carried out for a TM polarized, normally incident wave with a surface reflection phase response of 90 degrees and high reflection magnitude. It has been shown in [111]-[112] that this phase response provides the best input impedance match for low profile antennas. A population of 10 chromosomes was evolved for maximum of 300 iterations. The dimensions of the square unit cell were fixed to 1.0 cm by 1.0 cm with a thickness of 1.05 mm (0.11 λ_r). The permittivity of the dielectric was again set to ε_r = 10.2 - j0.0253. The cost function used for this optimization is

$$Cost = \left| 1 - R_{Top}^{10GHz} \right| , \tag{5-2}$$

where the surface reflection response is targeted to be $R_{Top} = j$. The optimized FSS geometries of the top and bottom surfaces are illustrated in Figure 5-7 (a) and in Figure 5-7 (b), respectively. The phase of S_{11} is 90° at 10.04 GHz and $|S_{11}|$ at 10.04 GHz is -0.41 dB as seen in Figure 5-8. The transmission magnitude, $|S_{21}|$, is -13.93 dB. The phase and the magnitude of the S_{22} are 171.5° and -0.19 dB, respectively. The bottom surface of the metamaterial behaves as a AEC while the top surface is optimized for the desired response.

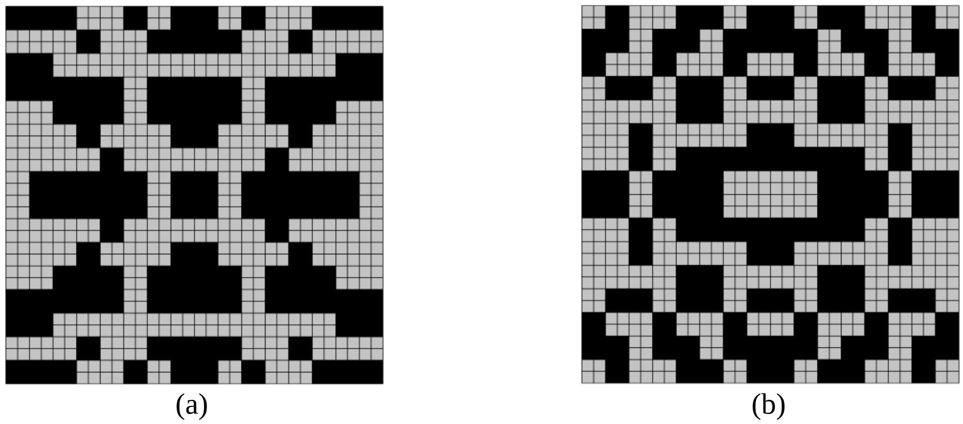

Figure 5-7: GA optimized pixelized square unit cell geometries for the second design optimization. Top FSS geometry is shown in (a), and bottom FSS geometry is shown in (b). Black pixels represent the metallic patches and gray pixels represent the absence of metallic patches where the dielectric is exposed.

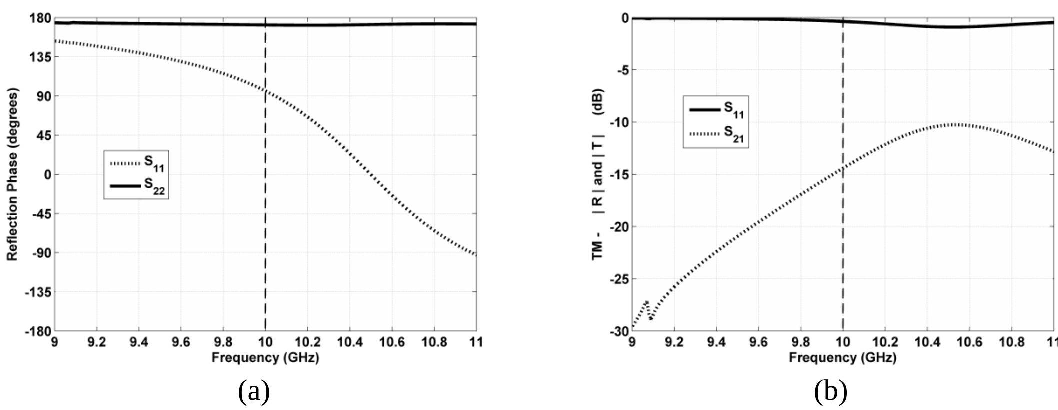

Figure 5-8: (a) TM reflection phase from the top and bottom surfaces, (b) reflection and transmission magnitudes.

The third design is carried out for a TM polarized, normally incident wave and is optimized for dual-band AMC conditions from the top surface at frequencies of 10.0 GHz, and 14.0 GHz. The cost function used for this optimization is

$$Cost = \left|1 - R_{Top}^{10.0GHz}\right| + \left|1 - R_{Top}^{14.0GHz}\right| \tag{5-3}$$

A population of 15 chromosomes was evolved for a maximum of 300 iterations. The dimensions of the square unit cell were set to 0.67 cm by 0.67 cm, with a thickness of 1.8 mm

(0.2683 λ_r at 14 GHz). The same dielectric with permittivity $\varepsilon_r = 10.2 - j0.0253$ was used for this design. The FSS geometries of the top and bottom surfaces are illustrated in Figure 5-9 (a) and Figure 5-9 (b), respectively. The phase of S_{11} passes through the zero at 10.06 GHz, and 13.90 GHz, hence the top surface exhibits dual band AMC response as seen in Figure 5-10. The magnitude of the S_{11} at 10.06 GHz is -1.00 dB and S_{21} is -15.25 dB, respectively. The magnitude of S_{11} at 13.90 GHz is -0.78 dB and S_{21} is -13.16 dB, respectively. The phase and the magnitude of S_{22} at 10.06 GHz are 177° and -0.14 dB, respectively. The phase and magnitude of S_{22} at 13.90 GHz are 175° and -0.22 dB, respectively. This demonstrates that the bottom face of the metamaterial behaves as a AEC ground plane at both target frequencies of 10 GHz and 14 GHz.

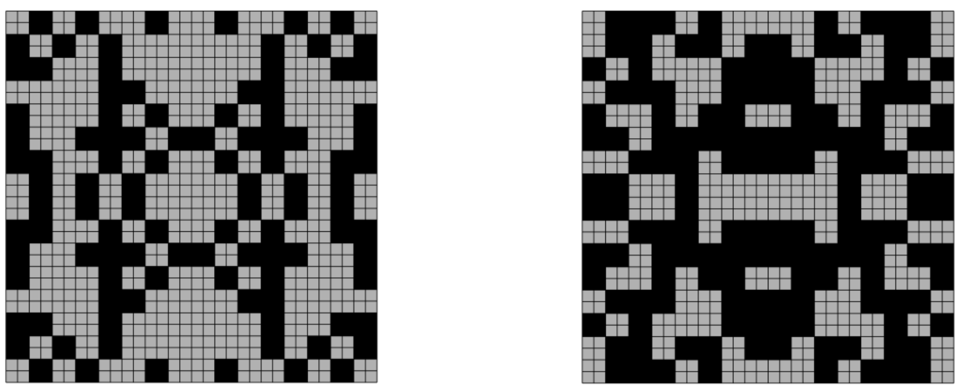

(a) (b)

Figure 5-9: GA optimized pixelized square unitcell geometries for a thin AMC structure at 10 GHz. Top FSS geometry is shown in (a), and bottom FSS geometry is shown in (b). Black pixels represent the metallic patches and gray pixels represent the absence of metallic patches where the dielectric is exposed

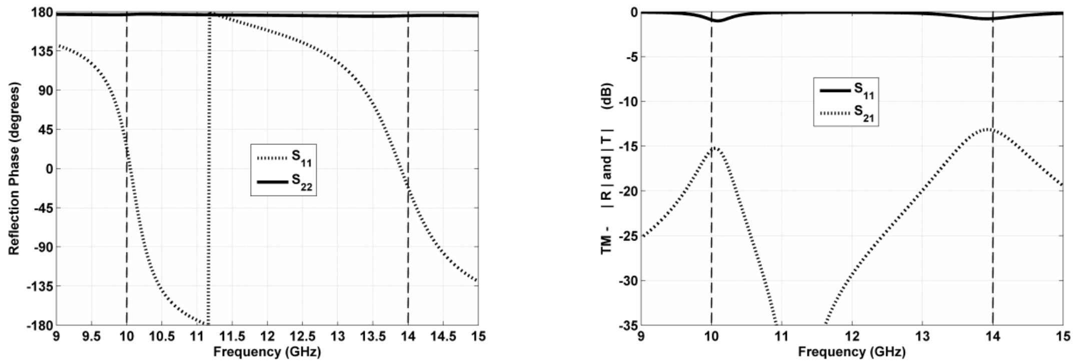

(a) (b)

Figure 5-10: (a) TM reflection phase from the top and bottom surfaces, (b) reflection and transmission magnitudes.

The fourth design example is carried out for a TE polarized, normally incident wave and optimized at two different frequencies, 8.0 GHz and 10.0 GHz. At 10.0 GHz, the design is optimized for an AMC response from top surface, and at 8.0 GHz it is optimized for low reflection, *i.e.* high transmission. The cost function to be minimized for this optimization is

$$Cost = \left| R_{Top}^{8.0GHz} \right| + 6 \times \left| 1 - R_{Top}^{10.0GHz} \right| \tag{5-4}$$

A population of 50 chromosomes was evolved for maximum of 200 iterations. The dimensions of the square unit cell were set to 1.0 cm by 1.0 cm, with a thickness of 0.9 mm (0.095 λ_r at 10 GHz). The permittivity of the dielectric was set to ε_r = 10.2 - j0.0253. The optimized FSS geometries of the top and bottom surfaces are illustrated in Figure 5-11 (a) and Figure 5-11 (b), respectively. After the optimization is completed, a fine frequency sweep is carried out. The reflection phase response from the top surface is computed via both PFEBI and Ansoft HFSS [108] and shown in Figure 5-12 (a). Except for a small frequency shift, both simulations agree very well. The small frequency shift can be explained by the different meshing techniques utilized by the two different solvers. The AMC band is achieved at 10 GHz as seen in Figure 5-12 (a), whereas at 8.0 GHz the structure allows high transmission. In Figure 5-12 (b), $|S_{11}|$ at 8.0 GHz is -18 dB and $|S_{21}|$ is -0.28 dB, respectively. At 10 GHz, $|S_{11}|$ is -0.6 dB and $|S_{21}|$ is -16.67 dB.

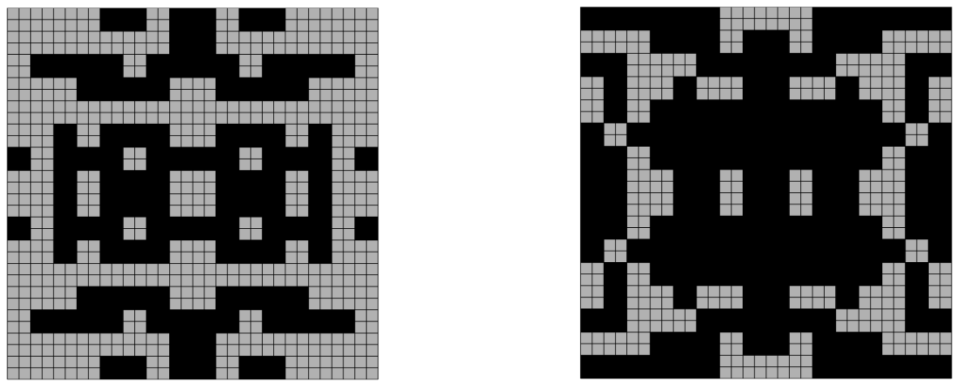

(a) (b)

Figure 5-11: GA optimized pixelized square unit cell geometries for a thin AMC structure for the fourth design example. Top FSS geometry is shown in (a), and bottom FSS geometry is shown in (b). Black pixels represent the metallic patches and gray pixels represent the absence of metallic patches where the dielectric is exposed.

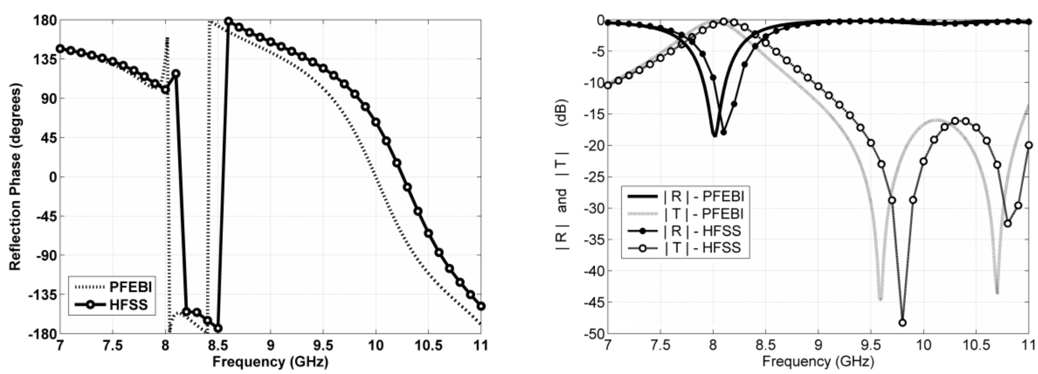

(a) (b)

Figure 5-12 : (a) TE reflection phase from the top surface, (b) reflection and transmission magnitudes.

The fifth design is carried out for a TM polarized, normally incident wave and is optimized for AMC condition at 10 GHz and two pass bands at 9.0 GHz and 11.5 GHz, respectively. This design demonstrates that we can achieve a highly reflective design with AMC condition at one frequency band and optimize the structure to be transparent outside of the band, providing a great deal of flexibility for composite systems. The cost function used for this optimization is

$$Cost = \left|R_{Top}^{9.0GHz}\right| + \left|1 - R_{Top}^{10.0GHz}\right| + \left|R_{Top}^{11.5GHz}\right| \tag{5-5}$$

A population of 10 chromosomes was evolved for a maximum of 300 iterations. The dimensions of the square unit cell were set to 1.035 cm by 1.035 cm with a thickness of 0.9 mm (0.095 λ_r). A permittivity of ε_r = 10.2 - *j*0.0253 was again used for the substrate. The FSS geometries of the top and bottom surfaces are illustrated in Figure 5-13 (a) and Figure 5-13 (b), respectively. At 9.94 GHz, $\angle S_{11}$ passes through zero and $|S_{11}|$ is -1.75 dB, hence the top surface of the metamaterial behaves as an AMC.

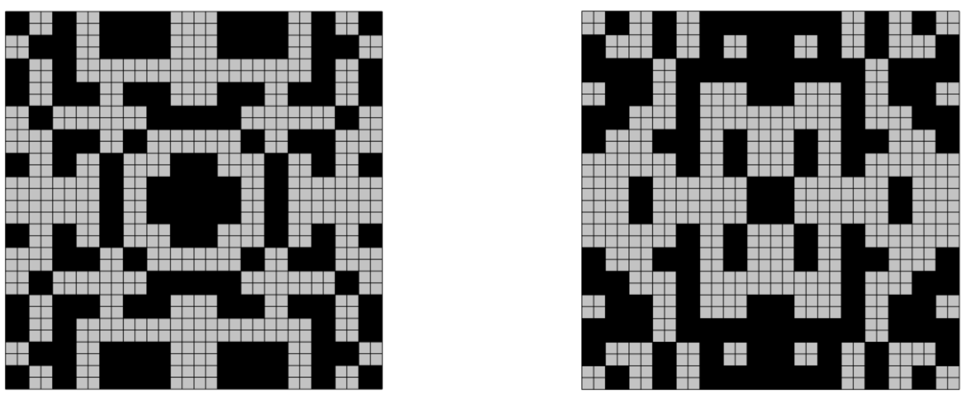

(a) (b)

Figure 5-13: GA optimized pixelized square unit cell geometries for a thin bandstop AMC structure at 10 GHz. Top FSS geometry is shown in (a), and bottom FSS geometry is shown in (b). Black pixels represent the metallic patches and gray pixels represent the absence of metallic patches where the dielectric is exposed.

On the other hand, $\angle S_{22}$ and $|S_{22}|$ are 160° and -0.16 dB, respectively, demonstrating that the bottom face of the metamaterial behaves as an AEC ground plane at around 10 GHz. As seen in Figure 5-14 (b), the pass-band frequencies are 9.0 GHz with $|S_{11}|$ of -16.3 dB and $|S_{21}|$ of -0.5 dB and 11.5 GHz with $|S_{11}|$ of -12.1dB and $|S_{21}|$ of -0.4 dB.

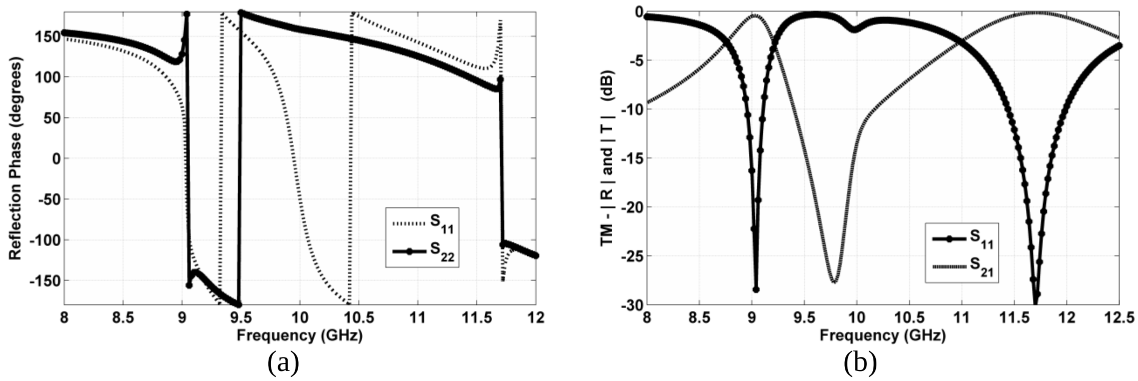

Figure 5-14: (a) TM reflection phase from the top and bottom surfaces, (b) reflection and transmission magnitudes.

The flexibility and versatility of the proposed synthesis method can be easily seen from the previous examples, where double-sided AMC structures are optimized for AMC behavior at single or multiple frequencies. Spatial filters are also possible, where pass bands can be designed at certain frequencies along with AMC bands, offering a great deal of flexibility for composite systems. The synthesis procedure can also be applied to absorber synthesis as well, requiring only small modifications to the structure. The previous two-layered designs assumed perfectly conducting metal, however, they can be modified to include lossy surface sheets instead or additionally, the structure can be extended to three FSS layers depending on the targeted surface response. In this sixth design example, again a two FSS structure is optimized, where the PEC patches of the top FSS is replaced with impedance patches which have a value optimized by the

GA. The absorption magnitude of the top surface is computed using the scattering parameters computed by the PFEBI through

$$|A| = 1 - \left|R_{Top}^{10.0GHz}\right|^2 - \left|T_{Top}^{10.0GHz}\right|^2 \qquad (5\text{-}6)$$

The optimization is carried out for a TM polarized, normally incident wave and the top FSS is optimized for high absorption at 10 GHz. The cost function to be minimized is defined as

$$Cost = \left|R_{Top}^{10.0\,GHz}\right| + \left|T_{Top}^{10.0\,GHz}\right| \qquad (5\text{-}7)$$

A population of 20 chromosomes was evolved for a maximum of 300 iterations. The dimensions of the square unit cell were preset to 1.0 cm by 1.0 cm with a thickness of 1.8 mm (0.19 λ_r). The impedance of the top FSS patches and the complex dielectric substrate permittivity were also optimized. The optimized top FSS has a surface impedance of 105.27 Ω and permittivity of ε_r = 11.87 - j0.117 where as the bottom FSS is preset to be PEC.

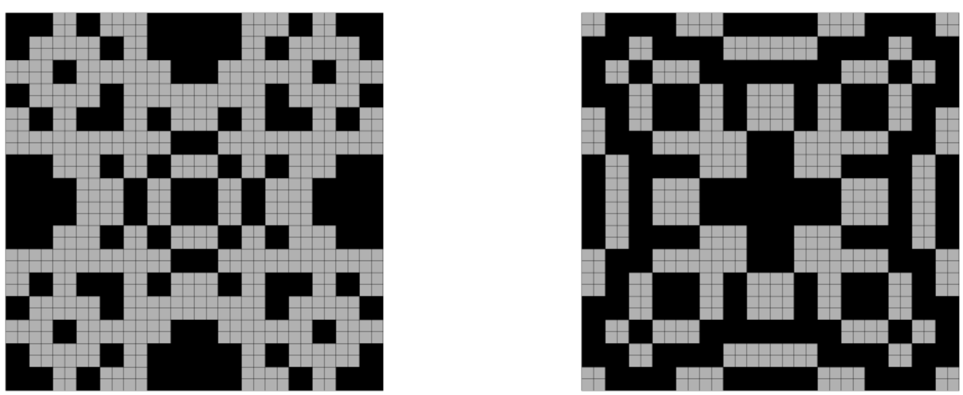

(a) (b)

Figure 5-15: GA optimized pixelized square unit cell geometries for a absorber structure at 10 GHz. (a) Top FSS geometry is shown, where black pixels represent the impedance patches and gray pixels represent the absence of the impedance patches. (b) Bottom FSS geometry is shown, where black pixels represent the metallic PEC patches and gray pixels represent the absence of metallic PEC patches where the dielectric is exposed.

The FSS geometries of the top and bottom surfaces are illustrated in Figure 5-15 (a) and in Figure 5-15 (b), respectively. To achieve polarization insensitivity, eight-folded symmetry is applied to the unit cells rather than four-folded symmetry. The scattering parameters for the design in Figure 5-15 are shown in Figure 5-16. At 10.0 GHz, $|S_{11}|$ is -25.10 dB and $|S_{21}|$ is -17.43 dB as seen in Figure 5-16 (a). For the bottom surface shown in Figure 5-16 (b), $|S_{22}|$ and $\angle S_{22}$ is -0.154 dB and 175.9° at 10.0 GHz. This provides a design with a highly absorptive top surface at 10 GHz and a bottom surface that behaves as an AEC without requiring a complete metallic back plane.

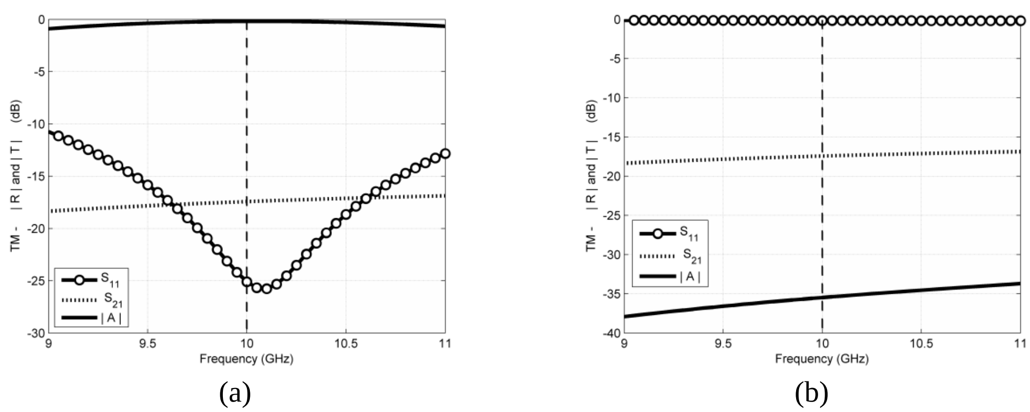

Figure 5-16: (a) TM surface response from the top surfaces; reflection, transmission and absorption magnitudes. (b) TM surface response from the bottom surfaces; reflection, transmission and absorption magnitudes.

The last design example uses three FSSs layers, where the top FSS again uses impedance patches; the middle and bottom FSS screens are PEC as seen in Figure 5-18. The optimization is carried out with a TM polarized wave at 10 GHz, where the top surface response is optimized for high absorption and the bottom surface response is optimized for an AMC. The cost function

$$Cost = \left| R_{Top}^{10.0\,GHz} \right| + \left| T_{Top}^{10.0\,GHz} \right| + \left| 1 - R_{Bottom}^{10.0\,GHz} \right| , \tag{5-8}$$

is used to achieve these goals. A population of 40 chromosomes was evolved for maximum of 500 iterations. Again, to achieve polarization insensitivity for absorber applications, eight-folded unit cell symmetry is used. The dimensions of the square unit cell were set to 1.0 cm by 1.0 cm with a thickness of 2.4 mm (0.259 λ_r), where the middle FSS is placed at the exact center of the dielectric, *i.e.*1.2 mm away from either surface. The optimized permittivity of the dielectric is ε_r = 10.496, and the optimized surface impedance for the impedance patches is 649.32 Ω. At 10 GHz, $|S_{11}|$ is -31.6 dB and $|S_{21}|$ is -22.4 dB, respectively. On the other side, $|S_{22}|$ and ∠S22 are 0.24° and -0.073 dB, respectively. This demonstrates that the bottom face of the metamaterial behaves as a AMC ground plane at 10 GHz while the top surface is highly absorptive.

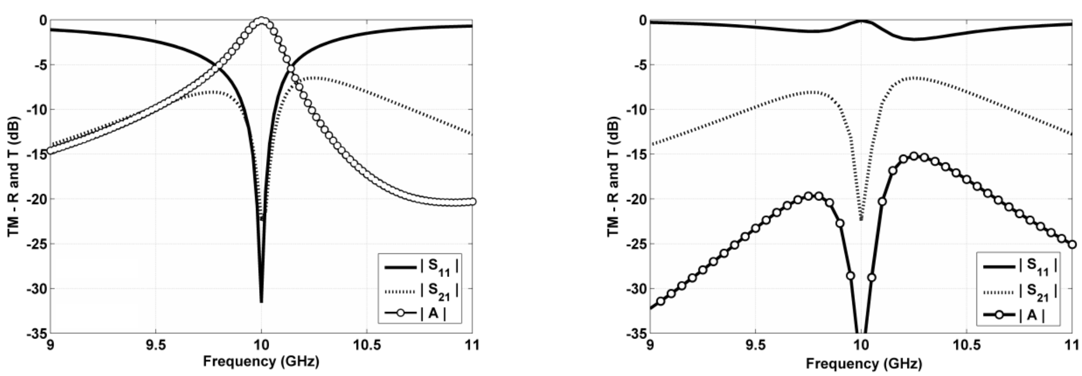

(a) (b)

Figure 5-17: (a) TM surface response from the top surfaces; reflection, transmission and absorption magnitudes. (b) TM surface response from the bottom surfaces; reflection, transmission and absorption magnitudes

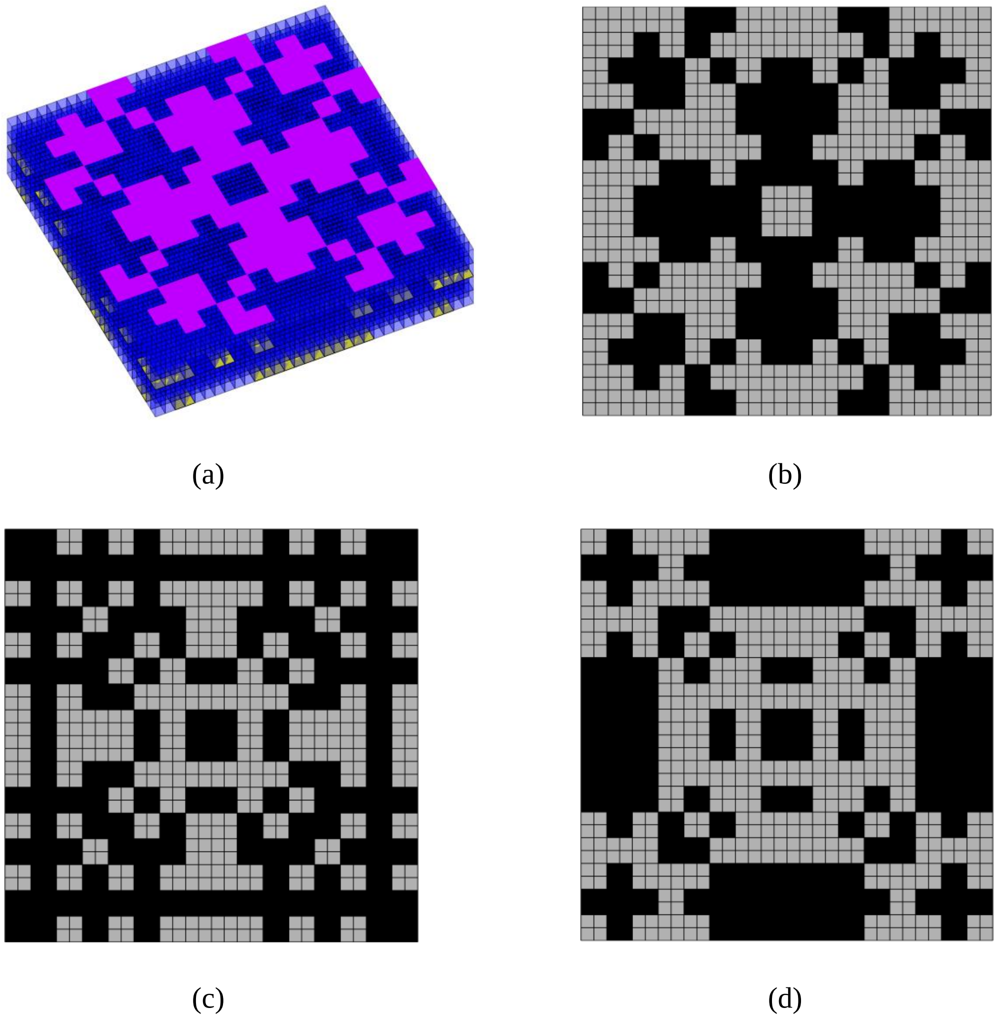

Figure 5-18: (a) Perspective view of the GA optimized square unit cell, where purple color represent the impedance surfaces, yellow represents the PEC surfaces and blue represent the absence of any metal where the dielectric material is exposed. (b) Top FSS geometry is shown, where black pixels represent the impedance patches and gray pixels represent the absence of the impedance patches. (c) Middle FSS geometry and (d) bottom FSS geometries are shown, where black pixels represent the PEC patches and gray pixels represent the absence of PEC patches where the dielectric is exposed.

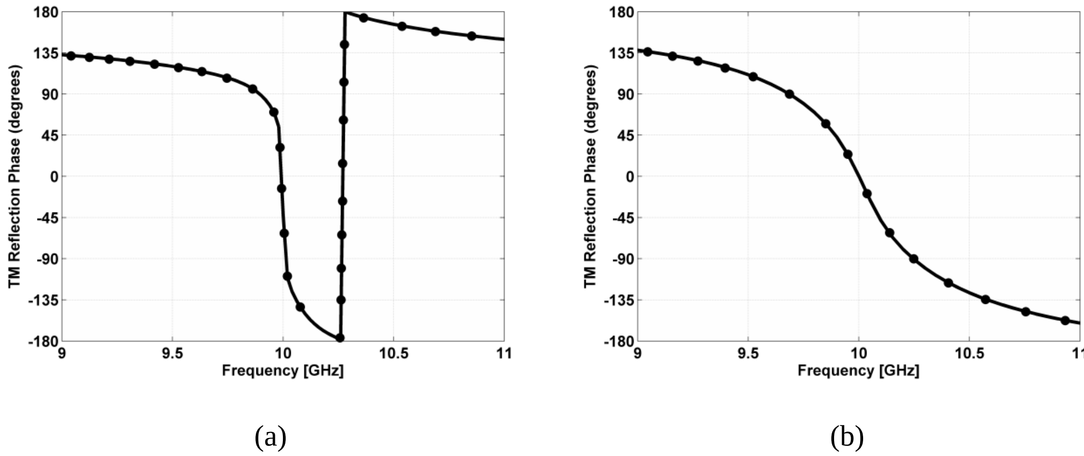

Figure 5-19: TM reflection phase from the top, shown in (a) and bottom surfaces shown in (b).

5.6. Application at Wi-Fi Frequencies

Customer demand in wireless communication devices has been toward compactness, multifunctionality, throughput, and a better user experience which commonly leads to development of new wideband and multiband communication devices. Multiple-input multiple-output (MIMO) antenna systems are one such technology that utilize multiple antennas and sophisticated communication protocols to achieve higher data rates and reduced interference [1]. Problems with multiple antenna devices arise from mutual coupling between tightly packed radiating elements. For reduced mutual coupling, antennas are typically spaced at a minimum of $\lambda/2$ apart [10], however, in compact devices with a small footprint, such separation may not be feasible.

To allow reduced spacing between two monopole antennas without performance degradation through mutual coupling, a thin double-sided artificial magnetic conducting surface is placed in between the antennas. DSAMC separator is optimized via the genetic algorithm and

PFEBI solver as with the previous designs. For realistic applications, the surface is likely not infinite in extent as is assumed with PFEBI. Hence, a finite dimension AMC separator is also simulated with two commercial finite element simulation tools after the GA optimization was completed. Here, Ansoft HFSS and CST Microwave Studio [113] are used with the monopoles included to confirm the results with finite length DSAMC separator. Design goals for the optimization of DSAMC include a highly reflective composite structure with AMC behavior at two different frequencies such that two antennas of diverse frequency can efficiently operate on either side of the separator and can be packed into smaller footprint. In this design example, the thin DSAMC separator is designed for use at the typical Wi-Fi bands of f_1 = 2.4 GHz and f_2 = 5.2 GHz. A 0.254cm-thick substrate of commercially available Rogers RT/Duroid® 6010 [109] is used, which has a relative permittivity of ε_r = 10.2 - j0.0253. The four-folded symmetric unit cell is optimized for a TE polarized, normally incident wave and the cost function to be minimized for this optimization is

$$Cost = \left| 1 - R_{Top}^{2.4GHz} \right| + \left| 1 - R_{Bottom}^{5.2GHz} \right| . \tag{5-9}$$

A population of 25 chromosomes was evolved over a maximum of 500 iterations. The dimensions of the square unit cell were fixed at 1.18 cm on a side. The optimized FSS geometries of the top and bottom surfaces are illustrated in Figure 5-20 (a) and Figure 5-20 (b), respectively. After optimization, a fine frequency sweep of the doubly periodic structure is carried out in HFSS and CST and displayed in Figure 5-21 (a), where excellent agreement can be observed between two simulations. While the top surface provides near zero phase at 2.4 GHz, the bottom surface reflection phase response is 45 degrees at 5.2 GHz, which is still in the working bandwidth of an AMC response (± 90°).

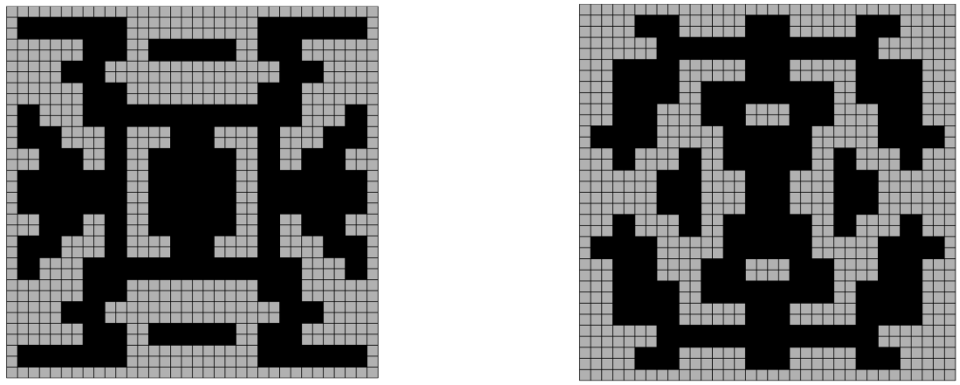

(a) (b)

Figure 5-20: GA optimized pixelized square unitcell geometries for a thin AMC structure. Top FSS geometry is shown in (a), and bottom FSS geometry is shown in (b). Black pixels represent the metallic patches and gray pixels represent the absence of metallic patches where the dielectric is exposed.

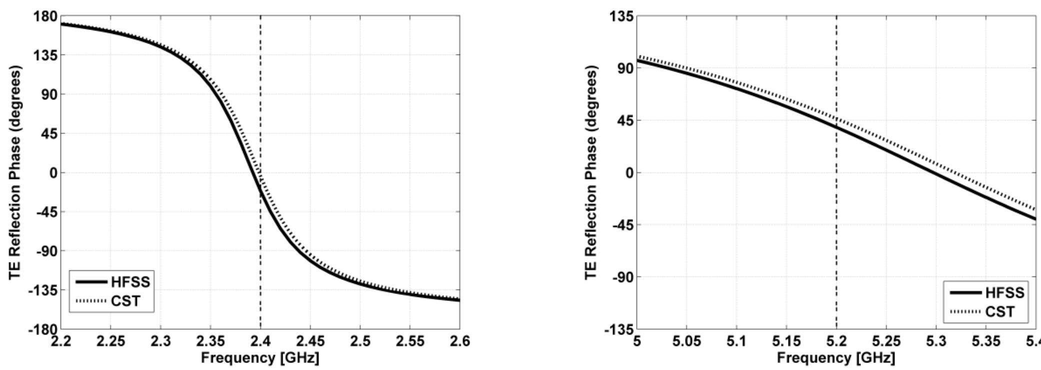

(a) (b)

Figure 5-21: (a) TE reflection phase from the top for f_1 = 2.4 GHz and (b) bottom surfaces f_2 = 5.2 GHz. Excellent agreement can be seen between HFSS and CST.

To confirm functionality of this design as a practical DSAMC separator, a 6 by 6 unit cell section of the material was placed halfway between a 2.4 GHz monopole and a 5.2 GHz monopole. The total size of the slab is 7.08 cm by 7.08 cm with a thickness of 0.252 cm. Each monopole is placed 5 mm away from their respective surfaces which constitutes a total of 12.52 mm separation between two monopoles as illustrated in Figure 5-22. This total distance is 0.10 λ_0 at f_1 and 0.217 λ_0 at f_2 which would lead to considerable coupling between the two antennas without any separator between them.

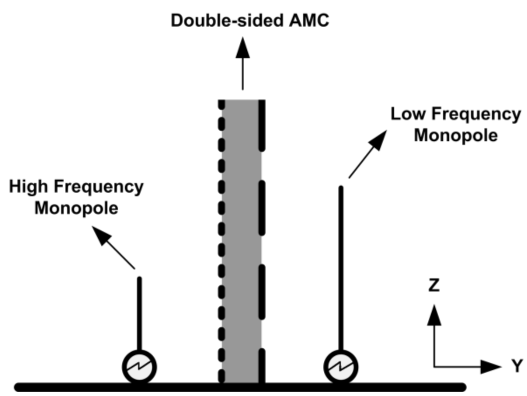

Figure 5-22: Cross-sectional diagram illustration of the double-sided AMC structure with two monopoles operating at diverse frequencies of f_1 and f_2 , where the face of the DSAMC is optimized for frequency f_1 and the other face is optimized for frequency f_2. Simulations are carried out in HFSS and CST.

A metal (PEC) separator can be placed in between the two monopole antennas to reduce the coupling, however, this also leads to poor input efficiencies as is illustrated with the black curves in Figure 5-23. On the other hand, inserting the optimized DSAMC separator allows tightly packing of the antennas with good isolation. The return loss and isolation of antennas are illustrated in Figure 5-23 (a) for the lower frequency band and Figure 5-24 (b) for upper frequency band. CST and HFSS simulations are in excellent agreement and the DSAMC separator provides good isolation and good return loss at the targeted Wi-Fi frequencies.

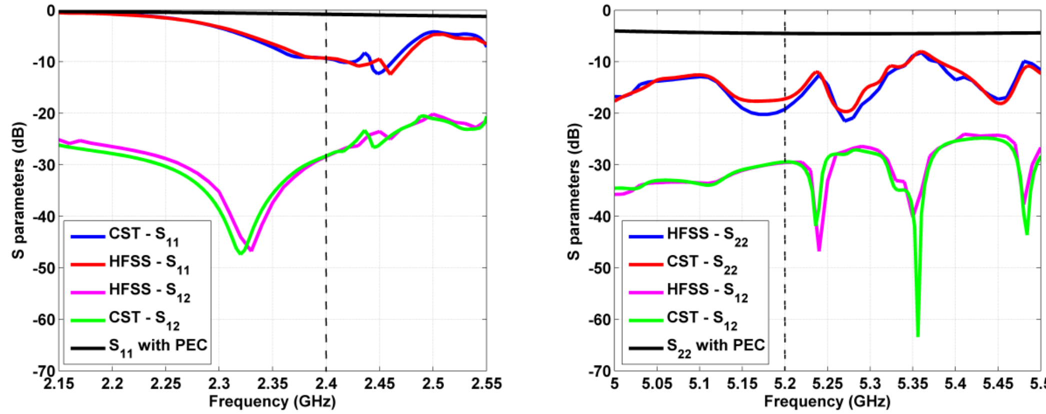

(a) (b)

Figure 5-23: Antenna performance and coupling for the low frequency band (a) and high frequency band of operation (b). S_{11} denotes the monopole performance at the low frequency f_1 = 2.4 GHz, and S_{22} denotes the monopole performance at the higher frequency f_2 = 5.2 GHz. The black curve demonstrates poor performance for both antennas when the PEC separator is used

Figure 5-24 illustrates the YZ plane cut of the radiation patterns of the individual monopoles when they are 5 mm away from their respective surfaces. For both antennas, highest gain is directed away from DSAMC separator and due to finite ground plane, the main beam is not directed at the horizon. The gain at respective frequencies is 4.8 dB for the low frequency monopole and 8.7 dB for the high frequency monopole.

5.7. Summary

A new design methodology has been presented for the synthesis of thin planar realizations of volumetric artificial magnetic conducting (AMC) surfaces. The composite materials are generated through optimization of two or three different metallic frequency selective surface (FSS) structures printed on either side, and optionally inside of, a thin dielectric substrate.

This type of realization eliminates the need for a complete PEC back plane and through optimization of these thin composite structures, it is possible to synthesize thin volumetric AMC planes for different polarizations, different surface responses, and also either single or multi-frequency of operation with thicknesses as small as $\lambda_r/10$. Such designs can also be tailored to absorber applications by simultaneously optimizing the FSS geometry and surface impedance of one surface and the PEC FSS of the opposite surface to provide a slab with absorber behavior on one side and AMC behavior on the other. A system example is also presented which illustrates the versatility of the double-sided AMC design as a separator to reduce the coupling between two monopole antennas operating at the Wi-Fi frequencies of 2.4 GHz and 5.2 GHz.

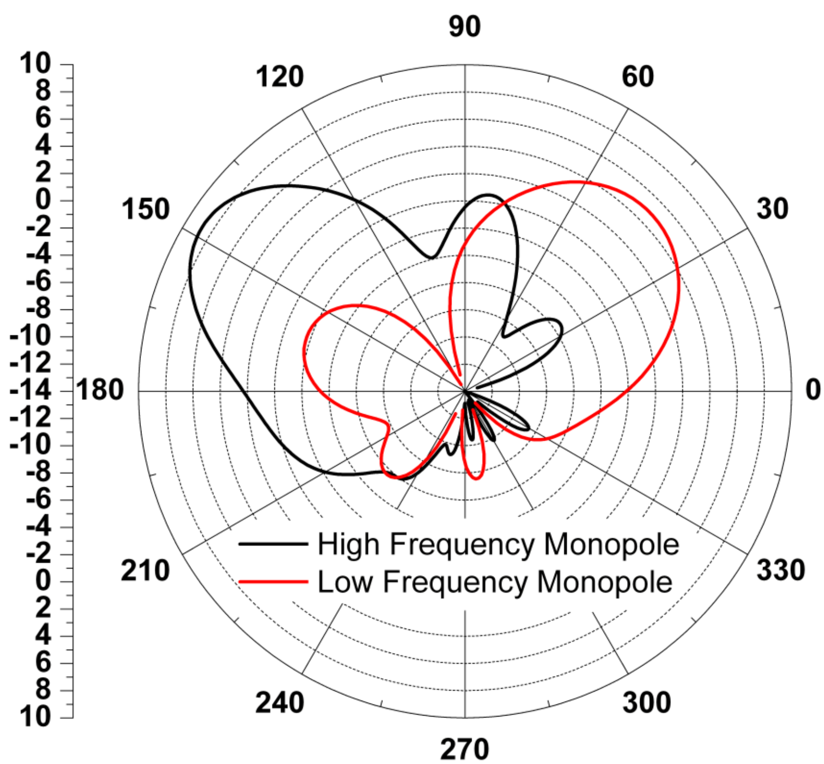

Figure 5-24: Gain plots of the individual monopoles operating at 2.4 GHz (red) and 5.2 GHz (black). Radiation is highest in the YZ plane as shown in Figure 5-22, with each antenna having highest gain away from its respective surfaces.

Chapter 6

Matched Impedance Thin Planar Composite Magneto-Dielectric Metasurfaces

6.1. Introduction

The advantages and disadvantages of applying high permittivity dielectric loading to electromagnetic devices such as in the miniaturization of patch antennas are well known [110]. Sometimes overlooked, however, is the same effect utilizing magnetic loading [114] or using magneto-dielectric materials. A low-loss material with both magnetic ($\mu_r > 1$) and dielectric ($\varepsilon_r > 1$) properties would enable the design of more advanced microwave devices and miniaturized antenna systems. Such materials could potentially be used as substrates for miniaturized planar antennas while maintaining a relatively high bandwidth and broadside gain. Unfortunately, most naturally occurring homogenous magnetic materials exhibit large losses that render them unusable at high frequencies beyond 500 MHz [115], hence engineered magnetic and magneto-dielectric materials have to be designed as composite structures. There have been a variety of efforts to realize magnetic materials as substrates for miniaturized patch antennas by combining metallic inclusions into non-magnetic substrates [116] - [118] which behave as embedded LC resonator circuit elements. As an alternative to embedded metallic inclusions, Namin *et al.* [119] recently suggested using alternating thin ferromagnetic films and polymer layers as composites for realizing substrates with identical relative permittivity and permeability. This technique was employed in [119] to design significantly miniaturized broadband stacked-patch antennas for the L-band. Kern *et al.* [12] proposed a design approach for composite magnetic metamaterial coatings, called metaferrites, which can be engineered to provide magnetic properties ($\mu_r > 1$, $\varepsilon_r =$

1) that are usable at frequencies beyond 1 GHz, where conventional magnetic materials tend to suffer from high losses and/or weaker response. In [12], it was demonstrated that the properties of a PEC backed homogenous magnetic slab with frequency dependent permeability could effectively be achieved using a properly designed high-impedance Electromagnetic Bandgap (EBG) structure. Unlike designs with embedded circuit element inclusions such as split-ring resonators, their planar configuration is relatively simple and only requires that a Frequency Selective Surface (FSS) type structure be printed on top of a thin PEC backed dielectric substrate. It was also demonstrated that the real and imaginary parts of the effective permeability of an equivalent homogeneous magnetic slab could be related to the surface impedance values of the composite EBG structure.

Electromagnetic absorbers represent another equally important area that can benefit from using magneto-dielectric metamaterials, with applications ranging from reducing the radar cross section of large objects [3] to reducing the reflected energy inside of anechoic chambers [4]. In many practical applications, electromagnetic absorbers are required to cover curved surfaces of large objects, where the thickness of the absorber as well as the electrically small feature size of the metamaterial structure become very important design considerations. Kern *et al.* [67] demonstrated a novel design synthesis methodology that employs a Genetic Algorithm (GA) with the ability to optimize the subwavelength unit cell geometry of a metamaterial to achieve a desired response at a targeted operating frequency or set of frequencies. This robust GA optimization technique was utilized in [67] to synthesize ultra-thin metamaterial absorbers based on lossy EBG surfaces and in [14] to design multiband Artificial Magnetic Conducting (AMC) surfaces by manipulating the electromagnetic properties of high-impedance FSS. Moreover, it has been shown in [12] that a similar GA optimization procedure can be used to synthesize lossy metaferrites for electromagnetic absorber applications.

In this chapter, a new design technique is introduced for creating matched impedance ($\mu_r = \varepsilon_r > 1$) magneto-dielectric metamaterial slabs. The technique is based on using a GA [5] to optimize thin planar metallo-dielectric metasurfaces comprised of a periodic array of electrically small and rotationally symmetric unit cell structures sandwiched between two different dielectric slabs, one of which is backed by a perfectly conducting ground plane. The ability to optimize the design parameters of these thin planar composite metallo-dielectric structures allows for the synthesis of low-loss matched-impedance magneto-dielectric metamaterials for planar antenna miniaturization and high-loss matched-impedance magneto-dielectric metamaterials for absorber applications. Moreover, these composite metallo-dielectric structures allow for the design of planar low-loss double-negative substrates as an alternative to volumetric split-ring resonators [115], [121].

6.2. Theoretical Development of Matched-Impedance Composite Magneto-Dielectrics

The design of the Matched Impedance ($\mu_r = \varepsilon_r > 1$) Magneto-Dielectric Metamaterial (MIMDM) consists of a metallic frequency selective surface (FSS) screen with electrically small unit cells sandwiched between two layers of different dielectric materials, one of which is backed by a PEC ground plane as illustrated on the left in Figure 6-1. The upper dielectric has a thickness of t_1 and relative permittivity of ε_1 and the lower layer has a thickness t_2 and relative permittivity of ε_2. The equivalent of this metallo-dielectric structure is a PEC backed homogenous impedance matched magneto-dielectric slab with thickness of $d = t_1 + t_2$ as illustrated on the right of Figure 6-1.

The properties of a PEC backed matched impedance homogenous magneto-dielectric slab with frequency dependent constitutive parameters could effectively be achieved by an optimized composite structure as seen on the left in Figure 6-1.

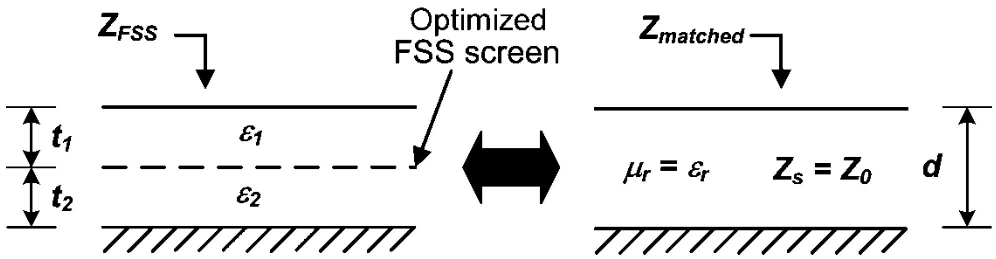

Figure 6-1: Cross-sectional diagram of the PEC backed composite magneto-dielectric metamaterial structure (left) and its equivalent PEC backed homogenous ($\mu_r = \varepsilon_r > 1$) material structure (right).

The surface impedance encountered by a propagating plane wave normally incident upon the composite structure can be expressed as

$$Z_{FSS} = R_{FSS} + j\,X_{FSS}\,, \tag{6-1}$$

where R_{FSS} and X_{FSS} are the respective resistance and reactance of the impedance Z_{FSS}. Moreover, a thin slab of PEC backed homogeneous magneto-dielectric material with thickness d, permeability μ_r (where $\mu_r = \mu'_r - j\mu''_r$) and permittivity ε_r (where $\varepsilon_r = \varepsilon'_r - j\varepsilon''_r$) would have the surface impedance, Z_{in}, as given in [3],

$$Z_{in} = Z_s\ \tanh(j\omega\sqrt{\mu_0\varepsilon_0}\,n_s d), \tag{6-2}$$

where

$$Z_s = Z_0\sqrt{\mu_r / \varepsilon_r} \tag{6-3}$$

Considering the scenario where the slab of PEC backed magneto-dielectric material is matched to free space ($\mu_r = \varepsilon_r$) such that $Z_s = Z_0$, then (6-2) simplifies to

$$Z_{matched} = Z_0\ \tanh(j\beta_0\,n_s d) \tag{6-4}$$

The index of refraction, n_s, for the same scenario, ($\mu_r = \varepsilon_r$), can be given by

$$n_s = \sqrt{\mu_r\,\varepsilon_r} = \sqrt{(\mu'_r - j\mu''_r)(\varepsilon'_r - j\varepsilon''_r)} = \mu_r = \varepsilon_r \tag{6-5}$$

Setting Z_{FSS} equal to $Z_{matched}$ using (6-1) and (6-4), respectively, it follows that

$$\tanh(j\beta_0\, n_s\, d) = Z_{FSS} / Z_0 \tag{6-6}$$

and solving (6-6) for n_s yields

$$n_s = \mu_r = \varepsilon_r = \frac{1}{j\beta_0 d}\tanh^{-1}\left(\frac{Z_{FSS}}{Z_0}\right) \tag{6-7}$$

which suggests that the real and imaginary parts of the complex permeability (or permittivity) can be expressed as

$$\varepsilon_r' = \mu_r' = \mathrm{Re}\left\{\frac{1}{j\beta_0 d}\tanh^{-1}\left(\frac{Z_{FSS}}{Z_0}\right)\right\} \tag{6-8}$$

and

$$\varepsilon_r'' = \mu_r'' = \mathrm{Im}\left\{\frac{1}{j\beta_0 d}\tanh^{-1}\left(\frac{Z_{FSS}}{Z_0}\right)\right\} \tag{6-9}$$

These equations relate the permeability (and permittivity) of the homogeneous magneto-dielectric material to the surface impedance of the composite metamaterial structure. Finally, utilizing (6-1), it is possible to derive independent equations for R_{FSS} and X_{FSS} in terms of the desired permittivity/permeability as shown by

$$R_{FSS} = \frac{Z_0}{2}\frac{\sinh(2x)}{\cosh^2(x) - \sin^2(y)} \tag{6-10}$$

and

$$X_{FSS} = \frac{Z_0}{2}\frac{\sin(2y)}{\cosh^2(x) - \sin^2(y)} \tag{6-11}$$

where $x = \beta_0\, d\, \mu_r''$, $y = \beta_0\, d\, \mu_r'$, $\mu_r' = \varepsilon_r'$ and $\mu_r'' = \varepsilon_r''$.

A binary GA design strategy is employed to optimize the various parameters of the composite metamaterial structure that provides the targeted surface impedance response based on (6-10) and (6-11) as well as the desired effective medium properties. The optimized design parameters include the complex dielectric permittivities (ε_1 and ε_2) of each layer, their corresponding thicknesses (t_1 and t_2), the pixelized geometry and the dimensions of the FSS unit cell.

6.3. Genetic Algorithm Optimization Schema

The GA is utilized for the synthesis of the MIMDM structures targeting various effective material parameters. The GA is well suited for both discrete-valued and real-valued parameterization in the design synthesis of the composite magneto-dielectric structures. It is used to search for the appropriate dielectric material thicknesses, dielectric constants and loss tangents, the FSS geometry and unit cell size that yield the required values for R_{FSS} and X_{FSS}. For fast numerical analysis of the composite structures, the GA is linked with a full-wave Periodic Method of Moments (PMM) code which employs layered media Green's functions, periodic boundary conditions based on Floquet's theorem, and rooftop basis functions [122].

Candidate solutions generated by the GA are evaluated by the PMM code and scattering coefficients are returned for the cost computations. A simple cost function of

$$Cost = \sum_{i=1}^{N}\left[(R_{FSS} - R_{matched})^2 + (X_{FSS} - X_{matched})^2\right], \tag{6-12}$$

is employed over N target frequencies, where R_{FSS} and X_{FSS} represent the surface resistance and surface reactance values of the composite structure, while $R_{matched}$ and $X_{matched}$ represent the real and imaginary parts of the surface impedance associated with the desired homogeneous MIMDM. Once the maximum number of iterations are exhausted or a design with the required values for R_{FSS} and X_{FSS} is found, the optimization terminates. Afterwards, a fine frequency sweep of the final optimized design is performed and validated against the commercially available Ansoft HFSS™ [108].

6.4. Planar Composite Metasurfaces

In the design of MIMDMs, the unit cell consists of a metallic FSS screen with electrically small unit cells sandwiched between two different dielectric layers, one of which is backed by a PEC ground plane. The FSS unit cell is divided in to 32 by 32 pixels and possesses four-fold rotational symmetry which ensures it will have a polarization independent response. Since rotational symmetry is applied, only one quarter of the unit cell is required to be specified by the GA. The crossed arms that pass through the center of the unit cell effectively extend into the neighboring unit cells as depicted in Figure 6-2. When the long arms are properly in alignment with the neighboring unit cells, the effective unit cell size, indicated by the dashed line, can be considerably reduced [123]. This tight packing increases coupling between neighboring cells which can lead to enhanced bandwidth [4].

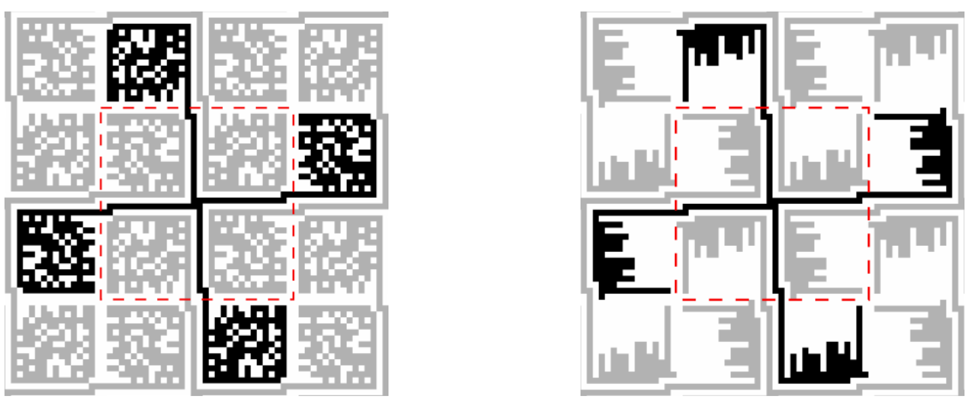

(a) (b)

Figure 6-2: Two different FSS-based metamaterial unit cell geometries. Black and gray shaded regions both represent PEC pixels with two-tones used to distinguish the interconnected structure which spans multiple unit cells. Note that the dashed lines designate the borders of a unit cell.

For the design of Figure 6-2 (a), the unit cell is split into four quadrants and the GA is used to optimize only one quadrant by turning pixels “on” and “off”, where “on” represents the existence of a PEC patch at that location and “off” represents the absence of metal. Each pixel is represented by a single bit in the GA chromosome, which in total requires 143 bits for the FSS geometry alone and an additional 70 bits for the remaining design parameters. Four-fold rotational symmetry is then applied to complete the unit cell geometry. Although this method provides a great deal of flexibility with all design possibilities for the FSS geometry, it can also overwhelm the GA with the proposed chromosome length of 213 bits. A simpler structure is shown in Fig. 3b, where again the GA optimizes only one quadrant but rather than turning on and off pixels, it adjusts the lengths of eleven rows of pixel strips, reducing the FSS geometry portion of the GA chromosome length to 70 bits; another 70 bits is used for the rest of the design parameters, resulting in total chromosome length of 140 bits. Applying symmetry completes the four-fold geometry.

6.5. Optimization Results

In order to demonstrate the versatility of the thin composite MIMDMs, several structures were optimized with different objectives in mind. These designs include low-loss single-band and dual-band magneto-dielectrics with either double-positive or double-negative constitutive parameters. In addition to low-loss designs, these composite structures can be optimized for absorber applications where a certain degree of loss is necessary. Equation (6-10) and (6-11) allows us to compute the required surface impedance values of R_{FSS} and X_{FSS} for an equivalent matched-impedance magneto-dielectric slab with desired constitutive parameters. Then the GA is used to optimize the composite structure in order to obtain the required surface impedance values at the targeted design frequencies.

6.5.1. Synthesis of Low-loss Single-band Magneto-dielectric Metamaterials

The first design example that will be considered was optimized to achieve effective material properties of $\mu_r = \varepsilon_r = 3 - j\,0.005$ at 1.5 GHz. The GA was configured with a population size of 25 chromosomes and was permitted to run for a maximum of 500 iterations using the cost function defined in (6-12). The unit cell geometry evolved by the GA is illustrated in Figure 6-3 (a), while the remaining optimized parameters of the structure are provided in Table 6-1.

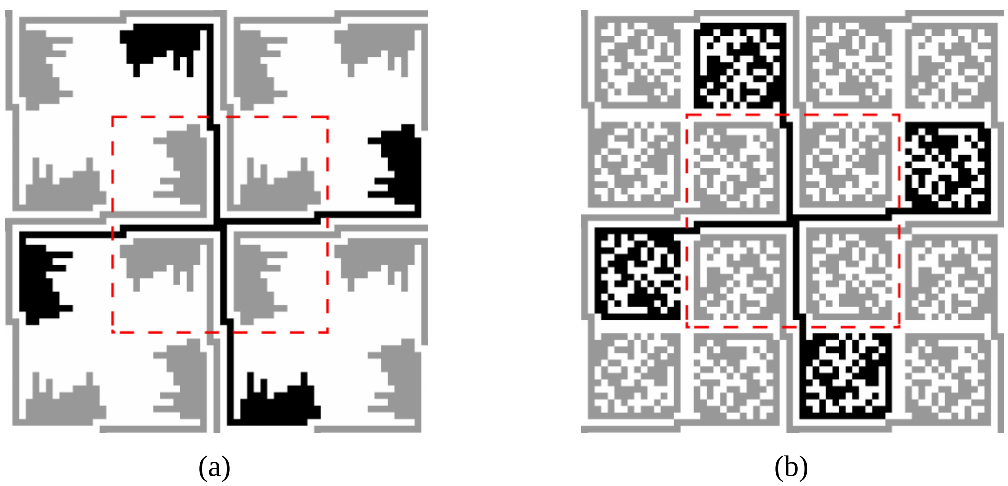

Figure 6-3 : FSS unit cell geometries for the targeted designs of (a) $\mu_r = \varepsilon_r = 3 - j\,0.005$, and (b) of $\mu_r = \varepsilon_r = 4 - j\,0.005$, where black and gray shaded regions represent PEC pixels with two-tones used to distinguish the interconnected structure which spans multiple unit cells. Note that the dashed black lines designate the borders of each unit cell.

Figure 6-4 plots the real and imaginary parts (dashed and solid curves respectively) of the constitutive parameters that are determined by substituting the PMM computed surface impedance values (Z_{FSS}) and the thickness (d) into (6-8) and (6-9). Values of $\mu_r = \varepsilon_r = 2.98 - j$ 0.022 are achieved at the targeted design frequency of 1.5 GHz. The real part of the surface impedance (R_{FSS}) for the optimized composite metamaterial is displayed in Figure 6-5 (a), which was computed via PMM and HFSS.

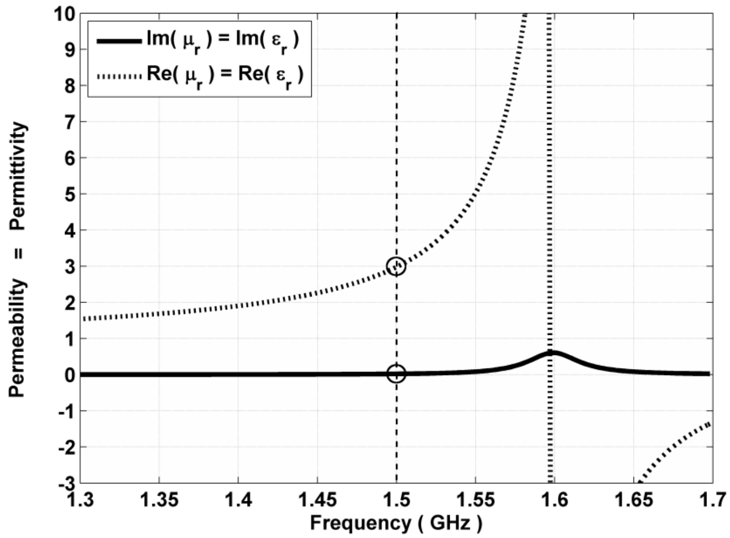

Figure 6-4: Real and imaginary parts of the effective parameters that are computed by substituting the surface impedance values (Z_{FSS}) into (6-8) and (6-9). At the targeted design frequency of 1.5 GHz, values of $\mu_r = \varepsilon_r = 2.98 - j\,0.022$ are achieved.

The two solvers agree very well other than a small frequency shift caused by different meshing strategies employed in the respective solvers. Figure 6-5 (a) also illustrates the HFSS computation of the surface resistance of a homogenous slab with the dispersive constitutive parameters of those shown in Figure 6-4. The dashed line represents the surface resistance of an ideal non-dispersive magneto-dielectric material of the same thickness ($R_{matched}$). The imaginary parts of the surface impedance (X_{FSS}) of the optimized composite metamaterial computed via PMM and HFSS are displayed in Figure 6-5 (b). Similar to the real parts, the shape of the curves agree well, save for a small frequency shift caused by the different meshing strategies employed in each code. Figure 6-5 (b) also illustrates the HFSS computation of the surface reactance of a homogenous slab with the dispersive constitutive parameters of Figure 6-4. The dashed line represents the surface reactance ($X_{matched}$) of an ideal non-dispersive magneto-dielectric material of the same thickness.

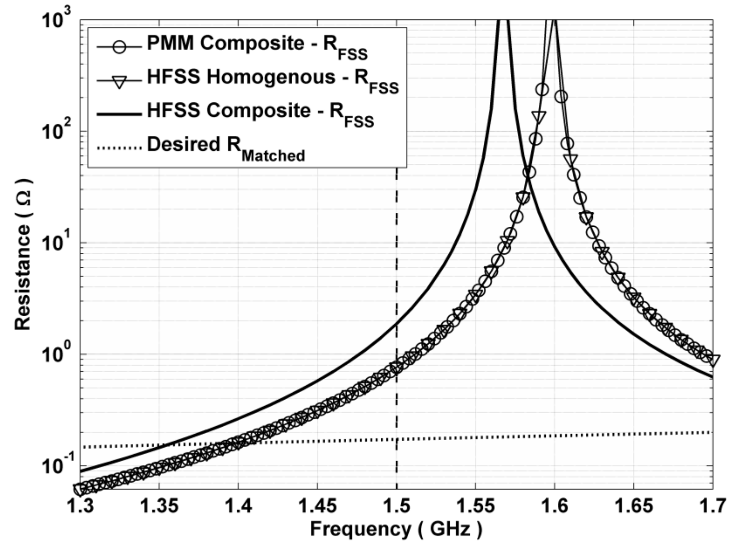

(a)

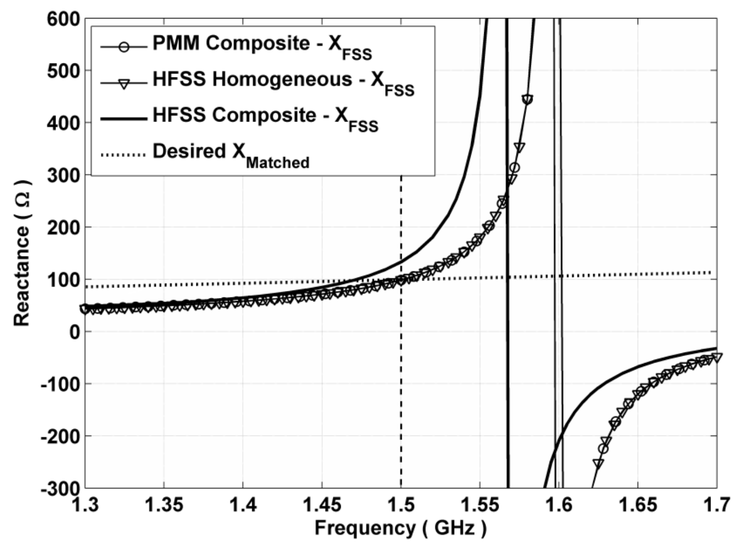

(b)

Figure 6-5: Real (a) and imaginary (b) parts of the surface impedance (Z_{FSS}) of the composite metamaterial targeting $\mu_r = \varepsilon_r = 3 - j\ 0.005$, along with the surface impedance of a homogenous slab with the dispersive constitutive parameter values assigned to it. The dashed lines represent the surface resistance of an ideal non-dispersive magneto-dielectric material with the same thickness.

The second design example was optimized to achieve effective material properties of $\mu_r = \varepsilon_r = 4 - j\ 0.005$ at 1.5 GHz. The GA was configured with a population size of 50 chromosomes for a maximum of 1000 iterations using the cost function given in (6-12). The unit cell geometry of the optimized design is illustrated in Figure 6-3 (b). For this design, the optimized parameter values are also provided in Table 6-1. The real and imaginary parts of the constitutive parameters that were determined by substituting the PMM computed surface impedance values (Z_{FSS}) and the thickness (d) into (6-8) and (6-9) are plotted in Figure 6-6 as the dashed and solid curves, respectively. Values of $\mu_r = \varepsilon_r = 3.98 - j\ 0.015$ were achieved at the targeted design frequency of 1.5 GHz.

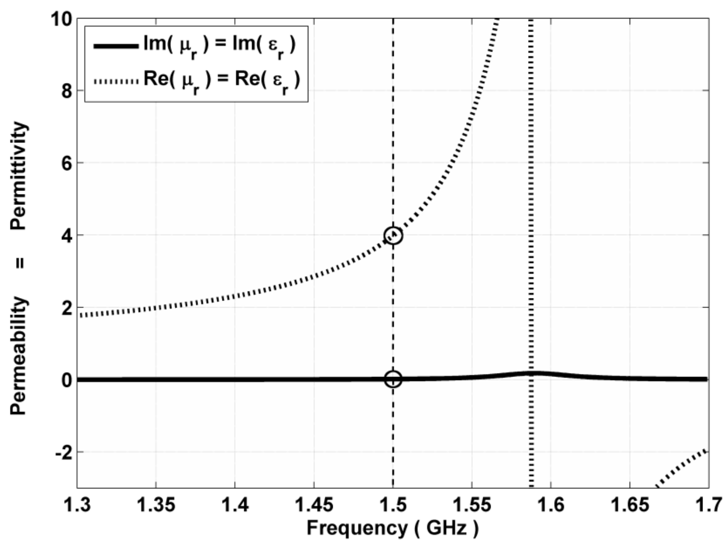

Figure 6-6: Real and imaginary parts of the effective parameters that are computed by substituting the surface impedance values, Z_{FSS}, into (6-8) and (6-9). At the targeted design frequency of 1.5 GHz, values of $\mu_r = \varepsilon_r = 3.98 - j\ 0.015$ are achieved.

The real part of the surface impedance (R_{FSS}) for the optimized composite metamaterial, computed via PMM, is displayed in Figure 6-7 (a), along with the HFSS computation of the surface resistance of a homogenous slab using the dispersive constitutive parameters shown in Figure 6-6. The dashed lines in Figure 6-7 (a) and (b) represent the surface resistance and reactance, respectively, of an ideal non-dispersive magneto-dielectric material of the same thickness. In Figure 6-7 (b), the imaginary part of the surface impedance (X_{FSS}) of the optimized composite metamaterial, computed via PMM, is illustrated along with the HFSS computation of the surface reactance of a homogenous slab using the dispersive constitutive parameters of Figure 6-6.

Table 6-1: Design Parameters for the Low-loss Matched Impedance Metamaterials at 1.50 GHz

Targeted Effective Constitutive Parameters	$\mu_r = \varepsilon_r = 3 - j\ 0.005$	$\mu_r = \varepsilon_r = 4 - j\ 0.005$
Unit Cell Dimensions (cm x cm)	0.6006 x 0.6006	0.460 x 0.460
Superstrate Permittivity, ε_1	11.61 - j 0.0174	11.56 - j 0.0155
Substrate Permittivity, ε_2	8.50 - j 0.0144	11.34 - j 0.0007
Superstrate Thickness, t_1	0.111 cm	0.085 cm
Substrate Thickness, t_2	0.162 cm	0.202 cm

6.5.2. Synthesis of Low-loss Dual Magneto-dielectric Metamaterials

The third design example was optimized to exhibit effective material properties of $\mu_r = \varepsilon_r = 2 - j\ 0.005$ at two separate frequencies of 1.5 GHz and 1.8 GHz. A GA population of 20 chromosomes was permitted to run for 500 iterations using the cost function provided in (6-12) at both frequencies, where $N = 2$. The unit cell geometry evolved by the GA is shown in Figure 6-8 (a), while the other optimized design parameters are provided in Table 6-2.

The real and imaginary parts of the frequency dependent effective parameters that are determined by substituting the PMM computed surface impedance values (Z_{FSS}) and the thickness (d) into (6-8) and (6-9) are shown plotted in Figure 6-10. Effective material parameter values of $\mu_r = \varepsilon_r = 1.96 - j\ 0.165$ at 1.5 GHz and $\mu_r = \varepsilon_r = 2.02 - j\ 0.116$ at 1.8 GHz were achieved.

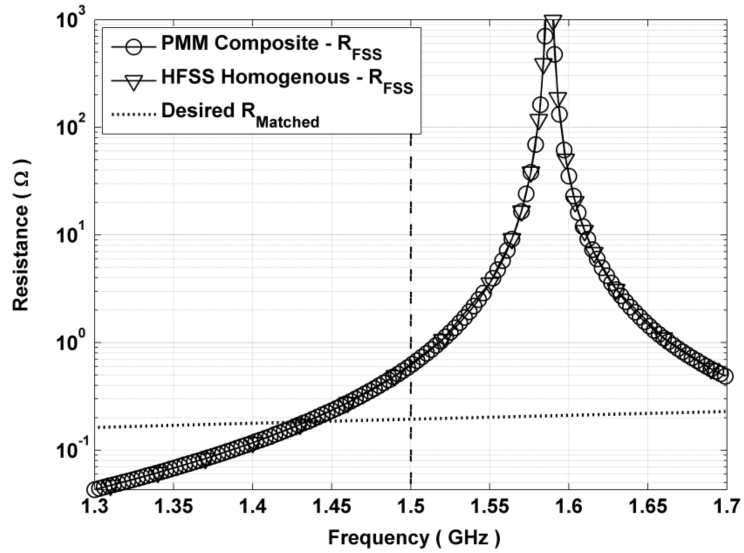

(a)

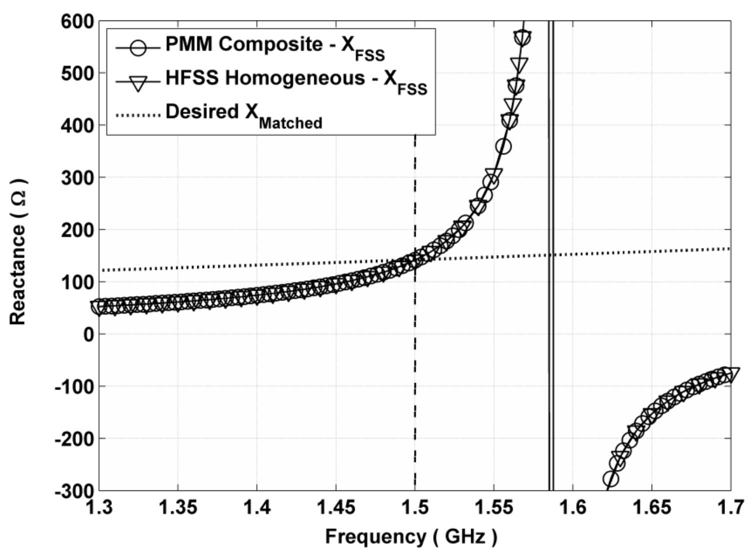

(b)

Figure 6-7: Real (a) and imaginary (b) parts of the surface impedance (Z_{FSS}) of the composite metamaterial targeting $\mu_r = \varepsilon_r = 4 - j\ 0.005$, along with the surface impedance of a homogenous slab with the dispersive constitutive parameter values assigned to it. The dashed lines represent the surface resistance of an ideal non-dispersive magneto-dielectric material with the same thickness.

The real part of the surface impedance of the optimized composite metamaterial (R_{FSS}), computed via PMM, is displayed in Figure 6-9 (a) along with the HFSS computation of the surface resistance of a homogenous slab using the dispersive constitutive parameters shown in Figure 6-10. The dashed lines in Figure 6-9 represent the surface resistance and reactance of an ideal non-dispersive magneto-dielectric material of equivalent thickness. In Figure 6-9 (b), the imaginary part of the surface impedance of the optimized composite metamaterial (X_{FSS}), computed via PMM, is illustrated along with the HFSS computation of the surface reactance for a homogenous slab using the dispersive constitutive parameters shown in Figure 6-10.

Table 6-2: Design Parameters for the Dual-band Low-loss Matched-Impedance Metamaterial at 1.5 GHz and 1.8 GHz.

Targeted Effective Constitutive Parameters	$\mu_r = \varepsilon_r = 2 - j\ 0.005$
Unit Cell Dimensions (cm x cm)	3.988 x 3.988
Superstrate Permittivity, ε_1	$8.76 - j\ 0.0908$
Substrate Permittivity, ε_2	$11.02 - j\ 0.0634$
Superstrate Thickness, t_1	0.175 cm
Substrate Thickness, t_2	0.138 cm

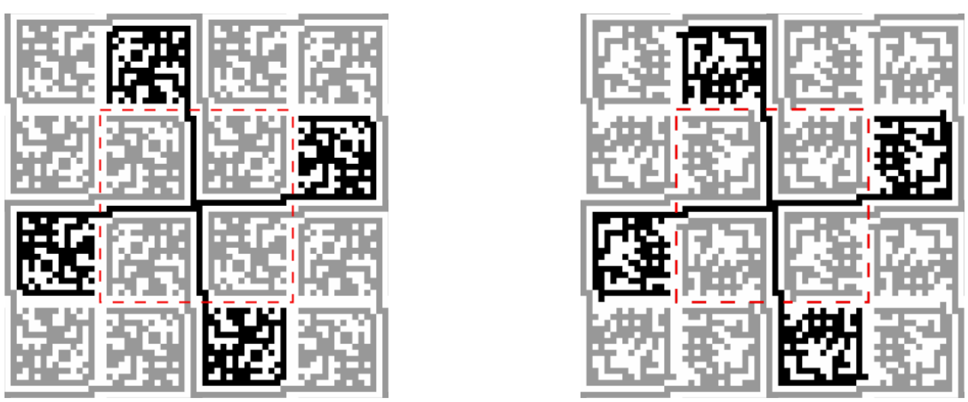

(a) (b)

Figure 6-8: FSS unit cell geometries for the design of (a) dual band metamaterial with $\mu_r = \varepsilon_r = 2 - j\ 0.005$, and (b) single band metamaterial with $\mu_r = \varepsilon_r = -4 - j\ 0.005$, where black and gray shaded regions represent PEC pixels with two-tones used to distinguish the interconnected structure which spans multiple unit cells. Note that the dashed black lines designate the borders of each unit cell.

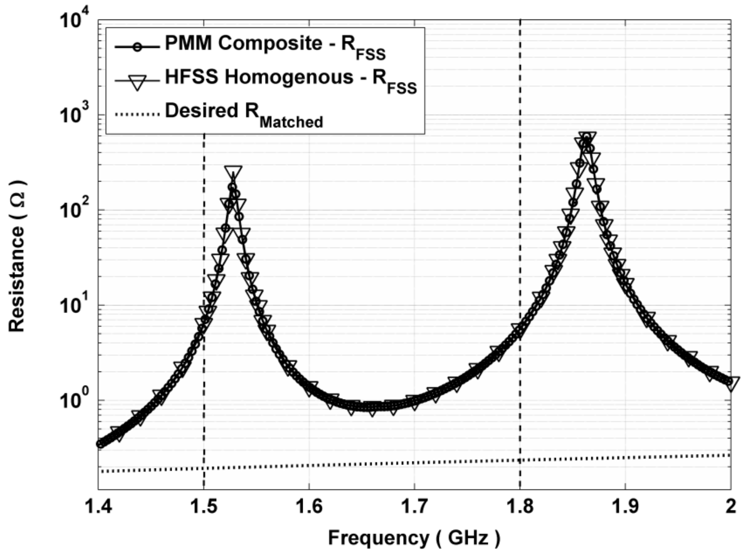

(a)

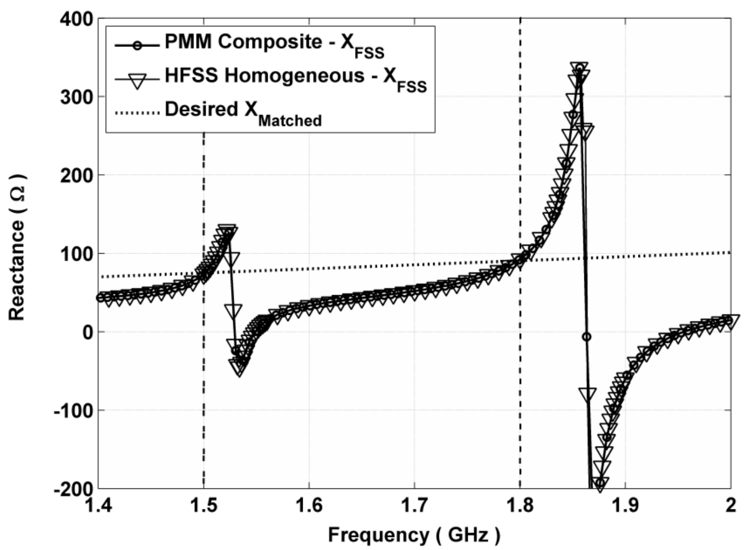

(b)

Figure 6-9: Real (a) and imaginary (b) parts of the surface impedance (Z_{FSS}) of the composite metamaterial targeting $\mu_r = \varepsilon_r = 2 - j\ 0.005$, along with the surface impedance of a homogenous slab with the dispersive constitutive parameter values assigned to it. The dashed lines represent the surface resistance of an ideal non-dispersive magneto-dielectric material with the same thickness.

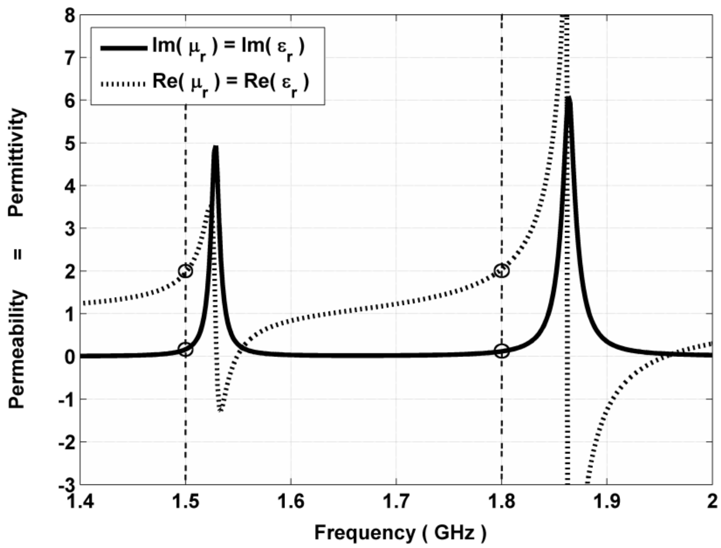

Figure 6-10: Real and imaginary parts of effective parameters that are computed by substituting the surface impedance values, Z_{FSS}, into (6-8) and (6-9). The targeted design frequencies are 1.5 GHz and 1.8 GHz.

6.5.3. Synthesis of Low-loss Double-negative Magneto-dielectric Metamaterials

The fourth and final low-loss example was optimized to possess double-negative matched impedance magneto-dielectric properties given by $\mu_r = \varepsilon_r = -4 - j\,0.005$, at the operating frequency of 1.5 GHz. A GA population of 50 chromosomes was permitted to run for 1000 iterations using the cost function found in (6-12). The unit cell geometry evolved by the GA is shown in Figure 6-8 (b) while the other optimized design parameters are provided in Table 6-3. The real and imaginary parts of the effective metamaterial parameters that are determined by substituting the PMM computed surface impedance values (Z_{FSS}) and the thickness (d) into (6-8) and (6-9) are illustrated in Figure 6-11 by the dashed and solid curves, respectively. Effective metamaterial parameter values of $\mu_r = \varepsilon_r = -4.07 - j\,0.014$ are achieved at the targeted operating frequency of 1.5 GHz. The real part of the surface impedance of the optimized composite metamaterial (R_{FSS}) computed via PMM is displayed in Figure 6-12 (a) along with the HFSS computation of the surface resistance of a homogenous slab using the dispersive constitutive parameters shown in Figure 6-11. The dashed lines represent the surface resistance and reactance of an ideal non-dispersive magneto-dielectric material with an identical thickness to the metamaterial. In Figure 6-12 (b), the imaginary part of the surface impedance of the optimized composite metamaterial, X_{FSS}, computed via PMM is illustrated along with the HFSS computation of the surface reactance corresponding to a homogenous slab using the dispersive constitutive parameters of Figure 6-11.

Table 6-3: Design Parameters for the Low-loss Double-Negative Matched Impedance Metamaterials at 1.5 GHz.

Targeted Effective Constitutive Parameters	$\mu_r = \varepsilon_r = -4 - j\ 0.005$
Unit Cell Dimensions (cm x cm)	0.893 x 0.893
Superstrate Permittivity, ε_1	7.65 - j 0.0014
Substrate Permittivity, ε_2	5.93 - j 0.0009
Superstrate Thickness, t_1	0.103 cm
Substrate Thickness, t_2	0.102 cm

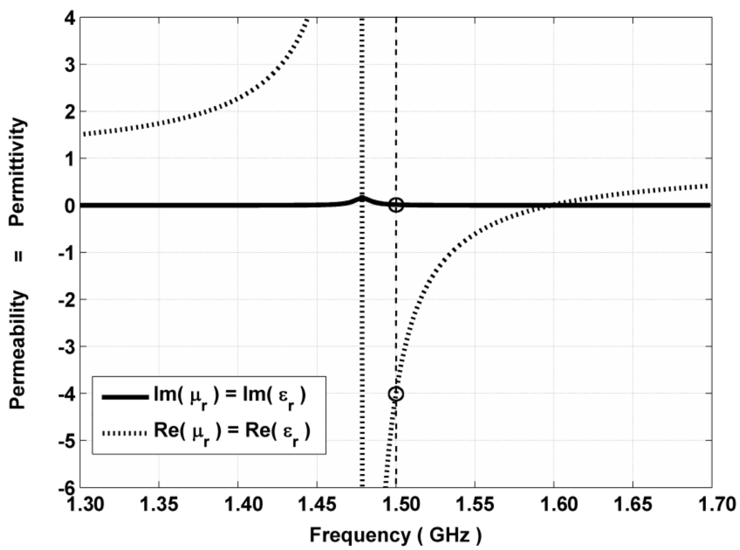

Figure 6-11: Real and imaginary parts of effective parameters that are computed by substituting the surface impedance values, Z_{FSS}, into (6-8) and (6-9). At the targeted design frequency of 1.5 GHz values of $\mu_r = \varepsilon_r = -4.07 - j\ 0.014$ are achieved

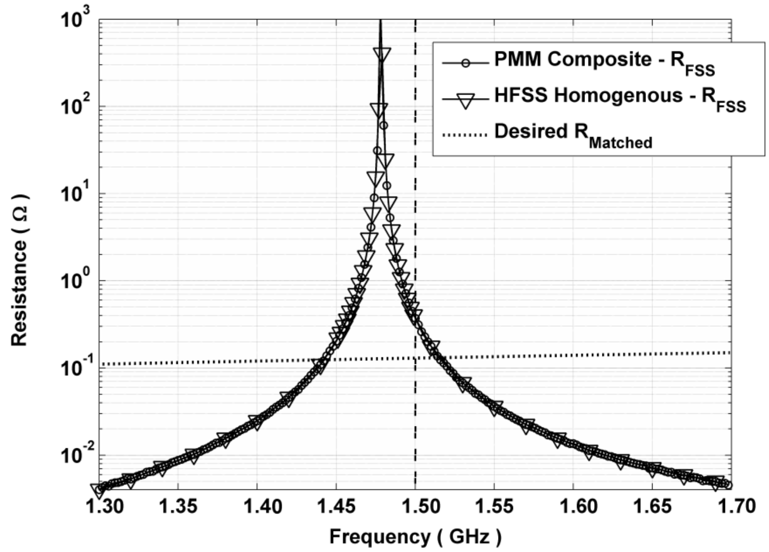

(a)

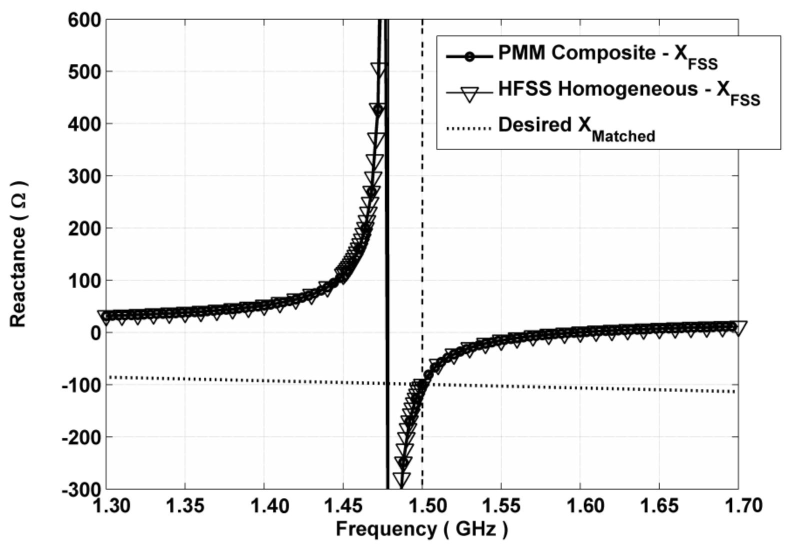

(b)

Figure 6-12: Real (a) and imaginary (b) parts of the surface impedance (Z_{FSS}) of the composite metamaterial targeting $\mu_r = \varepsilon_r = -4 - j\ 0.005$, along with the surface impedance of a homogenous slab with the dispersive constitutive parameter values assigned to it. The dashed lines represent the surface resistance of an ideal non-dispersive magneto-dielectric material with the same thickness.

6.5.4. Synthesis of Single-band Magneto-dielectric Metamaterial Absorber

The equations that were derived previously can be modified for electromagnetic absorber applications where thin composite structures are optimized to achieve a MIMDM with high loss. In this case the surface impedance of the composite structure can be controlled such that it is matched to free space ($Z_{FSS} = R_{FSS} + j\ X_{FSS} = Z_0$), achieving zero reflection at the free space-absorber interface [3]. The surface impedance of the composite structure (Z_{FSS}) can be expressed in terms of the equivalent PEC-backed homogenous matched impedance ($\mu_r = \varepsilon_r$) magneto-dielectric material permittivity and permeability by using (6-8) and (6-9). Since the surface impedance of the composite structure must match the impedance of free space, it is easily determined that

$$Z_{FSS} = R_{FSS} + jX_{FSS} = Z_0\,, \rightarrow R_{FSS} = Z_0 \text{ and } X_{FSS} = 0 \tag{6-13}$$

Based on this requirement, the desired values for μ'_r and μ''_r can be derived from (6-8) and (6-9) such that

$$X_{FSS} = 0 \rightarrow \mu'_r = n\lambda_0 / 4d\,, \quad \text{where } n = 1,2,3,... \tag{6-14}$$

and

$$R_{FSS} = Z_0 \rightarrow \mu''_r = m\lambda_0 / 2d\,, \quad \text{where } m = 1,2,3,... \tag{6-15}$$

These equations ensure a matched impedance material with zero reflection at the free space-absorber interface as well as high electric and magnetic losses which make it suitable for absorber applications. The first absorber example targets material properties of $\mu_r = \varepsilon_r = 7.153 - j\ 14.31$ at 1.5 GHz, while the optimized composite structure achieves $\mu_r = \varepsilon_r = 6.324 - j\ 12.76$ at the desired operating frequency as shown in Figure 6-15. For this optimization, a 25 member GA population was evolved through 500 generations. The resulting FSS screen structure is illustrated in Figure 6-13 (a). Its square unit cell has a length of 5.88 mm (0.0294 λ_0) on a side and it is sandwiched between dielectric layers with thicknesses t_1 = 1.62 mm and t_2 = 5.37 mm. The total thickness of the structure is 0.03495 λ_0. The relative dielectric constants of the layers are ε_1 = 3.14 - j 0.0664 and ε_2 = 6.79 - j 1.1563.

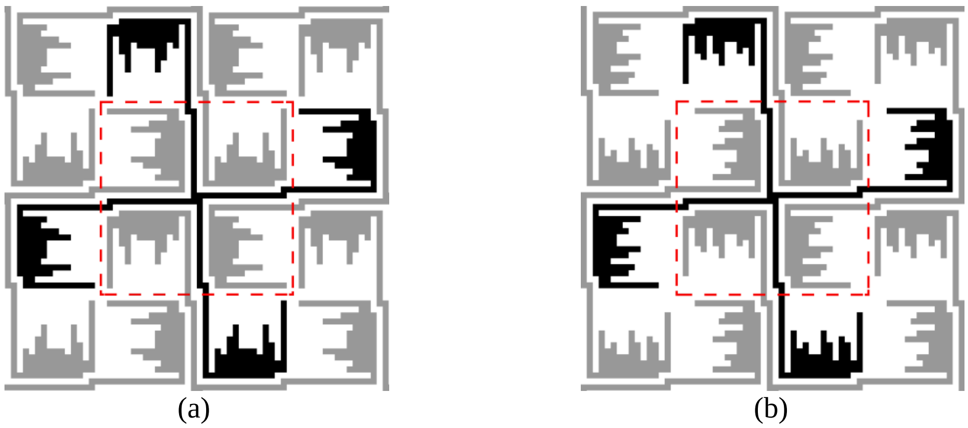

Figure 6-13: FSS unit cell geometries for the (a) single band, and of the (b) dual band magneto-dielectric absorbers, where the black and gray shaded regions represent PEC pixels with two-tones used to distinguish the interconnected structure which spans multiple unit cells. Note that the dashed black lines designate the borders of the unit cell.

The real part (R_{FSS}) of the surface impedance of the optimized composite metamaterial, computed via PMM and HFSS, are displayed in Figure 6-14 (a). Similar to the previous designs, the curves agree well save for a small frequency shift caused by the different meshing strategies employed in the two solvers. Figure 6-14 (a) also illustrates the HFSS computation of the surface resistance of a homogenous slab using the dispersive constitutive parameters shown plotted in Figure 6-15. The dashed lines in Figure 6-14 (a) and Figure 6-14 (b) represent the surface resistance and reactance, respectively, of an ideal non-dispersive magneto-dielectric material with an identical thickness to the metamaterial. Figure 6-14 (b) illustrates the imaginary part of the surface impedance (X_{FSS}) of the optimized composite metamaterial, computed via PMM and HFSS. Again, the reactance curves agree well save for a small frequency shift. Figure 6-14 (b) also illustrates the HFSS computation of the surface reactance of a homogenous slab using the dispersive constitutive parameters found in Figure 6-15.

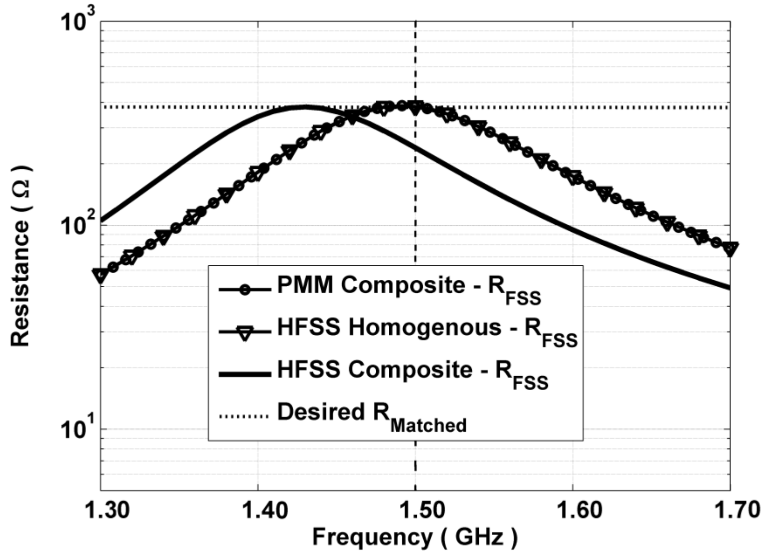

(a)

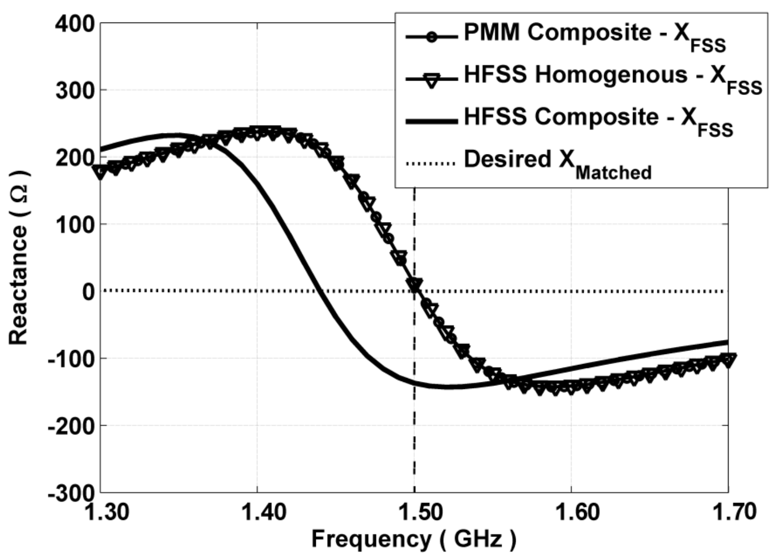

(b)

Figure 6-14: Real (a) and imaginary (b) parts of the surface impedance (Z_{FSS}) of the composite metamaterial absorber design, computed using PMM and HFSS, along with the surface impedance of a homogenous slab with the dispersive constitutive parameter values assigned to it. The dashed lines represent the surface resistance of an ideal non-dispersive magneto-dielectric material with the same thickness.

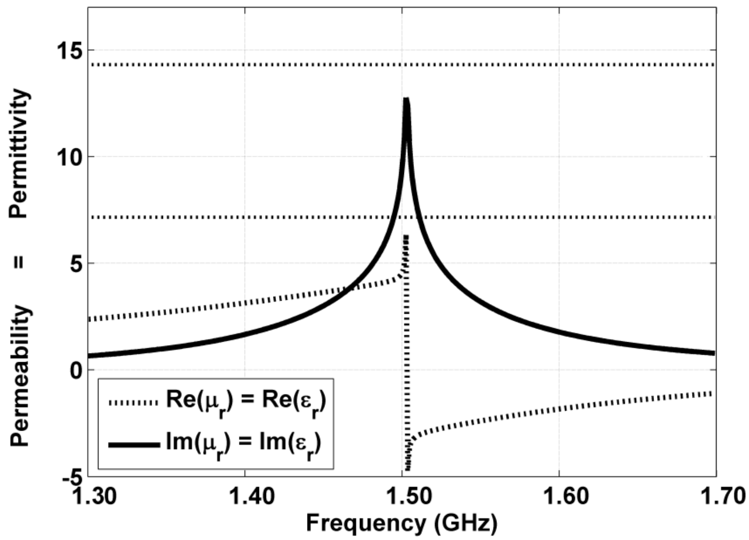

Figure 6-15: Real and imaginary parts of effective parameters that are computed by substituting the surface impedance values, Z_{FSS}, into (6-8) and (6-9). At the targeted design frequency of 1.5 GHz values of $\mu_r = \varepsilon_r = 6.324 - j\ 12.76$ are achieved.

A plot of the reflection magnitude versus frequency for this structure is shown in Figure 6-16 (a), where attenuation of more than 45 dB at the design frequency of 1.5 GHz is attained. Angular dependency of the reflection is also computed via PMM and illustrated in Figure 6-16 (b). The very small subwavelength unit cell structures of the metamaterial absorber provide a remarkably stable angular response, even with incident angles up to 50° from broadside.

6.5.5. Synthesis of Dual-band Magneto-dielectric Metamaterial Absorber

The second example is a dual band absorber designed to operate at 2.0 GHz and 2.5 GHz. This design targets effective material properties of $\mu_r = \varepsilon_r = 4.1946 - j\ 8.3893$. In this case, the GA evolved a population of 25 members through 500 generations.

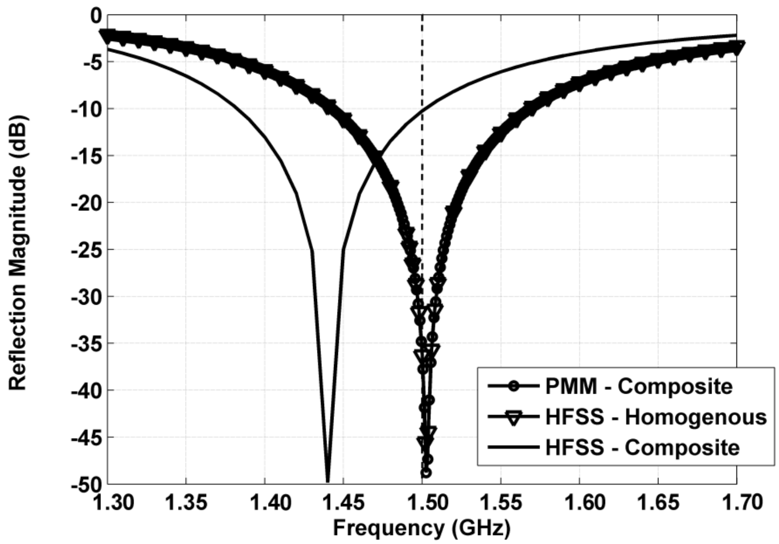

(a)

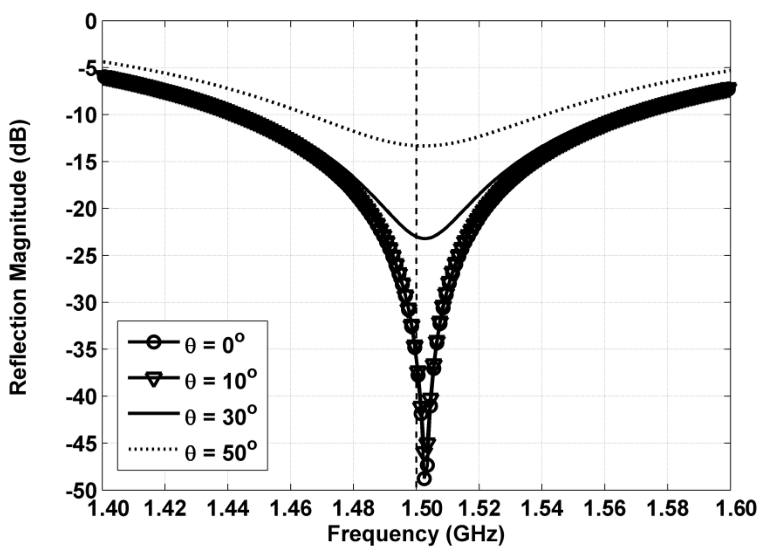

(b)

Figure 6-16: (a) Frequency response of the single-band thin composite magneto-dielectric absorber, where reflection coefficient magnitude of the design is shown. (b) Angular dependency of the reflection magnitude, where good absorber response is observed up to θ=50° from normal.

The square unit cell of the optimized design is 1.997 cm (0.1664 λ_0 at 2.5 GHz) on a side and it is sandwiched between dielectric layers with thicknesses t_1 = 5.95 mm and t_2 = 5.97 mm. The total thickness of the structure is 0.099 λ_0 at 2.5 GHz. The layers have relative dielectric constants of ε_1 = 11.72 - j 1.0469 and ε_2 = 9.44 - j 2.3594. The real and imaginary parts of the surface impedance of the optimized dual band composite metamaterial absorber computed via PMM and HFSS are displayed in Figure 6-18 (a) and (b), respectively. The surface impedance of a homogenous slab with the dispersive effective material parameter values is also displayed in Figure 6-18. Excellent agreement is achieved for both the R_{FSS} and X_{FSS}. The dashed lines highlight the free space wave impedance (Z_0), and very good agreement is observed at the target design frequencies. The reflection magnitude of this structure is illustrated in Figure 6-17, showing significant attenuation at both bands of operation.

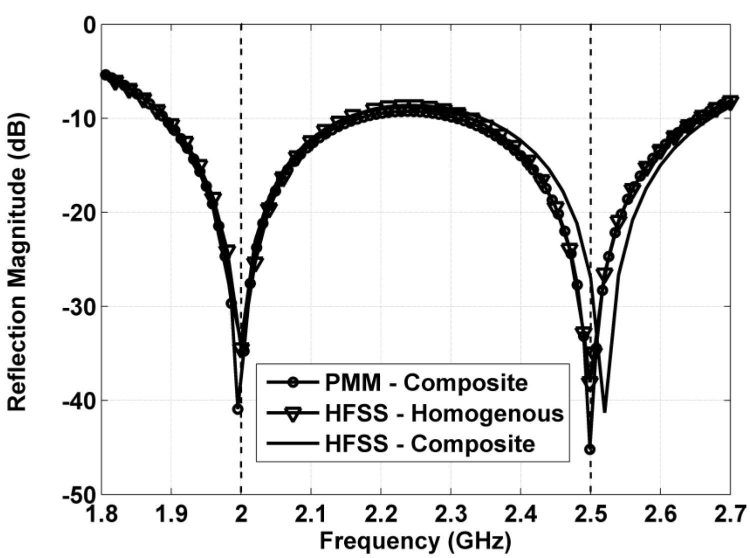

Figure 6-17: Frequency response of the dual band thin composite magneto-dielectric absorber, where the magnitude of the reflection coefficient is shown plotted as a function of frequency. Excellent agreement is observed between all simulations.

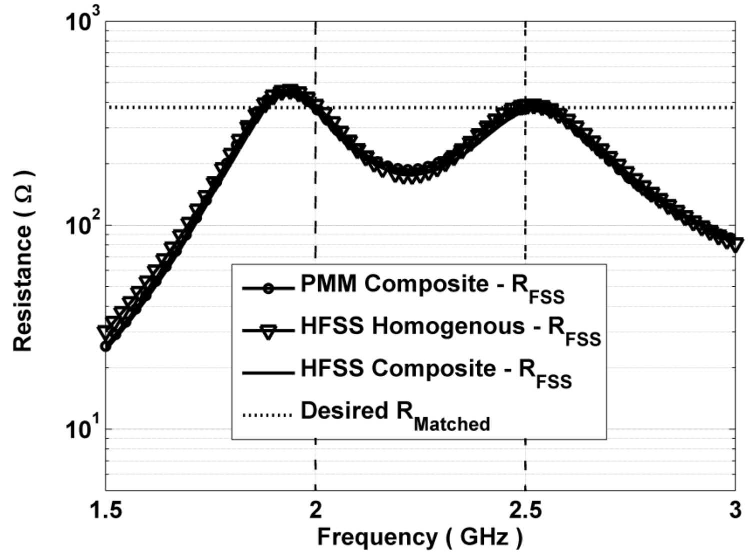

(a)

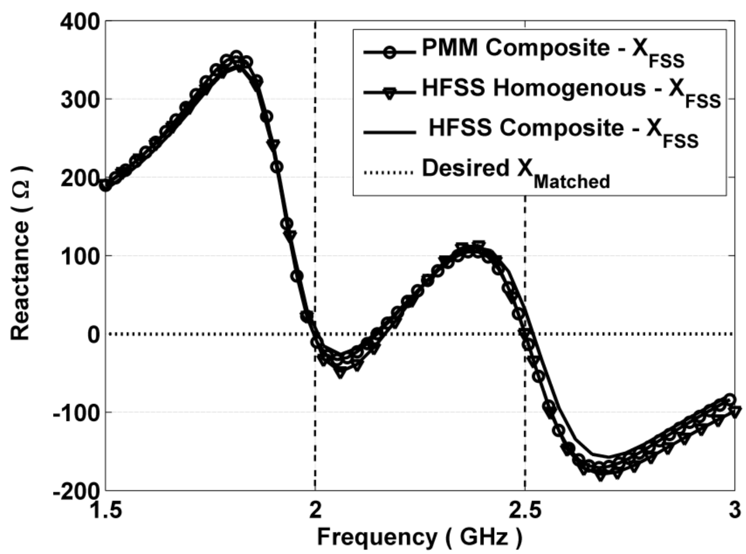

(b)

Figure 6-18: Real (a) and imaginary (b) parts of the surface impedance (Z_{FSS}) of the composite metamaterial absorber design, computed using PMM and HFSS, along with the surface impedance of a homogenous slab with the dispersive constitutive parameter values assigned to it. Excellent agreement is observed.

6.5.6. Rectangular Microstrip Antenna Miniaturization via MIMDM Substrates

Rectangular microstrip antennas are one of the most popular and widely used low profile antennas particularly in aircraft, satellite, air missile and other space applications, where the size of the antenna, cost of fabrication, ease of installation and performance are important. In its simplest form, a metallic rectangular shaped radiating structure is either suspended certain distance above a ground plane and excited by a probe feed or it can be printed on top of a dielectric substrate and fed by a matched microstrip feeding structure. Generally, it is a narrow band antenna, which has dimensions in the order of a half-wave length at the operating frequency. The size of the radiating patch element can be miniaturized by increasing the relative permittivity of the dielectric substrate which in turn leads to reduction in the operational bandwidth. This reduction can be compensated by increasing the thickness of the substrate, yet it increases the weight of the antenna system, which is not desired especially in space applications. Similarly, magnetic loading of the substrate can help with the miniaturization, but naturally occurring magnetic materials exhibit high losses at high frequencies rendering the antenna inefficient.

Miniaturization of the patch antennas can also be accomplished by designing and utilizing low-loss MIMDM substrates with desired magnetic and dielectric properties while maintaining the relative bandwidth. Below, a MIMDM was optimized to achieve effective material properties of $\mu_r = \varepsilon_r = 3 - j\, 0.005$ at 1.5 GHz targeting a miniaturization factor of 3. A slight modification is made to the structure, where the pixelized PEC area is forced to be small to provide space for the probe feed through it. In the simulations of the patch antenna, a coax feeding structure is simulated for simplicity. The GA was configured with a population size of 15 chromosomes and was permitted to run for a maximum of 500 iterations using the cost function defined in (6-12). The unit cell geometry evolved by the GA is illustrated in Figure 6-19, while the remaining optimized parameters of the structure are provided in Table 6-4.

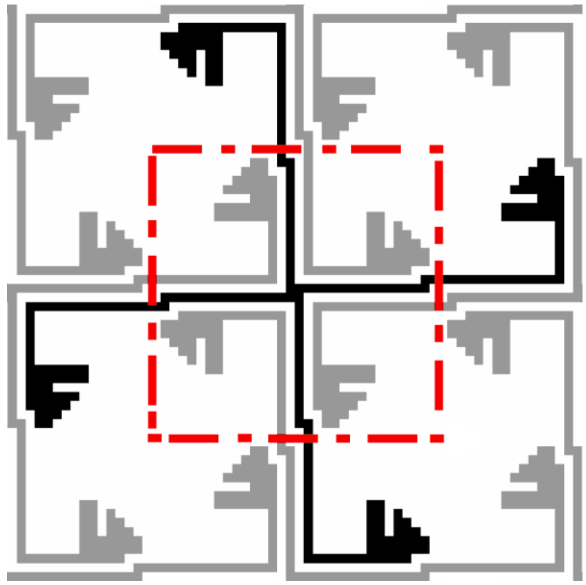

Figure 6-19: FSS unit cell geometry for the targeted designs of $\mu_r = \varepsilon_r = 3 - j\ 0.005$, where black and gray shaded regions represent PEC pixels to distinguish the interconnected structure which spans multiple unit cells. Note that the dashed red lines designate the borders of a single unit cell.

Table 6-4: Design Parameters for the Low-loss Matched Impedance Metamaterials at 1.5 GHz.

Targeted Effective Constitutive Parameters	$\mu_r = \varepsilon_r = 3 - j\ 0.005$
Unit Cell Dimensions (cm x cm)	1.099 x 1.099
Superstrate Permittivity, ε_1	5.94 - j 0.0031
Substrate Permittivity, ε_2	2.63 - j 0.0017
Superstrate Thickness, t_1	0.285 cm
Substrate Thickness, t_2	0.171 cm

Figure 6-20 plots the real and imaginary parts (black and red curves, respectively) of the constitutive parameters that are determined by substituting the PMM computed surface impedance values (Z_{FSS}) and the thickness (d) into (6-8) and (6-9). This figure also plots the HFSS computed values of the same unit cell shown in green and blue curves, respectively. The two codes agree other than a small frequency shift caused by the different meshing strategies employed in the respective solvers. The real part of the surface impedance (R_{FSS}) for the optimized composite metamaterial is displayed in Figure 6-21 (a), which was computed via PMM and HFSS. The black line represents the surface resistance of an ideal non-dispersive magneto-dielectric material of the same thickness ($R_{matched}$). The imaginary parts of the surface impedance (X_{FSS}) of the optimized composite metamaterial computed via PMM and HFSS are displayed in Figure 6-21 (b). Similar to the real parts, the shape of the curves agree well, save for a small frequency shift caused by the different meshing strategies employed in each code. The black line represents the surface reactance ($X_{matched}$) of an ideal non-dispersive magneto-dielectric material of the same thickness.

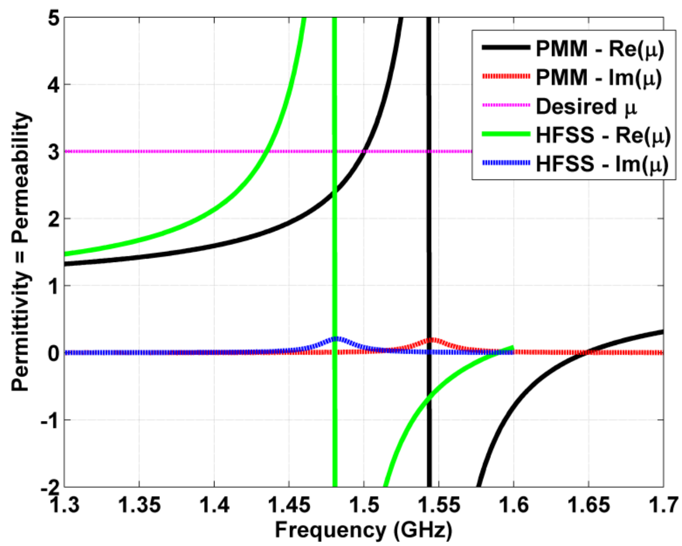

Figure 6-20: Real and imaginary parts of the effective parameters that are computed by substituting the surface impedance values (Z_{FSS}) into (6-8) and (6-9).

Considering the fact that the simulation of the microstrip patch antenna on finite length MIMDM substrate will be carried out in HFSS, a small frequency shift for the operating frequency of the patch antenna is expected as well. In order to demonstrate the MIMDM slab as a substrate for miniaturized patch antennas, a MIMDM ground plane is simulated in HFSS.

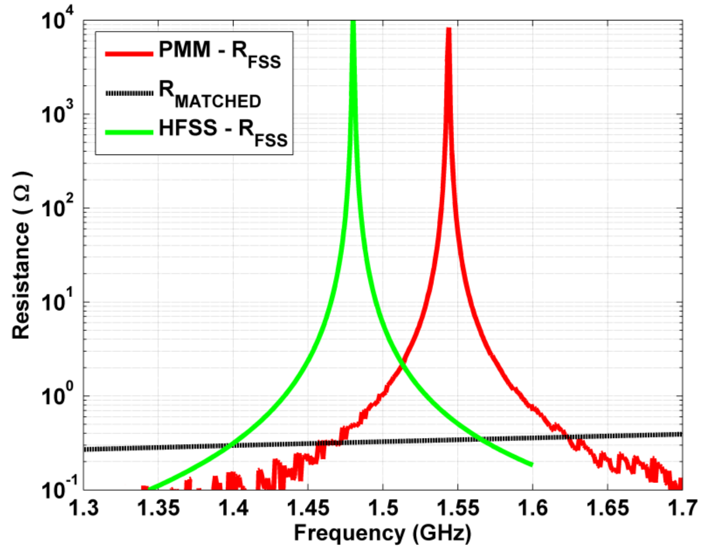

(a)

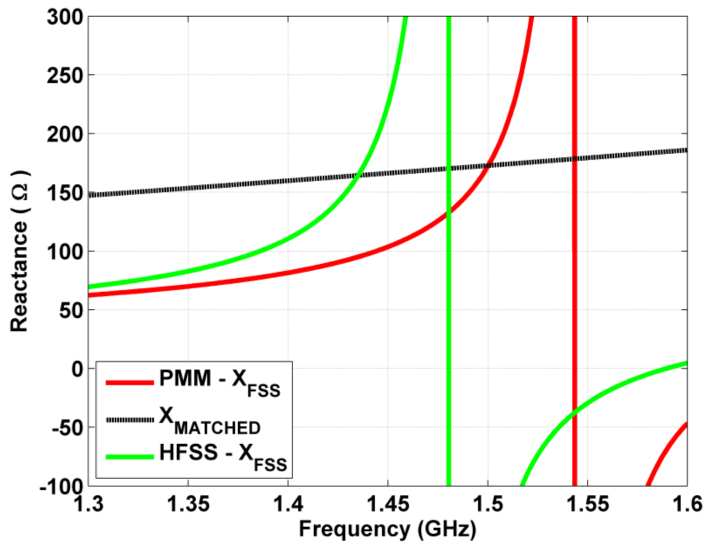

(b)

Figure 6-21: Real (a) and imaginary (b) parts of the surface impedance (Z_{FSS}) of the composite metamaterial targeting $\mu_r = \varepsilon_r = 3 - j\ 0.005$, computed via PMM and HFSS. The black lines represent the surface resistance of an ideal non-dispersive magneto-dielectric material with the same thickness.

The size of the MIMDM structure is set to be 13.18 cm by 14.28 cm, which corresponds to 13 unit cells in length and 14 unit cells in width. The square patch size is selected to be 30 mm by 30mm and fed by a probe feed. This lumped element feed is located 1.0 mm away from the center of the edge of the patch antenna as seen in Figure 6-22. In order to be able to simulate the structure in HFSS, a small ground plane is desired due to large memory requirements, yet it should be large enough to allow the patch antenna work efficiently.

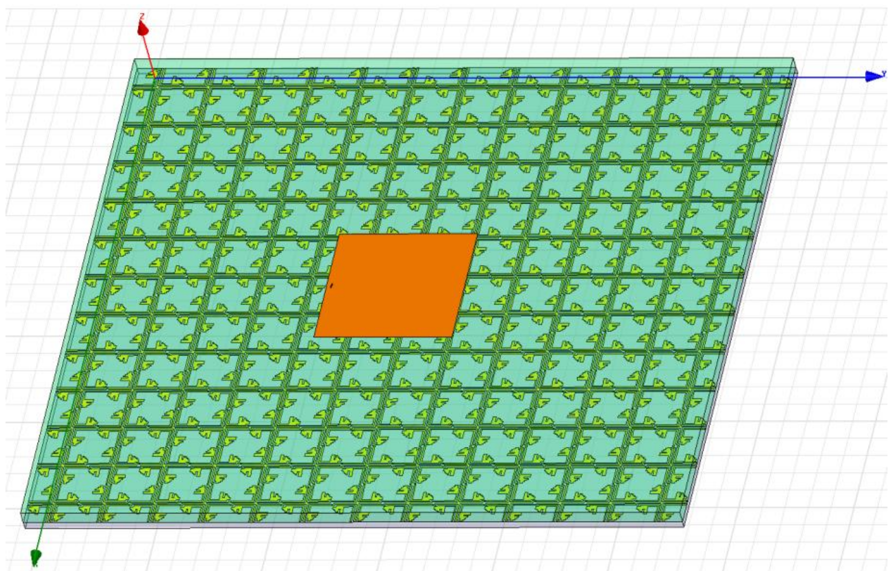

Figure 6-22: HFSS simulation of the miniaturized square shaped patch antenna, shaded in orange color. Patch antenna is printed on top of the MIMDM substrate and fed by a lumped port in HFSS, representing a coax feed.

For comparison purposes, two more simulations are carried out with same size substrates with different theoretical material properties. In the first simulation, a miniaturized patch antenna printed on a homogenous loss-less dielectric material with relative permittivity of 10 is carried out. For the second simulation, a theoretical loss-less matched-impedance magneto-dielectric material is utilized. Comparison of patch antennas on different substrates is provided in Figure 6-23.

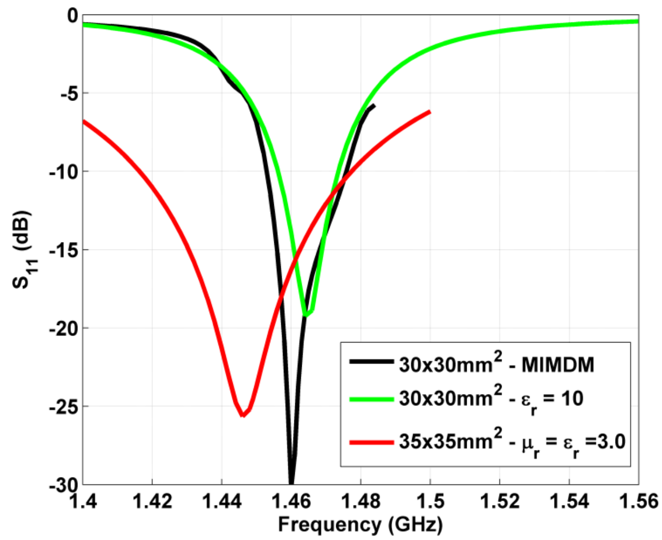

Figure 6-23: S-parameter comparison for three different simulations with miniaturized patch antennas.

In Figure 6-23, the black curve represents the S_{11} of the miniaturized patch antenna placed on the optimized MIMDM material, where the dimensions of the antenna is 30 mm by 30 mm. The green curve represents the S_{11} of the same size miniaturized patch antenna placed on a loss-less homogenous dielectric material with relative permittivity of 10. The red curve represents the performance of a similar shaped, 35 mm by 35 mm, patch antenna on an ideal homogenous loss-less matched impedance magneto-dielectric substrate with relative permittivity and permeability values of 3. It can be seen that the theoretical homogenous matched-impedance substrate can provide improved bandwidth as well as significant miniaturization. On the other hand, dielectric loaded patch can provide same amount of miniaturization at the expense of narrower band performance. Due to resonance based nature of the optimized MIMDM substrate, it can only provide narrow band response in a certain range of frequencies. However, its performance is as good as dielectric-only loaded patch antenna and provides significant miniaturization, which demonstrates its utility as a match-impedance magneto-dielectric metamaterial substrate.

6.6. Summary

In this chapter of the dissertation, a new design methodology has been presented for the synthesis of matched impedance ($\mu_r = \varepsilon_r > 1$) magneto-dielectric metamaterial (MIMDM) substrates. The materials are generated through optimization of thin metallo-dielectric metasurfaces comprised of a periodic array of electrically small and rotationally symmetric unit cells which are sandwiched between two thin dielectric layers and backed by a perfectly conducting ground plane. By optimizing the surface impedance of the composite structure, it is possible to synthesize matched impedance magneto-dielectrics with a wide range of effective parameters.

It was shown that the GA optimization is well suited for designing low-loss matched impedance magneto-dielectrics with both double-positive and double-negative effective parameters for single or multiple frequency bands. Lastly, single-band and dual-band lossy matched impedance magneto-dielectric materials were presented that would make effective electromagnetic absorbers. Due to the electrically small unit cell design, the absorbers demonstrate good performance over a wide field of view, even with incident angles of up to 50 degrees from broadside. For both low-loss and lossy MIMDM structures, it was shown that the full-wave simulations of the substrates assuming effective medium parameters were found to be in excellent agreement with the results when the actual subwavelength metamaterial structure was included in the model.

Chapter 7

Ultra-small Unit cell Artificial Magnetic Conductors

This chapter introduces a new unit cell geometry, which is electrically very small enabling design of smaller sub-wavelength artificial magnetic conducting (AMC) surface unit cells compared to the existing literature. The proposed design provides excellent field of view and identical bandwidth compared to the state-of-the-art AMCs. Different variations of this unique AMC structure are studied along with an optimization schema, where the WDO is utilized to synthesize AMCs with precise control of the operating frequencies.

7.1. Introduction

In Chapter 5, the historical progression of the artificial magnetic conducting surface synthesis was provided along with a novel method to eliminate the complete metallic ground plane backing. However, there is still room for improvement on the designs that utilize the complete metallic ground planes. The AMC designs discussed here are an extension of the AMC designs those consist of a complex FSS structure printed on top a dielectric substrate, which is backed by a PEC ground plane as illustrated in Figure 7-1 (a). The planar nature of the design approach simplifies the fabrication process, where no metallic vertical vias are needed. These designs target optimization of the top FSS layer to achieve the desired AMC condition at a single frequency [9] or at multiple frequencies [14] - [105]. Conventionally, the unit cells in the FSS based design approach are self-contained and they do not extend into neighboring unit cells. Four-folded or eight-folded symmetry can be applied to simplify the unit cell geometry, which also provides polarization insensitivity at normal incidence.

Earlier work in attempt to miniaturize the unit cell dimensions utilized convoluted elements and space filling curves, which achieve miniaturization compared to the conventional square patch AMCs at the expense of reduction in AMC bandwidth [124]-[125].

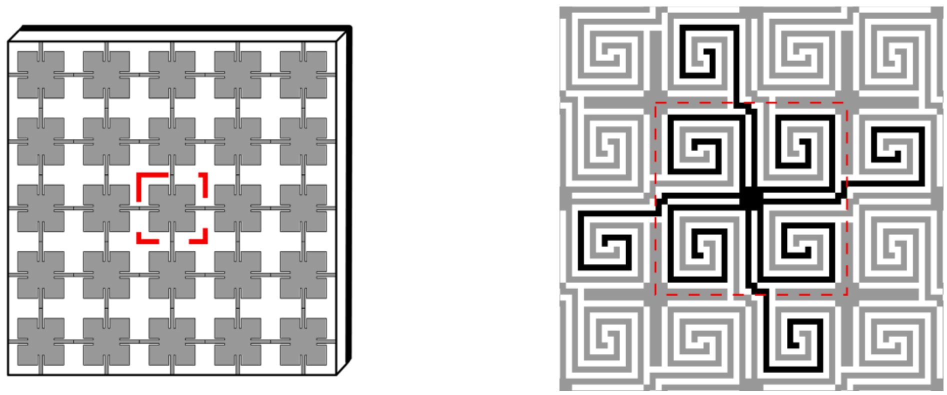

(a) (b)

Figure 7-1: (a) Profile view of a printed FSS based AMC design proposed in [9], (b) Top view of the unique AMC unit cell geometry proposed in [15]. (Figures are not drawn to scale).

Monorchio *et al.* has proposed novel smaller periodicity FSS unit cells for AMC designs to achieve enhanced bandwidth. Their design approach is based on 90° rotationally symmetric miniaturized unit cell geometries as seen in Figure 7-1 (b), which contains arms that extend into the neighboring unit cells and intertwine to achieve increased capacitance providing improved bandwidth [15, 129]. In this chapter, a novel unit cell geometry based on [15] is proposed and studied, which achieves miniaturization beyond the dimensions provided in [15] and maintains the same AMC bandwidth with excellent field of view.

Four different variations of the proposed unit cell design are illustrated in Figure 7-2, where all unit cells are 90° rotationally symmetric and posses interdigitated arms extending into the neighboring unit cells creating an electrically compact unit cell that achieves increased capacitance. The first resonance of the FSS screen is given in [15] by $\omega_0 = 1/\sqrt{(LC)}$ and the bandwidth is proportional to $BW \cong 0.5\sqrt{C/L}$. Thus, increasing the capacitance, C, increases the operational bandwidth, while the unit cell dimensions are miniaturized. The dashed lines in Figure 7-2 represent boundaries of the unit cell, where black shaded regions are the metallic geometry of the novel unit cell design that extends in to neighboring unit cells illustrated by the gray shaded regions. Four different configurations are shown below, where the interdigitation with neighboring unit cells varies.

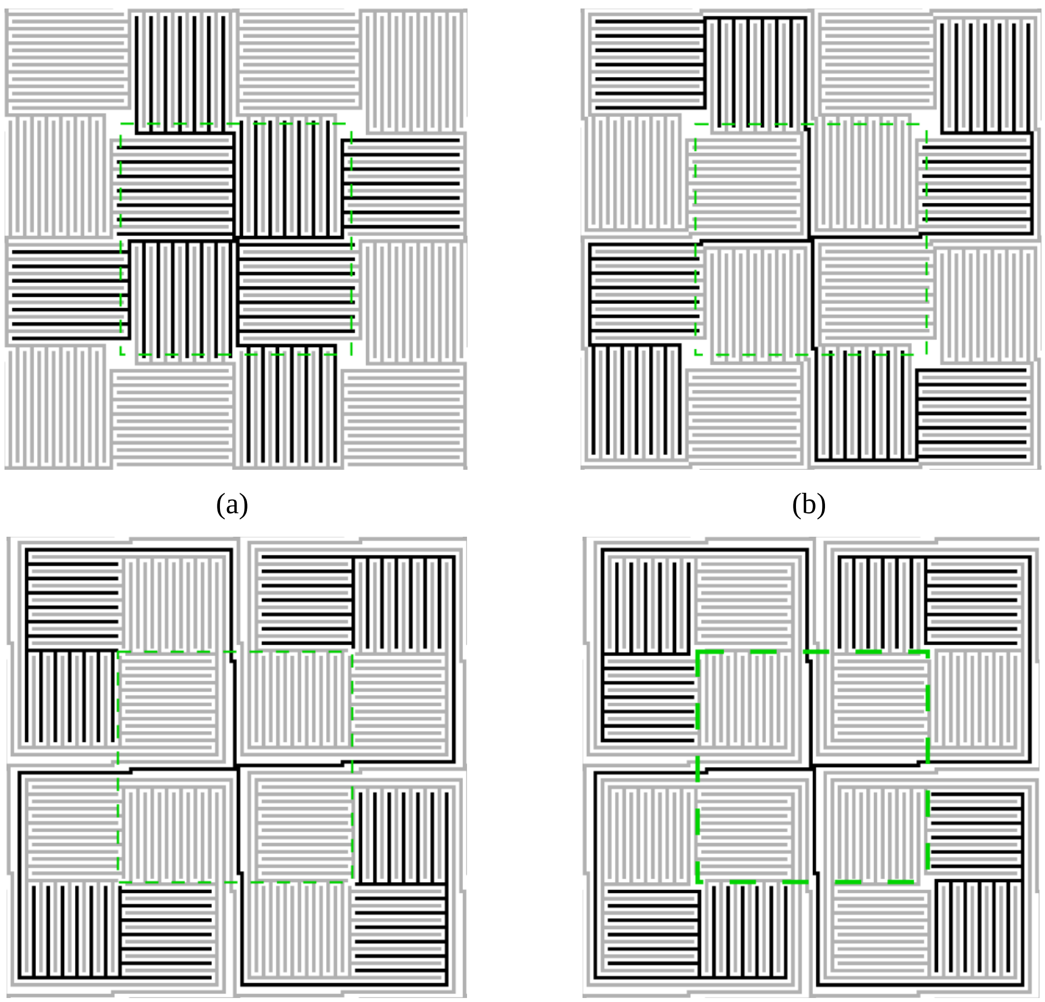

(a) (b) (c) (d)

Figure 7-2: Illustration of four different AMC unit cell geometries based on the proposed design method, where the dashed lines illustrate an individual unit cell boundaries. (a) Design 1, (b) Design 2, (c) Design 3, and (d) Design (4).

To better appreciate the advantages offered by the proposed design, a numerical study is carried out via Periodic Method of Moment (PMoM) solver. The proposed ultra-small unit cell AMCs (USAMC), the square patch AMC and Monorchio's design in [15] are evaluated in PMoM solver for operation frequency of 600 MHz and compared. This target frequency is selected to point out the problem with the large physical unit cell sizes at low frequencies, where λ_0 = 50 cm. In the comparison, all device parameters are kept identical for all designs, where the unit cells are printed on a dielectric slab with thickness of the h = 3.4 cm, and a relative permittivity of $\varepsilon_r = 2.7 - j0.1$. The only difference, which is also the deciding factor for these designs is the unit cell dimensions that allow the AMC band to be centered at around 600 MHz. The footprint comparison of the conventional square patch AMC, the Monorchio's AMC [15] and the Design 2 shown in Figure 7-2 (b) is illustrated in Figure 7-3 along with their dimensions. The USAMC achieves increased miniaturization compared to [15] and can fit 144 unit cells into the same footprint as a square patch AMC, where as Monorchio's design could only fit 16.

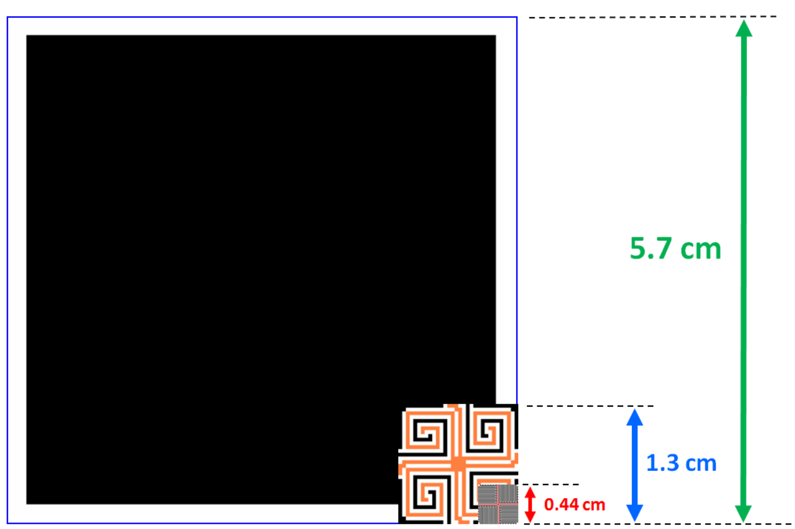

Figure 7-3: Footprint comparison of three different square AMC geometries, where all other parameters kept identical. The square patch AMC has a unit cell dimension of 5.70 cm, the Monorhio's AMC design has a dimension of 1.30 cm and proposed USAMC has a dimension of 0.44 cm.

In addition to the increased miniaturization, the USAMCs can provide nearly identical operational bandwidth as the square patch AMC and Monorchio's AMC design [15] as illustrated in Figure 7-4 for a TE polarized normally incident wave. This numerical study clearly shows that the proposed design provides increased miniaturization without any loss in the AMC bandwidth performance.

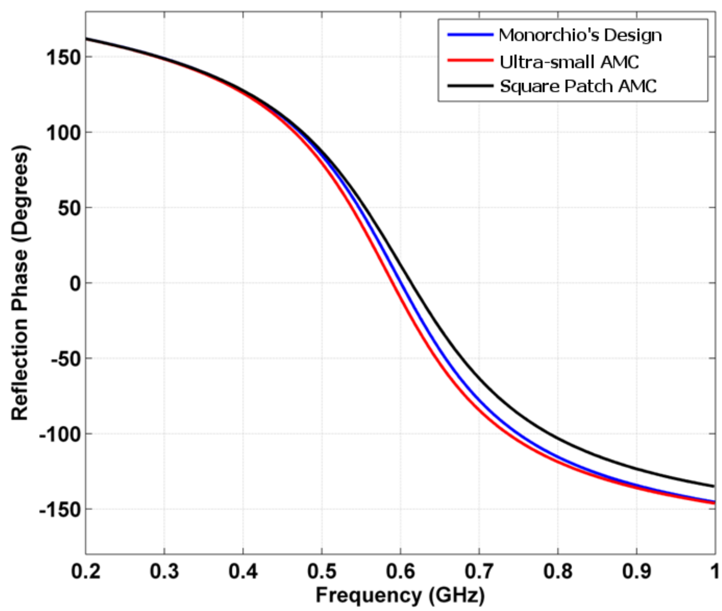

Figure 7-4: Reflection phase comparison of the three unit cell designs as shown in Figure 7-3 for a TE polarized normally incident wave.

7.2. Numerical Study of Different Configurations

The four different unit cell configurations of the proposed ultra-small unit cell artificial magnetic conducting surfaces are numerically studied by utilizing the Periodic Method of Moments solver to determine the physical limits of interdigitation and unit cell extension in to neighboring unit cells. These configurations are illustrated in Figure 7-2, where arms gradually extended further into neighboring unit cell sections, which should increase the largest effective dimension of the unit cell, in turn allowing further miniaturization. The unit cell boundaries are shown with the dashed lines in Figure 7-2, which are 0.44 mm for all configurations and printed on a 3.4 cm thick dielectric slab, with a relative permittivity of $\varepsilon_r = 2.7 - j0.1$. The only difference among them is the geometry of the FSS unit cells. For Design 1, *i.e.* effectively the shortest, the center of the AMC band is located 666 MHz. For Design 2, it is 590 MHz, for Design 3 and Design 4, it is 583 MHz. This study illustrates that extending the arms of the unit cells further into the neighboring unit cells could help to increase the miniaturization with diminishing returns.

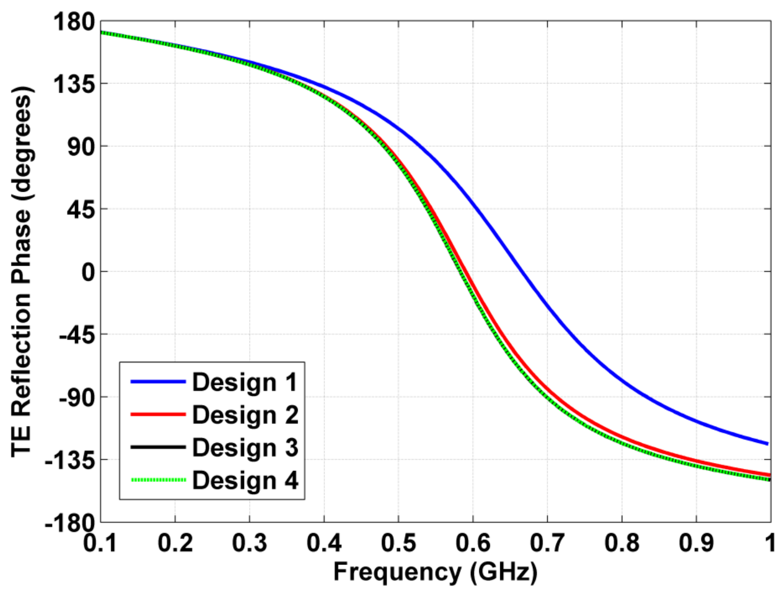

Figure 7-5: AMC band performance comparison of the four different unit cell configurations for a normally incident TE polarized wave.

In addition to the miniaturization and AMC bandwidth performance, the field of view performance is also studied to see how the frequency response of all configurations change for different polarizations and different angles of incidences varying from normal to grazing angle. The PMoM evaluation of each design example are shown in Figure 7-6, Figure 7-7, Figure 7-8, and Figure 7-9, respectively. The AMC bandwidth, that was defined as the range in between +90° and -90° of the reflection phase [8], exhibits reduction for the TE polarization for all configurations as the incidence angle increases while the center of the AMC band shifts very little in frequency. On the other hand, for the TM polarization case, the AMC bandwidth seem to be preserved over the range, yet the center of the band shifts much more in frequency than TE case.

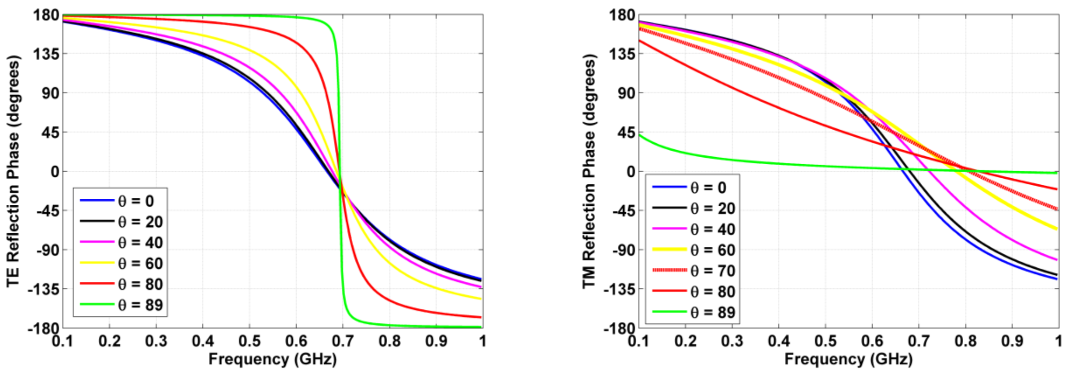

(a) (b)

Figure 7-6: Design 1; (a) TE polarization with varying angles of incidences, (b) TM polarization with varying angles of incidences.

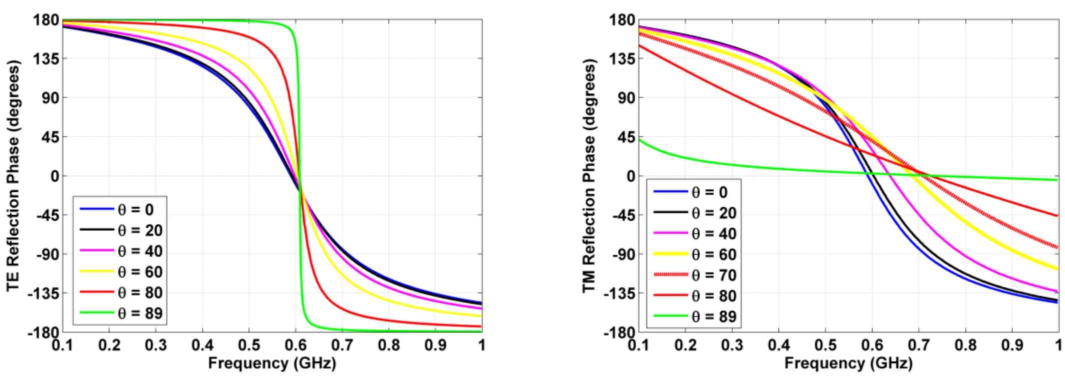

(a) (b)

Figure 7-7: Design 2; (a) TE polarization with varying angles of incidences, (b) TM polarization with varying angles of incidences.

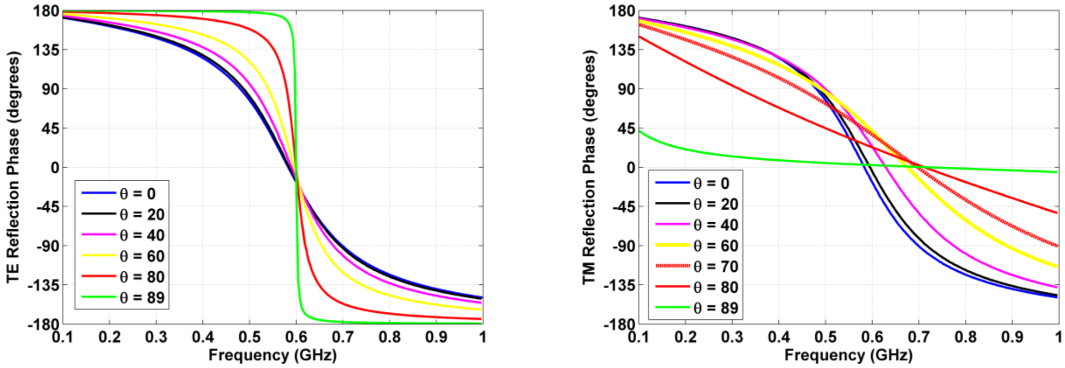

(a) (b)

Figure 7-8: Design 3; (a) TE polarization with varying angles of incidences, (b) TM polarization with varying angles of incidences.

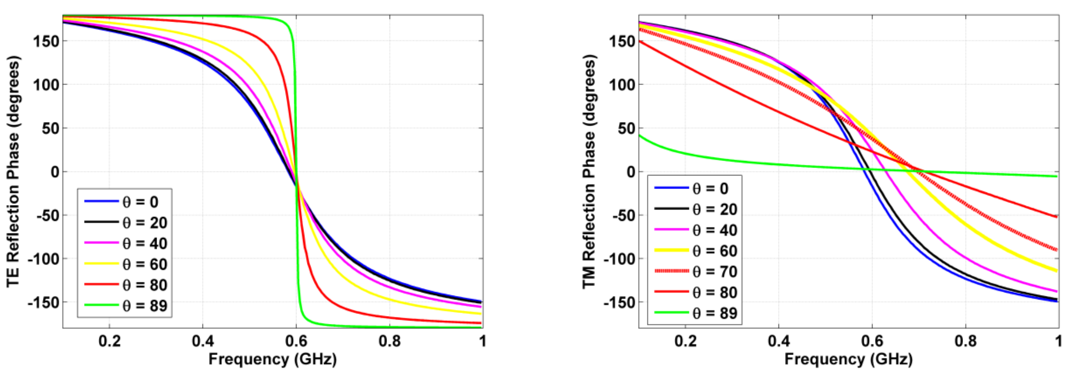

(a) (b)

Figure 7-9: Design 4; (a) TE polarization with varying angles of incidences, (b) TM polarization with varying angles of incidences,.

7.3. WDO Optimization Schema

In Chapter 4, a novel nature-inspired optimization algorithm called Wind Driven Optimization (WDO) was introduced and shown to be very efficient in the design optimization of various electromagnetics problems. Here, the WDO is utilized to optimize the geometry of the ultra-small unit cell artificial magnetic conductors to achieve precise control over the location of the center of the AMC band. For the first design example, the center of the band is targeted to be at 625 MHz, and Design 2 is optimized via WDO. The unit cell dimensions are set to be 0.44 cm with a dielectric thickness of 3.4 cm and relative permittivity of $\varepsilon_r = 2.7 - j0.10$. The optimization is achieved by altering the finger lengths of the extended interdigitated arms, where the reflection phase of the each candidate design was evaluated by the PMoM solver. A simple *Pressure* function is utilized to align the center of the AMC band at the desired frequency, f_{target},

$$Pressure = |\, 1 - R(f_{target})\,| \qquad (7\text{-}1)$$

Lengths of 13 fingers were optimized, where the WDO was allowed to run for a maximum of 100 iterations with a population size of 15 air parcels. Following coefficients were used in the WDO; $\boldsymbol{\alpha} = 0.4$, $\boldsymbol{g} = 0.2$, $\boldsymbol{c} = 0.4$, $\boldsymbol{RT} = 3$, and $\boldsymbol{V_{max}} = \underline{+}\,|0.3|$.

The optimized design geometry is shown in Figure 7-10 (a) where the dashed lines illustrate the boundaries of the unit cell and the lengths of each fingers are altered to achieve the reflection phase center at 625 MHz as seen in Figure 7-10 (b).

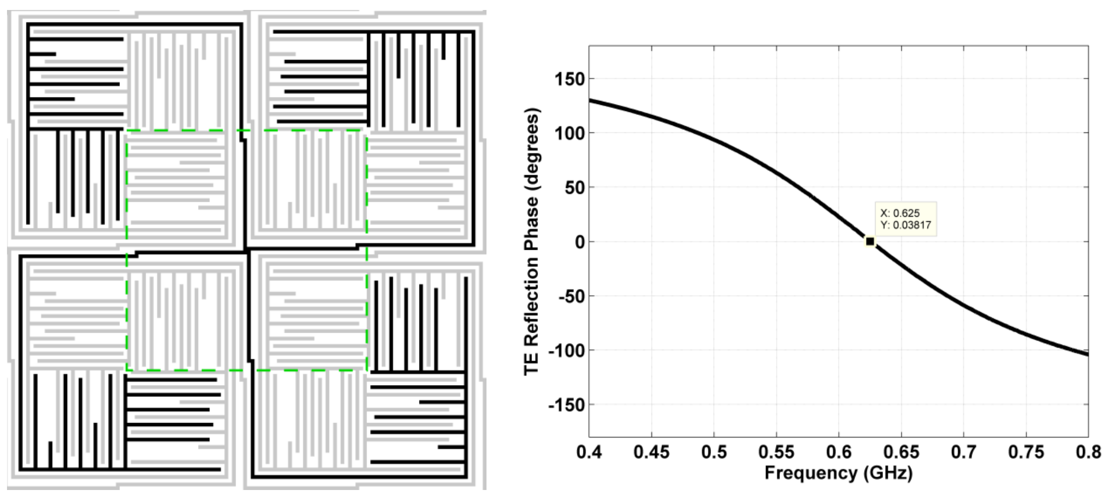

(a) (b)

Figure 7-10: (a) Optimized geometry of the unit cell structure targeting center frequency of 625 MHz, (b) TE reflection phase response over frequency at normal incidence.

For the second design synthesis, the same optimization settings were utilized, where only the target center frequency was changed to f_{target} = 800 MHz. The optimized design geometry is shown in Figure 7-11 (a) and the reflection phase center was achieved at 800 MHz as seen in Figure 7-11 (b).

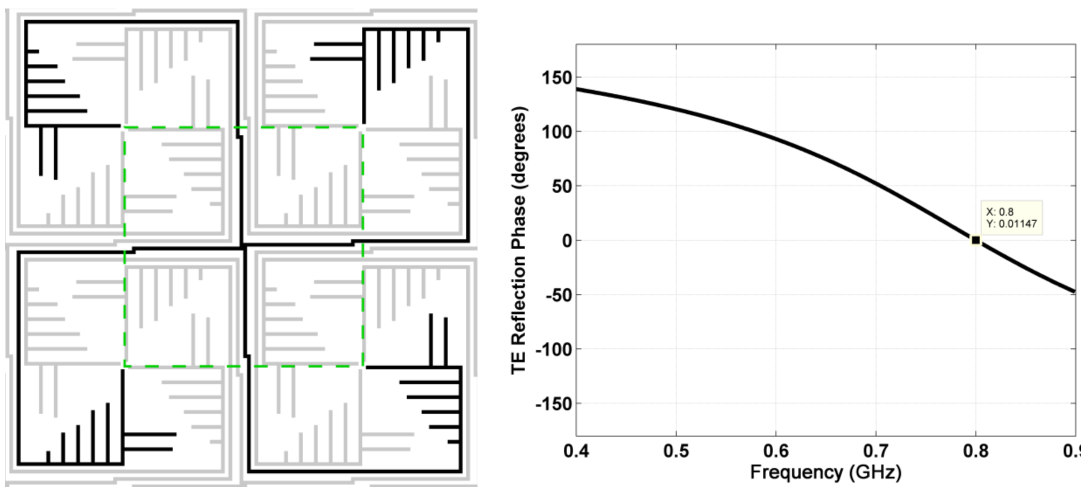

(a) (b)

Figure 7-11: (a) Optimized geometry of the unit cell structure targeting center frequency of 800 MHz, (b) TE reflection phase response over frequency at normal incidence.

7.4. Summary

This chapter introduced a set of new ultra small unit cell artificial magnetic conducting surfaces, and studied their properties numerically. It was shown that the proposed designs provide miniaturization, excellent field of view and identical bandwidth compared to the state-of-the-art AMCs. The WDO optimization schema also discussed and optimization results showed that it is also possible to precisely control the center of the desired operating frequency band.

Chapter 8

Planar EBG Designs for Mutual Coupling Reduction

This chapter introduces a new planar electromagnetic bandgap structure (EBG) for isolation of patch antennas. The proposed design is based on the 90 degrees rotational symmetric unit cell geometry that extends into neighboring unit cells [15]. The planar nature of the proposed EBG structure makes it ideal for planar antenna array applications to achieve increased isolation between neighboring patch antennas.

8.1. EBG designs for Patch Antenna Isolation

Rectangular microstrip antennas, also known as patch antennas, are printed on dielectric materials, or magneto-dielectric substrates, and they provide unique properties such as being low profile and light weight, which are desired for aircraft and space applications. Also, they are simple to design and inexpensive to fabricate along with their ease of integration with other microwave circuitry makes them an active field of continuing research. For integration with microwave circuitry, it is desirable to increase the dielectric permittivity, which leads to tightly bound fields reducing the unwanted radiation and increasing the amount of miniaturization of the elements [110]. However, high permittivity dielectrics come with the reduction in operational bandwidth of the patch antennas as well as unwanted surface wave excitations [16]. In array configuration, the excited surface waves increase the mutual coupling among neighboring antenna elements. To address this problem, the surface wave suppression property of the electromagnetic bandgap structures can be exploited, where EBG unit cells are designed and placed between two antenna array elements, which have a bandgap range coinciding with the operational bandwidth of the patch antennas. In [16], Yang *et al.* designed a simple mushroom type EBG structure utilizing the equations in [112] to reduce the mutual coupling between two planar patch antennas. The geometry of the mushroom type EBG unit cell is illustrated in Figure 8-1 (a) along with the irreducible Brillouin zone of the eight-folded symmetric unit cell (Γ - X - M), where the dispersion diagram is computed numerically via the eigen-solver of the Ansoft HFSS [108, 126] as seen in Figure 8-1 (b). The square unit cell dimensions are 3.5 mm x 3.5 mm (0.067 λ_0) with a 3.0 mm x 3.00 mm square patch printed on a 1.92 mm thick substrate with a relative permittivity of ε_r = 10.2 -*j*0.023. The radius of the metallic via is set to 0.12 mm, which connects the upper square patch to the PEC ground plane.

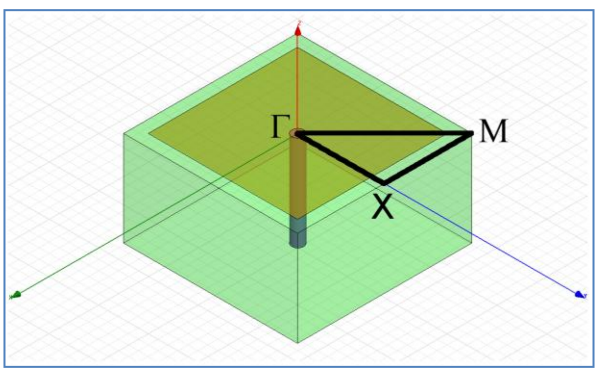

(a)

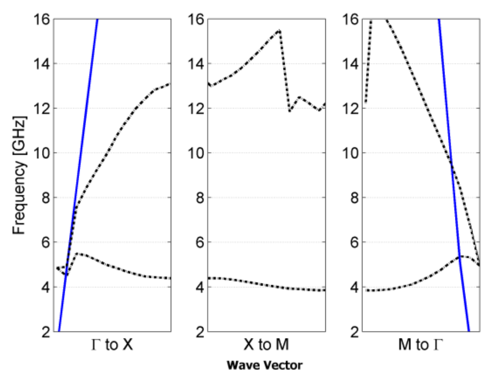

(b)

Figure 8-1: (a) Mushroom type EBG structure geometry shown with the irreducible Brillouin zone shown (Γ - X - M), (b) Dispersion diagram of this mushroom type EBG unit cell is shown where only the first two modes are reproduced by utilizing eigen-solver of the Ansoft HFSS.

These mushroom EBG structures are then placed between two identical patch antennas, which have a resonance coinciding with the bandgap of the EBGs and Yang *et al.* show that the coupling between two antenna element can be reduced up to 10 dB. This design example is reproduced by utilizing the information provided in [16] and simulation setup is illustrated in Figure 8-2, where the achieved isolation improvements can be observed in Figure 8-3.

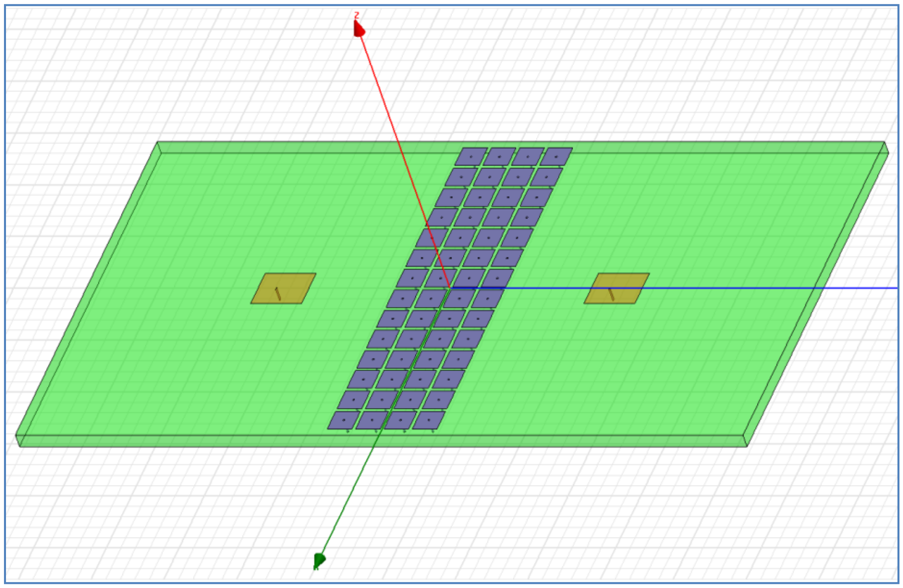

Figure 8-2: Simulation setup for patch antenna isolation via utilization of mushroom type EBG structures, where results are reproduced via finite-element solver of the Ansoft HFSS based on the dimensions provided in [16].

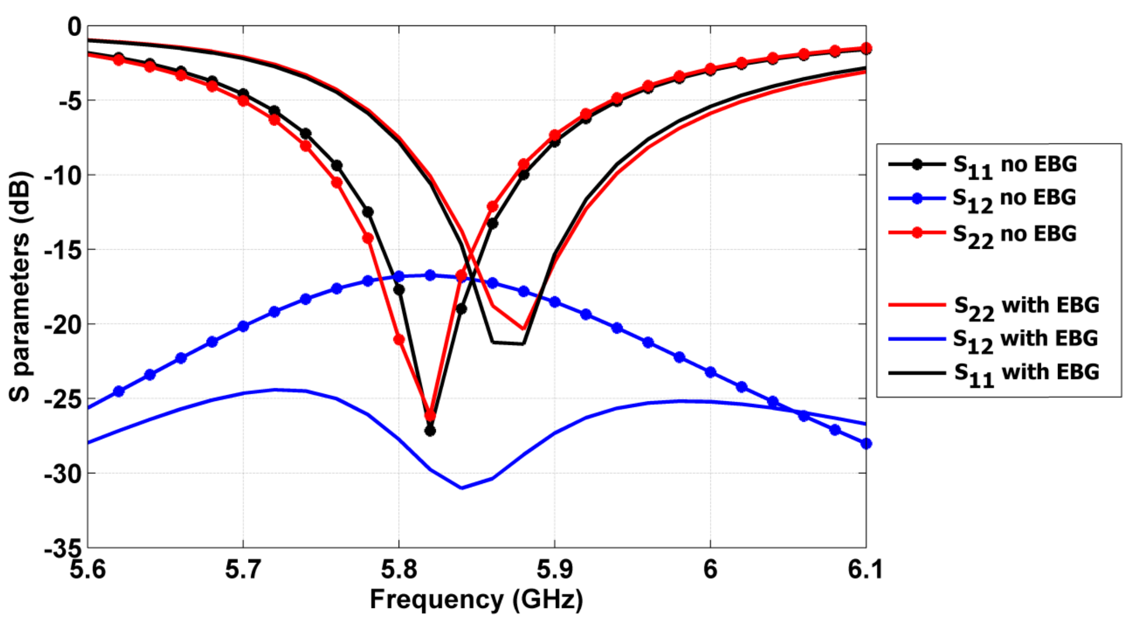

Figure 8-3: Comparison of the S parameters of the two patch antennas, with and without the mushroom type EBGs in between. Results are reproduced from [16]. It can be clearly seen that the S_{12} (mutual coupling) can be reduced significantly within the EBG frequency bandgap.

The wide bandgap of the square mushroom type EBG comes with the drawback of vertical metallic vias, which may lead to fabrication errors thus potentially reduce the performance of the EBG separator. The effect of the via thickness variations on the width of the bandgap is purposefully exploited in [127] and the effect of the via location variations on the bandgap frequency shift is also exploited in a methodical way in [128] to achieve improvements over the conventional design, yet uncontrolled variations in the location and the thickness of the vias could happen during the fabrication process, which may lead to undesired variations in the performance of the EBG.

To simplify the fabrication process and to eliminate any potential problems, a planar EBG unit cell geometry is proposed here, which does not require any vertical connections to the ground plane unlike the mushroom type EBGs. This unit cell design is based on the 90 degrees rotationally symmetric structures [15], where the arms of the unit cell extend into the neighboring unit cells to achieve increased capacitance, and AMC bandwidth, while achieving miniaturized unit cell dimensions. Properties of similar designs were studied in Chapter 7.

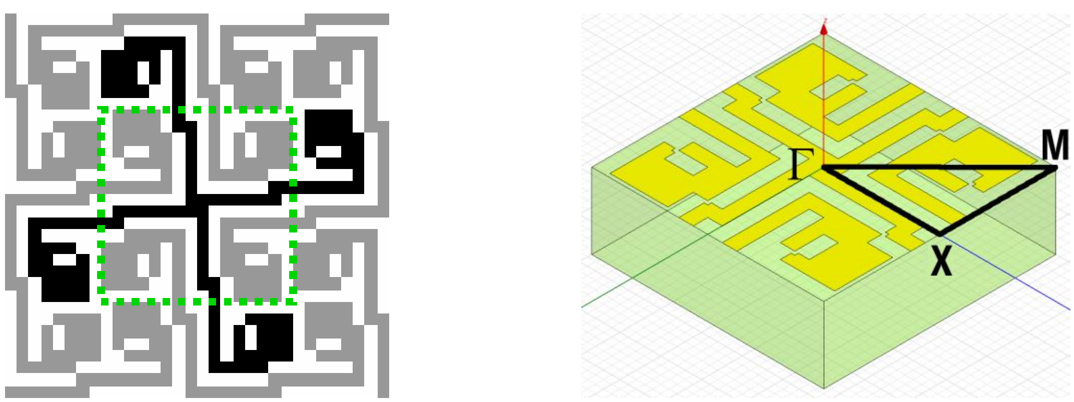

(a) (b)

Figure 8-4: (a) Unit cell geometry of the proposed planar EBG structure, (b) certain section of the Brillouin zone is illustrated, where study of on this section was sufficient to determine the bandgap.

The unit cell dimensions are highlighted with the dashed lines in Figure 8-4 (a) and only a certain section of the Brillouin zone is shown in Figure 8-4 (b). Design is targeting operating frequency of 1.5 GHz. The square unit cell dimensions are 1.423 cm (0.071 λ_0) and printed on a 0.463 cm thick dielectric with a relative permittivity of $\varepsilon_r = 9.42 - j0.0011$.

The dispersion diagram of the proposed planar EBG structure is calculated numerically via the eigen-solver of the Ansoft HFSS and illustrated in Figure 8-5. A very narrow bandgap is supported by this design in the range of [1.447 GHz, 1.452 GHz].

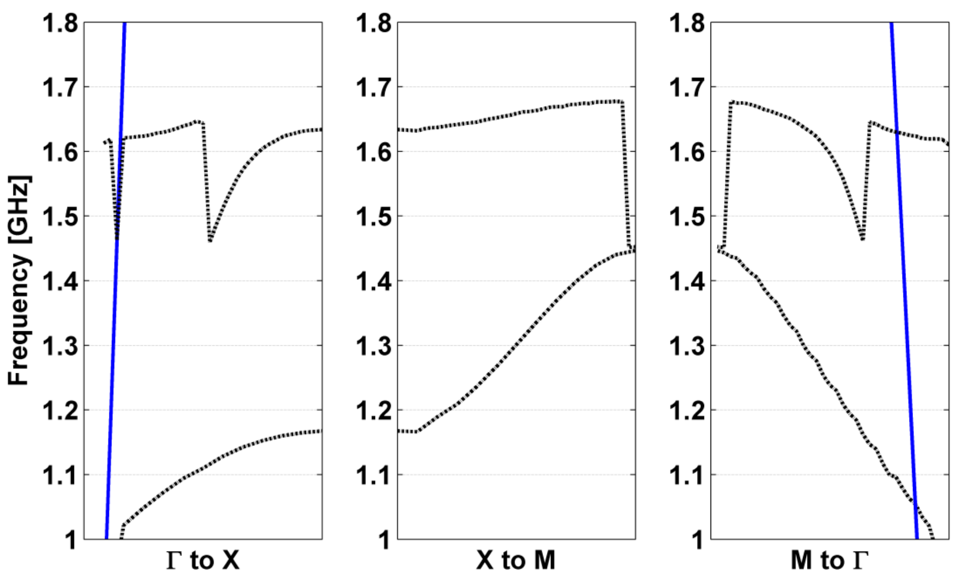

Figure 8-5: Dispersion diagram of the proposed planar EBG structure. A very narrow bandgap is shown in the range of [1.447 GHz, 1.452 GHz].

To confirm the bandgap, and its utility as EBG isolator between two patch antennas, a section of 8 by 10 unit cells are placed between two identical antennas as illustrated in Figure 8-6. The antennas are designed to resonate within the frequency range of the bandgap as shown by the

S-parameters in Figure 8-7 (a). The square dimensions of the patch antenna is 31.2 mm on a single edge and the separation between two antennas is 0.75 λ_0. The EBGs and the antennas are printed on a 0.463 cm thick dielectric with relative permittivity of $\varepsilon_r = 9.42 -j0.0011$. The total length of the dielectric slab and the ground plane is 24.191 cm by 39.744 cm, which corresponds to the same footprint of 17 by 28 unit cell sizes.

The effect of the EBG unit cells on the mutual coupling reduction between two antennas can be observed in Figure 8-7 (b), where the bandgap is illustrated with the yellow lines. S_{11} and S_{22} seem to shift to a higher frequency, yet, still with a good input impedance at the 1.45 GHz. On the other hand, there is significant reduction in the mutual coupling as shown with the reduction in S_{12} in Figure 8-7 (b). At the lower edge of the bandgap, at 1.447 GHz, S_{12} reduces 12 dB and at the higher edge of the bandgap, 1.452 GHz, S_{12} reduces 4.4 dB.

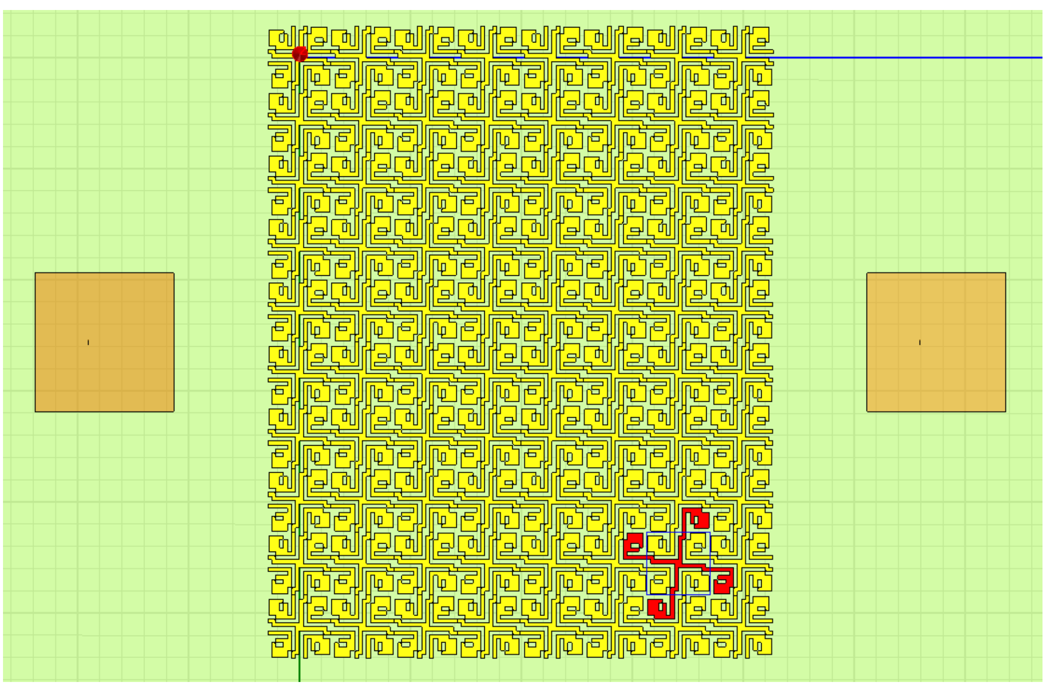

Figure 8-6: Simulation setup to illustrate utility of the proposed EBG unit cell between two patch antennas to reduce the mutual coupling. Simulations are carried out in Ansoft HFSS.

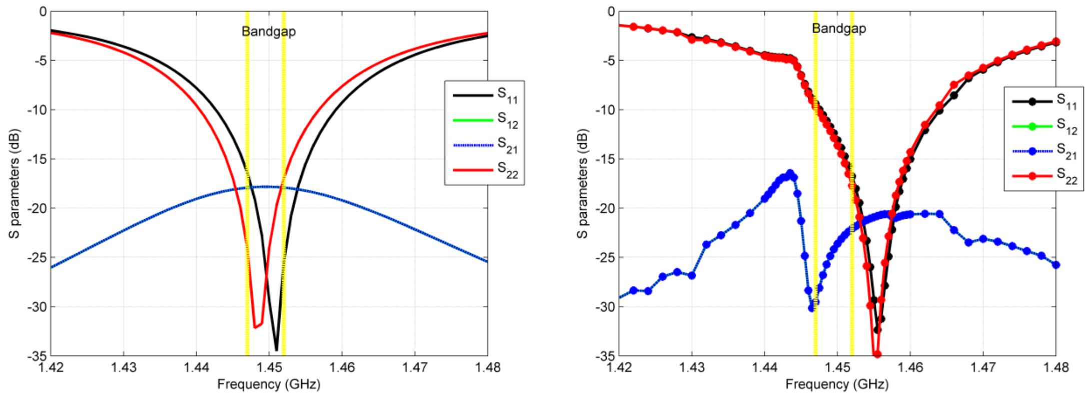

(a) (b)

Figure 8-7: (a) S parameters of the two patch antennas resonating at around 1.45 GHz. There is no EBG between two patch antennas, (b) S parameters of the same patch antennas with the proposed EBG unit cells in between as illustrated in Figure 8-6.

8.2. Summary

In this chapter, the surface wave suppression property of the mushroom type EBG structures were revisited and a novel planar electromagnetic bandgap structure (EBG) for isolation of patch antennas was introduced. The proposed design is based on the 90 degrees rotational symmetric unit cell geometry that extends in to neighboring unit cells [15]. The dispersion diagram study showed a narrow bandgap at around 1.45 GHZ, and the effectiveness of the proposed planar EBG was illustrated with two planar patch antenna array applications to achieve increased isolation between them. Although the bandgap is narrower, all planar nature of the geometry makes the fabrication processes much simpler reducing the chance in fabrication errors hence possible performance problems of EBGs.

Chapter 9

Conclusions and Future Work

9.1. Conclusions

One of the two research branches presented in this dissertation has demonstrated advancements in the design synthesis of novel metamaterial surfaces targeting different applications including improvements on existing artificial magnetic conducting surfaces as well as introducing novel methods to design double-sided AMCs, matched impedance magneto-dielectric surfaces, frequency selective surfaces, and planar electromagnetic bandgap structures targeting both antenna applications and absorber applications.

Some of the work presented as improvements of existing state-of-the-art methods, such as the synthesis of ultra-small unit cell size 90 degrees rotational symmetric intertwining unit cell designs those provide exceptional performance for the achieved miniaturization levels. Combining this method with a numerical optimizer also provides precise control of the center of the band without altering any of the design dimensions giving significant control to the designer. Similarly, utilizing the small unit cell rotationally symmetric structures as planar electromagnetic bandgap material to reduce mutual coupling of microstrip patch antenna arrays can also be considered as an advancement on existing planar technology where mushroom type EBGs require more complicated fabrication methods and are prone to fabrication errors.

In addition, novel metamaterial techniques are also proposed, studied and implemented, such as the thin planar double-sided AMC ground planes and separators. While these novel ground planes provide flexibility to composite antenna systems, highly optimized DSAMC separators are shown to be very effective when used with vertical antennas in the WiFi frequency ranges.

A novel method to synthesize matched-impedance ($\mu_r = \varepsilon_r > 1$) magneto-dielectric metamaterial (MIMDM) is proposed and optimized for applications at single and multiple frequencies, which can be easily utilized as substrates beneath patch antennas, and provide increased miniaturization. Both double-positive and double-negative constitutive parameter materials are designed and provided as planar alternatives to similar materials with embedded *LC* resonator elements.

Absorber applications are also addressed where slight modifications to the DSAMCs and MIMDMs provided efficient absorbers either in composite systems or wide field of views with much smaller unit cell sizes compared to current literature.

As the other branch of the research presented here, numerical optimization algorithms are studied, a novel implementation to an existing algorithm is proposed in the case of Parallel Clonal Selection Algorithm as well as a brand new nature-inspired optimization algorithm is invented and proved to be efficient optimization tool for electromagnetic design problems as illustrated with the Wind Driven Optimization algorithm.

9.2. Future Work

This research has demonstrated various advancements both in numerical optimization methods and both design synthesis of novel electromagnetic surfaces, yet with any research, there is always room for improvements and for new ideas to thrive from the work presented.

Based on the presented work, following topics may be considered as future areas of research:

- Application of the Wind Driven Optimization algorithm to wider range of optimization problems with more complex search topologies.
- Hybridization of the WDO with other statistical methods to overcome any drawbacks that comes with the operators of the algorithm or to improve the current state of performance.
- Establishing a convenient method to link the AMC band of a planar design with its frequency bandgap so that optimization schema could be simplified.
- Further research into improving narrow frequency bandgap of rotationally symmetric unit cell designs.
- Continuing evaluation of MIMDMs and their applications for planar antennas to improve the gain, bandwidth and miniaturization.
- Further study of double-sided AMCs with embedded LC resonators to achieve tunability.

Bibliography

1. M. K. Ozdemir, E. Arvas, and H. Arslan, "Dynamics of spatial correlation and implications on MIMO systems," *IEEE Commun. Mag.*, vol. 42, no. 6, pp. S14 – S19, June 2004.

2. A. Erentok, P. L. Luljak, and R. W. Ziolkowski, "Characterization of a volumetric metamaterial realization of an artificial magnetic conductor for antenna applications," *IEEE Trans. Antennas and Propag.*, vol. 53, no. 1, pp. 160-172, Jan. 2005.

3. K. J. Vinoy, and R. M. Jha, *Radar Absorbing Materials: From Theory to Design and Characterization*, Boston, MA: Kluwer, 1996.

4. L. H. Hemming, *Electromagnetic Anechoic Chambers: A Fundamental Design and Specification Guide,* Piscataway, NJ, IEEE Press, 2002.

5. R. L. Haupt, and D. H. Werner, *Genetic Algorithms in Electromagnetics*, Wiley-IEEE Press, Hoboken, New Jersey, April 2007.

6. J. Kennedy and R. Eberhart, "Particle swarm optimization," *Proc. Ninth Int. Conf. on Neural Networks*, vol. 4, pp. 1942-1948, Nov. 1995.

7. Z. Bayraktar, M. Komurcu, and D. H. Werner, "Wind driven optimization (WDO): a novel nature-inspired optimization algorithm and its application to electromagnetics," *Proc. 2010 IEEE Int. Symp. Antennas and Propag. and CNC/USNC/URSI Radio Science Meeting,* Toronto, Ontario, Canada, July 11-17, 2010.

8. D. Sievenpiper, L. Zhang, Romulo F. J. Broas, N. G. Alexopolous and E. Yablonovitch, "High-impedance electromagnetic surfaces with a forbidden frequency band," *IEEE Trans. Microw. Theory and Tech.*, vol. 47, no. 11, pp. 2059 – 2074, Nov. 1999.

9. K-P. Ma, K. Hirose, F-R. Yang, Y. Qian, and T. Itoh, "Realisation of magnetic conducting surface using novel photonic bandgab structure," *IEE Electronics Letters*, vol. 34, no. 21, pp. 2041-2042, 15th Oct. 1998.

10. Z. Bayraktar**,** J. Bossard and D. H. Werner, "AMC metamaterials for low profile antennas mounted on or embedded in composite platforms," *Proc. 2007 Antennas and Propag. Soc. Int. Symp.*, Honolulu, Hawaii, USA, pp. 1305-1308, June 10-15, 2007.

11. Z. Bayraktar, M. Gregory, and D. H. Werner, "Composite planar double-sided AMC surfaces for MIMO applications," *Proc. 2009 IEEE Int. Symp. on Antennas and Propag. and USNC/URSI National Radio Science Meeting*, Charleston, SC, USA, June 1-5, 2009.

12. D. J. Kern, D. H. Werner, and M. Lisovich, "Metaferrites: using electromagnetic bandgap structures to synthesize metamaterial ferrites," *IEEE Trans. Antennas and Propag.*, vol. 53, no. 4, pp.1382 - 1389, April 2005.

13. Z. Bayraktar, M. Gregory, D. Kern, and D. H. Werner, "Matched impedance thin composite

magneto-dielectric metasurfaces," *Proc. 2009 IEEE Int. Symp. on Antennas and Propag. and USNC/URSI National Radio Science Meeting*, Charleston, SC, USA, June 1-5, 2009.

14. D. J. Kern, D. H. Werner, A. Monorchio, L. Lanuzza, and M. J. Wilhelm, "The design synthesis of multi-band artificial magnetic conductors using high impedance frequency selective surfaces," *IEEE Trans. Antennas and Propag.*, Special Issue on Artificial Magnetic Conductors, Soft/Hard Surfaces, and other Complex Surfaces, vol. 53, no. 1, pp. 8-17, January 2005.

15. A. Monorchio, S. Genovesi, E. Carrubba, and G. Manara, "Design of printed FSS for compact and bandwidth-enhanced metasurfaces," *Proc. 2007 Metamaterials Symposium*, pp. 811-814, Oct. 2007.

16. F. Yang, and Y. Rahmat-Samii, "Microstrip antennas integrated with electromagnetic band-gap (ebg) structures: a low mutual coupling design for array applications," *IEEE Trans. on Antennas and Propag.*, vol. 51, no. 4, pp. 2936 - 2946, Oct. 2003.

17. Z. Bayraktar, and D. H. Werner, "Ultra-small unit cell artificial magnetic conductor synthesis," in preparation for publication in the *IEEE Antennas and Wireless Propagation Letters*.

18. Z. Bayraktar, M. Komurcu, and D. H. Werner, "Wind driven optimization technique in electromagnetics," in preparation for publication in the *IEEE Trans. Antennas and Propag*.

19. Z. Bayraktar, M. D. Gregory, and D. H. Werner, "Thin composite planar double-sided high-impedance surfaces and their applications," in preparation for publication in the *IEEE Trans. Antennas and Propag*.

20. Z. Bayraktar, J. A. Bossard, X. Wang, and D. H. Werner, "A real-valued parallel clonal selection algorithm and its application to design optimization of multi-layered frequency selective surface filters," submitted for publication in the *IEEE Trans. Antennas and Propag*.

21. Z. Bayraktar, M. D. Gregory, X. Wang, and D. H. Werner, "Matched impedance thin planar composite magneto-dielectric metasurfaces," submitted for publication in the *IEEE Trans. Antennas and Propag*.

22. Z. Bayraktar, Z. H. Jiang, D. H. Werner and P. L. Werner, "Stub-loaded inverted-F antenna Synthesis via Wind Driven Optimization," accepted for publication in the *2011 IEEE Int. Symp. on Ant. and Propag. and USNC/URSI National Radio Sci. Meeting, July 3-8, 2011, Spokane, WA, USA.*

23. Z. Bayraktar, J. A. Bossard, X. Wang, and D. H. Werner, "Real-valued parallel clonal selection algorithm for design optimization in electromagnetics," *Proc. of the 2010 IEEE Int. Symp. on Ant. and Propag. and CNC/USNC/URSI National Radio Sci. Meeting*, Toronto, Ontario, Canada, July 11-17, 2010.

24. Z. Bayraktar, X. Wang, and D. H. Werner, "Thin composite matched impedance magneto-dielectric metamaterial absorbers," *Proc. of the 2010 IEEE Int. Symp. on Ant. and Propag. and CNC/USNC/URSI National Radio Sci. Meeting*, Toronto, Ontario, Canada, July 11-17, 2010.

25. J. H. Holland, *Adaptation in Natural and Artificial Systems*, University of Michigan Press, Ann Arbor, 1975.

26. A. J. F. Griffiths, S. R. Wessler, R. C. Lewontin, W. M. Gelbart, D. T. Suzuki, and J. H. Miller, *Introduction to Genetic Analysis*, 8th ed., W. H. Freeman and Company, New York, 2004.

27. R. L. Haupt, and S. E. Haupt, *Practical Genetic Algorithms*, 2nd ed., Wiley, New York, 2004.

28. B. Tian, Z. Li, and C. Wang, "Boresight gain optimization of an UWB monopole antenna using FDTD and genetic algorithm," *IEEE Int. Conf. Ultra-Wideband (ICUWB)*, vol. 1, pp. 1-4, 20-23 Sept. 2010.

29. E. E. Altshuler, "Design of a vehicular antenna for GPS/Iridium using a genetic algorithm," *IEEE Trans. Antennas and Propag.*., vol. 48, no. 6, pp. 968-972, June 2000.

30. X. Chen, K. Huang, and X.-B. Xu, "Automated design of a three-dimensional fishbone antenna using parallel genetic algorithm and NEC," *IEEE Antennas Wireless Propag. Lett.*, vol. 4, pp. 425 428, 2005.

31. E. E. Altshuler, and D. S. Linden, "Wire-antenna designs using genetic algorithms," *IEEE Antennas and Propag. Mag.*, vol. 39, no. 2, pp. 33-43, Apr 1997.

32. T. D. Nguyen, T. P. Vuong, Y. Duroc, and V. Y. Vu, "Optimization of PIFA antenna using an auto-embedded genetic algorithm," *Third Int. Conf. on Comm. and Electronics (ICCE)*, pp. 367 372, 11-13 Aug. 2010.

33. T. G. Spence, and D. H. Werner, "A novel miniature broadband/multiband antenna based on an end-loaded planar open-sleeve dipole," *IEEE Trans. on Antennas and Propag.*, vol.54, no.12, pp. 3614-3620, Dec. 2006.

34. T. G. Spence, and D. H. Werner, "Design of broadband planar arrays based on the optimization of aperiodic tilings," *IEEE Trans. on Antennas and Propag.*, vol.56, no.1, pp. 76-86, Jan. 2008.

35. L.-F. Tuen, and C.-L. Li, "Design and optimization for the satellite Ku-band CP array antennas," *2010 Int. Conf. Applications of Electromagnetism and Student Innovation Competition Awards (AEM2C)*, pp. 274-278, 11-13 Aug. 2010.

36. J. M. Johnson, and Y. Rahmat-Samii, "Genetic Algorithms in Engineering Electromagnetics," *IEEE Antennas and Propag. Mag.*, vol. 39, no. 4, pp. 7-21, 1997.

37. M. G. Bray, D. H. Werner, D. W. Boeringer, and D. W. Machuga, "Optimization of thinned aperiodic linear phased arrays using genetic algorithms to reduce grating lobes during scanning," *IEEE Trans. Antennas and Propag.*, vol.50, no.12, pp. 1732- 1742, Dec 2002.

38. E. Michielssen, J.-M Sajer, S. Ranjithan, and R. Mitra, "Design of lightweight, broad-band microwave absorbers using genetic algorithms," *IEEE Trans. Microw. Theory Tech.*, vol.41, no.6, pp.1024-1031, Jun/Jul 1993.

39. S. Cui, D. S. Weile, and J. L. Volakis, "Novel planar electromagnetic absorber designs using genetic algorithms," *IEEE Trans. Antennas and Propag.*, vol. 54, no. 6, pp. 1811-1817, June 2006.

40. D. S. Weile, E. Michielssen, and D. E. Goldberg, "Genetic algorithm design of Pareto optimal broadband microwave absorbers," *IEEE Trans. Electromagn. Compat.*, vol. 38, no. 3, pp. 518-525, Aug. 1996.

41. S. W. Han, Y. S. Park, and D. P. Neikirk, "Broadband infrared detection using Jaumann absorbers with genetic algorithm," *Electronics Letters*, vol. 41, no. 24, pp. 1307-1308, 24 Nov. 2005.

42. G. Manara, A. Monorchio, and R. Mittra, "Frequency selective surface design based on genetic algorithm," *Electronics Letters* , vol. 35, no. 17, pp.1400-1401, 19 Aug. 1999.

43. J. A. Bossard, X. Liang, L. Li, S. Yun, D. H. Werner, D. Weiner, T. S. Mayer, P. F. Cristman, A. Diaz, and I. C. Khoo, "Tunable frequency selective surfaces and negative-zero-positive index metamaterials based on liquid crystals," *IEEE Trans. Antennas and Propag.*, vol. 56, no. 5, pp. 1308-1320, May 2008.

44. E. Michielssen, J. M. Sajer, and R. Mittra, "Design of multi-layered FSS and waveguide filters using genetic algorithms," *IEEE AP-S Symposium Digest*, Ann Arbor, MI, pp. 1936-1939, 28 June-2 July 1993.

45. J. A. Bossard, D. H. Werner, T. S. Mayer, J. A. Smith, Y. U. Tang, R. P. Drupp, and L. Li, "The design and fabrication of planar multiband metallodielectric frequency selective surfaces for infrared applications," *IEEE Trans. Antennas and Propag.*, vol. 54, no. 4, pp. 1265-1276, April 2006.

46. L. Akhoondzadeh-Asl, D. J. Kern, P. S. Hall, and D. H. Werner, "Wideband dipoles on electromagnetic bandgap ground planes," *IEEE Trans. Antennas and Propag.*, vol.55, no.9, pp.2426-2434, Sept. 2007.

47. J. Yeo, R. Mittra, and S. Chakravarty, "A GA-based design of electromagnetic bandgap (EBG) structures utilizing frequency selective surfaces for bandwidth enhancement of microstrip antennas," *IEEE AP-S Symposium*, vol.2, pp. 400-403, 2002.

48. D. J. Kern, and D. H. Werner, "Ultra-thin electromagnetic bandgap absorbers synthesized via genetic algorithms," *IEEE AP-S Symposium*, vol.2, pp. 1119-1122, 22-27 June 2003.

49. D-H. Kwon, and D. H. Werner, "Synthesis of zero-index metamaterial slabs using genetic algorithms," *IEEE AP-S Symposium*, pp.2229-2232, 9-15 June 2007.

50. E. Hart, and J. Timmis, "Application areas of AIS: the past, the present and the future," *Appl. Soft Comput.*, vol. 8, no. 1, pp. 191 - 201, Elsevier Science Publishers, 2008.

51. X.-R. Yang, J.-Y. Shen, and R. Wang, "Artificial immune theory based network intrusion detection system and the algorithms design," *Proc. of the 2002 Int. Conf. on Machine Learning and Cybernetics*, vol. 1, pp. 73- 77, 2002.

52. D.-W. Lee, and K.-B. Sim, "Artificial immune network-based cooperative control in collective autonomous mobile robots," *Proc. of the 6th IEEE Int. Workshop on Robot and Human Communication*, pp. 58-63, Sep. 29 - Oct. 1, 1997.

53. V. K. Karakasis, and A. Stafylopatis, "Data mining based on gene expression programming and clonal selection," *Proc. of the 2006 IEEE Congress on Evol. Comput.*, pp. 514-521, July 16-21, 2006.

54. Z. Chen, "Data mining based on clonal selection wavelet network," *Proc. of the Eighth ACIS Int.*

Conf. on Software Engineering, Artificial Intelligence, Networking, and Parallel/Distributed Computing, vol. 3, pp. 665-669, July 30 - Aug. 1, 2007.

55. L. N. de Castro, and F. J. von Zuben, "Learning and optimization using the clonal selection principle," *IEEE Trans. Evol. Comput.*, vol. 6, no. 3, pp. 239 - 251, June 2002.

56. L. N. de Castro, and F. J. von Zuben, *Recent Developments in Biological Inspired Computing*, IDEA Group Publishing, 2005.

57. F. Campelo, F. G. Guimaraes, H. Igarashi, and J. A Ramirez, "A clonal selection algorithm for optimization in electromagnetics," *IEEE Trans. Magnet.*, vol. 41, no. 5, May 2005.

58. F. G. Guimaraes, F. Campelo, R. R. Saldanha, H. Igarashi, R. H. C. Takahashi, and J. A. Ramirez, "A multiobjective proposal for the team benchmark problem 22," *IEEE Trans. Magnet.*, vol. 42, no. 4, April 2006.

59. F. Campelo, F. G. Guimaraes, J. A Ramirez, and H. Igarashi, "Optimization in electromagnetics using the real-coded clonal selection algorithm," *IEEE Conf. on Soft Comp. in Industrial Applications*, pp. 89-94, June 25-27, 2008.

60. L. Batista, F. G. Guimaraes, and J. A. Ramirez, "A distributed clonal selection algorithm for optimization in electromagnetics," *IEEE Trans. Magnet.*, vol. 45, no. 3, March 2009.

61. L. S. Batista, D. B. Oliveira, F. G. Guimaraes, E. J. Silvia, and J. A. Ramirez, "Dynamic multiobjective clonal selection algorithm for engineering design," *IEEE Trans. Magnet.*, vol. 46, no. 8, Aug. 2010.

62. Y. Ke, L. Jiao, and W. Zhou, "Channel estimation based on clonal selection algorithm in MIMO systems," *Proc. of the Int. Conf. on Computational Intellig. and Security*, pp. 406-409, Nov. 2006.

63. B. Babayigit, A. Akdagli, and K. Guney, "A clonal selection algorithm for null synthesizing of linear antenna arrays by amplitude control," *J. of Electromagn. Waves and Appl.*, vol. 20, pp. 1007-1020, 2006.

64. A. Akdagli, K. Guney, and B. Babayigit, "Clonal selection algorithm for design of reconfigurable antenna array with discrete phase shifters," *J. of Electromagn. Waves and Appl.*, vol. 21, no. 2, pp. 215-227, 2007.

65. K. Guney, B. Babayigit, and A. Akdagli, "Position only pattern nulling of linear antenna array by using a clonal selection algorithm (clonalg)," *Springer Electrical Engineering*, vol. 90, no. 2, pp. 147-153, 2007.

66. B. A. Munk, *Frequency Selective Surfaces: Theory and Design*. New York: Wiley, 2000.

67. D. J. Kern, and D. H. Werner, “A genetic algorithm approach to the design of ultra-thin electromagnetic bandgap absorbers,” *Microwave Opt. Technol. Lett.*, vol. 38, no. 1, pp. 61-64, Jul. 2003.

68. J. A. Bossard, S. Yun, D. H. Werner, and T. S. Mayer, “Synthesizing low loss negative index metamaterial stacks for the mid-infrared using genetic algorithms,” *Opt. Expr.*, vol. 17, no. 17, pp. 14771-14779, Aug. 2009.

69. J. A. Bossard, D. H. Werner, T. S. Mayer, and R. P. Drupp, “A novel design methodology for reconfigurable frequency selective surfaces using genetic algorithms,” *IEEE Trans. Antennas Propag.*, vol. 53, no. 4, pp. 1390-1400, Apr. 2005.

70. D. L. Carroll, *FORTRAN Genetic Algorithm (GA) Driver*. [Online]. Available: http://cuaerospace.com/carroll/ga.html

71. R. Coico, G. Sunshine, and E. Benjamine, *Immunology: A Short Course*, Wiley-Liss, 5th ed., 2003.

72. A. M. Silverstein, *A History of Immunology*, 2nd ed., Elsevier, 2009.

73. F. M. Burnet, *The Clonal Selection Theory of Acquired Immunity*, Cambridge, U.K., Cambridge Univ. Press, 1959.

74. T. R. Bowry, *Immunology Simplified*, Oxford Medical Publications, 1977.

75. V. Cutello, G. Nicosia, and M. Pavone, "Real coded clonal selection algorithm for unconstrained global optimization using a hybrid inversely proportional hypermutation operator," *Proc. of the 2006 ACM Symp. on Applied Computing*, pp. 950 - 954, 2006.

76. T. F. Eibert, J. L. Volakis, D. R. Wilton, and D. R. Jackson, “Hybrid FE/BI modeling of 3-D doubly periodic structures utilizing triangular prismatic elements and an MPIE formulation accelerated by the Ewald transformation,” *IEEE Trans. Antennas Propag.*, vol. 47, no. 5, pp. 843-850, May 1999.

77. R. C. Eberhart, Y. Shi, and J. Kennedy, *Swarm Intelligence*, Morgan Kaufmann, 2001.

78. M. Dorigo, and T. Stutzle, *Ant Colony Optimization*, MIT Press, 2004.

79. K. Price, R. M. Storn, and J. A. Lampinen, "*Differential Evolution: A Practical Approach to Global Optimization*," Springer-Verlag Berlin, 2005.

80. N. Hansen, S. D. Müller, and P. Koumoutsakos, “Reducing the time complexity of the derandomized evolution strategy with covariance matrix adaptation (CMA-ES),” *Evolutionary Computation*, vol. 11, no. 1, pp. 1–18, 2003.

81. R. D. Thompson, *Atmospheric Processes and Systems*, Routledge, New York, 1998.

82. NASA Jet Propulsion Laboratory. The Layer's of Earth's Atmosphere. [Online]. Available: http://airs.jpl.nasa.gov/maps/satellite_feed/atmosphere_layers/

83. H. Riehl, *Introduction to the Atmosphere*, McGraw Hill, 1978.

84. C. D. Ahrens, *Meteorology Today: An Introduction to Weather, Climate, and the Environment*, 7th ed., Thomson –Brook/Cole, 2003.

85. Wikipedia. Pressure Gradient. [Online]. Available: http://en.wikipedia.org/wiki/Pressure_gradient

86. J. M. Wallace and P. V. Hobbs, *Atmospheric Science: An Introductory Survey*, 2nd ed., Elsevier, 2006.

87. M. L. Salby, *Fundamentals of Atmospheric Physics*, Academic Press, 1995.

88. R. B. Stull, *Meteorology for Scientists and Engineers*, 2nd ed., Brooks Cole, 1999.

89. P. R. Bannon, *The Dynamic Atmosphere, A Theoretical Perspective*. Class notes for Intro. Atmospheric Dynamics, Department of Meteorology, The Pennsylvania State University, 2003.

90. J. Robinson, and Y. Rahmat-Samii, "Particle swarm optimization in electromagnetics," *IEEE Trans. Antennas and Propag.*, vol. 52, No. 2, pp. 397-407, Feb. 2004.

91. X. Yao, Y. Liu, and G. Lin, "Evolutionary programming made faster," *IEEE Trans. Evol. Comp.*, vol. 3, no. 2, pp. 82 - 102, July 1999.

92. M. M. Khodier, and C. G. Christodoulou, "Linear array geometry synthesis with minimum sidelobe level and null control using particle swarm optimization," *IEEE Trans. Antennas and Propag.*, vol. 53, no. 8, pp. 2674-2679, Aug. 2005.

93. D. W. Boeringer, and D. H. Werner, "Particle swarm optimization versus genetic algorithm for phased array synthesis," *IEEE Trans. Antennas and Propag.*, vol. 52, no. 3, pp.771-779, Mar. 2004.

94. W.-C. Weng, F. Yang, and A. Z. Elsherbeni, "Linear antenna array synthesis using taguchi's method: a novel optimization technique in electromagnetics," *IEEE Trans. Antennas and Propag.*, vol. 55, no. 3, pp. 723-730, Mar. 2007.

95. K.-K. Yan, and Y. Lu, "Sidelobe reduction in array-pattern synthesis using genetic algorithm," *IEEE Trans. Antennas and Propag.*, vol. 45, no. 7, pp. 1117-1122, Jul. 1997.

96. C. Lin, A. Qing, and Q. Feng, "Synthesis of unequally spaced antenna arrays by using differential evolution," *IEEE Trans. Antennas and Propag.*, vol. 58, no. 8, pp. 2553-2561.

97. SuperNEC. Design Curves for an Inverted F Antenna (IFA). Dec. 2010. [Online]. Available: http://www.supernec.com/ifa.htm

98. H. Nakano, R. Suzuki, and J. Yamauchi, "Low-profile inverted-F antenna with parasitic elements on an infinite ground plane," *Proc. of the IEE Microwaves, Antennas and Propagation*, vol. 145, Issue: 4, pp. 321 - 325, Aug. 1998.

99. J. Tie-hua, S. Dong-lin, D. Ke-kia, W. Guo-yu, and Z. Yan, "Design of the low-profile inverted-F antenna with multi-parasitic elements," *Proc. of the 7th Int. Symp. on Antennas, Propagation and EM Theory*, 26-29 Oct. 2006.

100. S. Schulteis, C. Waldschmidt, C. Kuhnert, and W. Wiesbeck, "Design of a capacitively loaded inverted F antenna for wireless-LAN applications," *Proc. of the Int. ITG Conf. on Antennas*, 17-19 Sep. 2003.

101. D. K. Karmokar, K. M. Morshed, A. Md. Numan-Al-Mobin, and A. N. M. E. Kabir, "High gain multiband loaded inverted-F antennas for mobile WiMAX, Wi-Fi, Bluetooth, and WLAN operation," *Int. Journal of Engineering*, vol. 4, no. 3, pp. 219 - 232, 08 Oct. 2010.

102. M. Kim, and H. Arai, "Low-profile loop-shaped inverted-F wire antenna with dualmode operation," *Proc. of the 2007 IEEE Region 10 Conf.*, Oct 20 - Nov. 2, 2007.

103. P. L. Werner, Z. Bayraktar, B. Rybicki, D. H. Werner, K. Schlager, and D. Linden, "Stub-loaded long-wire monopoles optimized for high gain performance," *IEEE Trans. Antennas and Propag.*, vol. 56, no. 3, pp. 639 - 644, Mar. 2008.

104. Z. Bayraktar, P. L. Werner, and D. H Werner, "Reconfigurable high-gain stub-loaded monopoles," *Proc. of the 2008 IEEE Int. Symp. on Antennas and Propag. and USNC/URSI National Radio Science Meeting* in San Diego, USA on July 5-12, 2008.

105. D. J. Kern, D. H. Werner, and P. L. Werner, "Optimization of multi-band AMC surfaces with magnetic loading," *Proc. of the IEEE Antennas Propag. Intl. Symp.*, vol. 1, pp. 823–826, June 2004.

106. P. J. Ferrer, J. M. Gonzalez-Arbesu, and J. Romeu, "Decorrelation of two closely spaced antennas with a metamaterial AMC surface," *IEEE Microwave and Optical Technology Letters*, Vol. 50, No. 5, pp. 1414–1417, May 2008.

107. M. M. Bait-Suwailam, M. S. Boybay, and O. M. Ramahi, "Electromagnetic coupling reduction in high-profile monopole antennas using single-negative magnetic metamaterials for MIMO applications," *IEEE Trans. Antennas and Propag.*, vol. 58, no. 9, pp. 2894–2902, Sep. 2010.

108. HFSS. 3D Full-wave EM Field Simulations. Ansoft [Online]. Version 12.1. Available: http://www.ansoft.com/products/hf/hfss/

109. Advanced Circuit Materials Division High Frequency Laminates and Flexible Circuit Materials Datasheet. Rogers Corporation [Online]. Available: http://www.rogerscorporation.com/acm/hfproductselector.htm

110. C. A. Balanis, *Antenna Theory: Analysis and Design*, 2nd Ed. Wiley, 1996.

111. N. Jin, and Y. Rahmat-Samii, "Particle swarm optimization of miniaturized quadrature reflection phase structure for low-profile antenna applications," *IEEE APS Int. Symp. Dig.*, vol. 2B, pp. 225 8, July 2005.

112. F. Yang, and Y. Rahmat-Samii, *Electromagnetic Band Gap Structures in Antenna Engineering*, Cambridge University Press, 2009, p. 118.

113. CST Microwave Studio. 3D Full-wave EM Field Simulations. CST [Online]. Available : http://www.cst.com/Content/Products/MWS/Overview.aspx

114. D. J. Kern, and D. H. Werner, "Magnetic loading of EBG AMC ground planes and ultra-thin absorbers for improved bandwidth performance and reduced size," *Microwave and Optical Technology Letters*, vol. 48, no. 12, pp. 2468-2471, December 2006.

115. H. Mosallaei, and K. Sarabandi, "Magneto-dielectrics in electromagnetics: concept and applications," *IEEE Trans. Antennas and Propag.*, vol. 52, issue 6, pp. 1558-1567, June 2004.

116. K. Buell, H. Mosallaei, and K. Sarabandi, "A substrate for small patch antennas providing tunable miniaturization factors," *IEEE Trans. on Microw. Theory and Tech.*, vol. 54, no. 1, pp. 135-146,

Jan. 2006.

117. H. Mosallaei, and K. Sarabandi, "Design and modeling of patch antenna printed on magneto dielectric embedded-circuit metasubstrate," *IEEE Trans. on Antennas and Propag.*, vol. 55, no. 1, pp. 45-52, Jan. 2007.

118. M. Karkkainen, and P. Ikonen, “Patch antenna with stacked split-ring resonators as an artificial magneto-dielectric substrate,” *Microwave and Optical Technology Letters*, vol. 46, no. 6, pp. 554 556, Sep. 20, 2005.

119. F. Namin, T. G. Spence, D. H. Werner, and E. Semouchkina, "Broadband, miniaturized stacked-patch antennas for L-band operation based on magneto-dielectric substrates," *IEEE Trans. on Antennas and Propag.*, vol. 58, no. 9, pp. 2817-2822, Sep. 2010.

120. E. F. Knott, J. F. Shaeffer, and M. T. Tuley, *Radar Cross Section*, 2nd Ed., Raleigh, NC, SciTech Publishing, Inc., 2004.

121. D. R. Smith, W. J. Padilla, D. C. Vier, S. C. Nemat-Nasser, and S. Schultz, "Composite medium with simultaneously negative permeability and permittivy," *Phys. Rev. Lett.*, vol. 84, no. 18, pp. 4184-4187, May 2000.

122. T. K. Wu, Ed., *Frequency Selective Surface and Grid Array*, New York: Wiley, 1995.

123. S. R. Best, and J. D. Morrow, "On the significance of current vector alignment in establishing the resonant frequency of small space-filling wire antennas," *IEEE Antennas Wireless Propag. Letters*, vol. 2, pp. 201-204, 2003.

124. S. Tse, S. Izquierdo, J. C. Batchelor and R. J. Langley, “Reduced sized cells for electromagnetic band-gap sources”, *Electronics Letters*, vol. 39, no. 24, pp. 1699 – 1701, 27 Nov. 2003.

125. J. McVay, N. Engheta, and A. Hoorfar, "High impedance metamaterial surfaces using hilber-curve inclusions," *IEEE Microw. and Wireless Compon. Lett.*, vol. 14, no. 3, pp. 130-132, Mar. 2004.

126. P. Kovacs, and Z. Raida, "Dispersion analysis of planar metallo-dielectric EBG structures in Ansoft HFSS," *17th Int. Conf. on Microwaves, Radar and Wireless Commun.*, 19-21 May 2008.

127. L. Liang, C. H. Liang, L. Chen, and X. Chen, "A novel broadband EBG using cascade mushroom-like structure," *Microwave and Optical Technology Letters*, vol. 50, no. 8, pp. 2167-2170, Aug. 2008.

128. L.-J. Zhang, C.-H. Liang, L. Liang, and L. Chen, "A novel design approach for dual-band electromagnetic band-gap structure," *Progress in Electromagnetics Research M*, vol. 4, pp. 81-91, 2008.

129. S. Barbagallo, A. Monorchio, and G. Manara, "Small periodicity FSS screens with enhanced bandwidth performance," *Electronics Letters*, vol. 42, no. 7, pp. 382-384, 30 March 2006.

Appendix

A Sample Code for the Implementation of Wind Driven Optimization

```
%--------------------------------------------------------------------------------
% Sample Matlab / Octave Code for the Wind Driven Optimization.
% Optimization of the Sphere Function in the range of [-5, 5].
% by Zikri Bayraktar - zikribayraktar@gmail.com.
% Penn State University - May 2011.
%--------------------------------------------------------------------------------
tic;  clear;  close all;  clc;  format long g;
delete('output.txt');  delete('pressure'); delete('position');
fid=fopen('output.txt','a');  d=date;   fprintf(fid,d);
% WDO parameters:
param.popsize = 20;                 % population size.
param.npar = 5;                     % Dimension of the problem.
param.maxit = 500;                  % Maximum number of iterations.
param.RT = 3;                       % RT coefficient.
param.g = 0.2;                      % gravitational constant.
param.alp = 0.4;                    % constants in the update equation.
param.c = 0.4;                      % coriolis effect.
maxV = 0.3;                         % maximum allowed speed.
dimMin =  -5;                       % Lower dimension boundary.
dimMax= +5;                         % Upper dimension boundary.
%---------------------------------------------------------------------
% Initializing population:  Position and Velocity :
pos = 2*(rand(param.popsize,param.npar)-0.5) ;              % random population in [-1,1]
vel = maxV * 2 * (rand(param.popsize,param.npar)-0.5);      % random velocity
%---------------------------------------------------------------------
% Evaluate initial population: (Sphere Function)
for K=1:param.popsize,
        x = (dimMax - dimMin) * pos(K,:) + dimMin;
        pres(K,:) = sum (x.^2);
end
%---------------------------------------------------------------------
% Finding best air parcel in the initial population :
[globalpres,indx] = min(pres);
globalpos = pos(indx,:);
minpres(1) = min(pres);             % min pressure
%---------------------------------------------------------------------
% Rank the air parcels :
[sorted_pres rank_ind] = sort(pres);
% Sort the air parcels:
pos = pos(rank_ind,:);
keepglob(1) = globalpres;
%---------------------------------------------------------------------
% Start iterations :
iter = 1;                           % counter
for ij = 2:param.maxit,

        % Update the velocity:
        for i=1:param.popsize
        a = randperm(param.npar);               % choose random dimensions.
```

```
velot(i,:) = vel(i,a);              % choose velocity based on random dimens.
            vel(i,:)      =      (1-param.alp)*vel(i,:)      -      (param.g*pos(i,:))          ...
            +  abs(1-1/i)*((globalpos-pos(i,:)).*param.RT) + (param.c*velot(i,:)/i);
end

% Check velocity:
overlimitV=vel<=(1*maxV);
underlimitV=vel>=(-1*maxV);
vel=vel.*overlimitV + (1*maxV)*not(overlimitV);
vel=vel.*underlimitV + (-1*maxV)*not(underlimitV);

% Update air parcel positions :
pos = pos + vel;
overlimitPos=pos<=(1);
underlimitPos=pos>=(-1);
pos=pos.*overlimitPos + (1)*not(overlimitPos);
pos=pos.*underlimitPos + (-1)*not(underlimitPos);

% Evaluate population: (Pressure)
for K=1:param.popsize,
            x = (dimMax - dimMin) * pos(K,:) + dimMin;
            pres(K,:) = sum (x.^2);
end

%-----------------------------------------------------
% Finding best particle in population
[minpres,indx] = min(pres);
minpos = pos(indx,:);                    % min location for this iteration
%-----------------------------------------------------
% Rank the air parcels:
[sorted_pres rank_ind] = sort(pres);
% Sort the air parcels position, velocity and pressure:
pos = pos(rank_ind,:);
vel = vel(rank_ind,:);
pres = sorted_pres;

% Updating the global best:
better = minpres < globalpres;
if better
            globalpres = minpres           % initialize global minimum
            globalpos = minpos;
 end

% Keep a record of the progress:
keepglob(ij) = globalpres;
save position pos -ascii -tabs;

end
%Save values to the final file.
pressureFile = transpose(keepglob);
save pressure pressureFile -ascii -tabs;
%END
```

VITA

Zikri Bayraktar

EDUCATION :

The Pennsylvania State University, University Park, PA, 16802

- Doctor of Philosophy in Electrical Engineering — May 2011
- Doctor of Philosophy Minor in Computational Science — May 2011
- Master of Science in Electrical Engineering — December 2006
- Bachelor of Science in Electrical Engineering — December 2004

AWARDS :

2010 Leopold B. Felsen Award for *Excellence in Electromagnetics* by the Dogus University.

2010 Anthony J. Ferraro *Outstanding Graduate Research Award in Electromagnetics* in the Penn State University Electrical Engineering Department.

2010 Melvin P. Bloom Memorial *Outstanding Doctoral Research Award* in the Penn State University, Electrical Engineering Department.

2009 Central Pennsylvania IEEE Chapter Student Paper Competition.

2008 IEEE Antennas and Propagation Society *Ph. D. Research Award*.

Dean's List (7 / 7 semesters) – Graduated with Honors and Distinction from B. Sc. E.E.

2004 Arthur Glenn *Undergraduate Summer Research Award*, Schreyer Honors College.

Awarded full scholarship to study abroad at Penn State, 2001-2004.

Ranked **3rd** among *1.4 million* students in the year 2000 National University Entrance Exam in Turkey.